Acoustic Charge Transport in Organic Semiconductors using Surface Acoustic Wave Devices

A thesis submitted
for the award of the degree of

Doctor of Philosophy

by

Himakshi Mishra
Roll No.-166102010

Department of Electronics and Electrical Engineering
Indian Institute of Technology Guwahati
Assam-781039, India
March 2023

TH-3353_166102010

TH-3353_166102010

This thesis is dedicated to my

Nephew Dishu

&

Late aunt, Loni mahi.

TH-3353_166102010

TH-3353_166102010

भारतीय प्रौद्योगिकी संस्थान गुवाहाटी
INDIAN INSTITUTE OF TECHNOLOGY GUWAHATI
Guwahati-781039, Assam, India

Declaration

This is to declare that the thesis entitled "**Acoustic Charge Transport in Organic Semiconductors using Surface Acoustic Wave Devices**" submitted by me to the Indian Institute of Technology Guwahati for the award of the degree of Doctor of Philosophy is a bonafide record of research work carried out by me under the supervision of Prof. Harshal Bhalchandra Nemade. Hereby, I declare that the contents of this thesis, in full or in parts, have not been submitted to any other University or Institute for the award of any degree or diploma.

Dated:

Place: Guwahati, Assam

Himakshi Mishra
Department of Electronics and Electrical Engineering,
Indian Institute of Technology Guwahati,
Guwahati-781039,
Assam, India

TH-3353_166102010

TH-3353_166102010

भारतीय प्रौद्योगिकी संस्थान गुवाहाटी
INDIAN INSTITUTE OF TECHNOLOGY GUWAHATI
Guwahati-781039, Assam, India

Certificate

This is to certify that the thesis entitled "**Acoustic Charge Transport in Organic Semiconductors using Surface Acoustic Wave Devices**" submitted by Himakshi Mishra (166102010), a research scholar in the Department of Electronics and Electrical Engineering, Indian Institute of Technology Guwahati, for the award of the degree of Doctor of Philosophy, is a record of an original research work carried out by her under my supervision and guidance. The thesis has fulfilled all requirements as per the regulations of the institute and in my opinion has reached the standard needed for submission. The results embodied in this thesis have not been submitted to any other University or Institute for the award of any degree or diploma.

Dated: 2 May 2024

Place: Guwahati, Assam

H Nemade

Supervisor: Prof. Harshal Bhalchandra Nemade
Department of Electronics and Electrical Engineering,
Indian Institute of Technology Guwahati, Assam, India

TH-3353_166102010

TH-3353_166102010

Acknowledgements

I want to thank my thesis supervisor, Professor Harshal B. Nemade, from the bottom of my heart for his wise advice and support during my research. I have been greatly inspired by his generosity, commitment, effort, and attention to detail. I would like to express my gratitude to him for his unending encouragement, priceless counsel, and unwavering patience. I owe a great deal of gratitude to the members of my doctoral committee, Prof. Roy Paily Palathinkal, Dr. Arun Tej Mallajosyula, and Dr. Rishikesh Kulkarni, for their insightful comments and recommendations that significantly enhanced the calibre of my thesis work. I would like to acknowledge Department of Electronics & Electrical Engineering (EEE), Centre for Nanotechnology (CNT), and Central Instruments Facility at Indian Institute of Technology (IIT) Guwahati for permitting use of the laboratories, required equipment and facilities to carry out all my experiments. I convey my special thanks to the staff members of EEE department for their assistance in facilitating the completion of different processes in a timely manner. I extend my sincere appreciation to the CNT staff for their assistance with multiple duties. I'd also want to thank the Ministry of Human Resource and Development (MHRD) for funding my Ph.D. studies with a scholarship.

I consider myself lucky to have met Prof. Aditya Mohite from Rice University, USA while he was visiting IIT Guwahati. The discussions we had were quite insightful and helped me in my work. The conversations with him have driven and inspired me in a variety of ways, and I am incredibly appreciative of the perceptive comments and advice he has given me for a stable career.

I appreciate the assistance and guidance of my seniors, Dr. Namami Goswami and Dr. Ningthoujam Somorojit. I would also like to thank my colleagues Atanu Purkayastha, Himangshu Gogoi, Anwesha Choudhury, Kasturi Gogoi, Abhilasha Bora, Sujit, Jinti Hazarika and Rahul Sharma, for the fruitful conversations, assistance, and support. My co-worker and lab partner Paromita Bhattacharjee deserve special mention for her unfailing support, morale, and ability to make my time in the lab and IIT enjoyable. I want to give special recognition to Manjay *Da*, a staff member from the CNT department for his constant physical assistance with laborious tasks including equipment setup, repair, and transportation. I am thankful to the juniors of the CNT department for their help and support.

When one stays in a hostel at a residential campus like IITG for a prolonged amount of time, including the stressful times of Corona, one may find it tough to maintain composure and

TH-3353_166102010

serenity while dealing with the ups and downs of research life. But I was fortunate enough to be surrounded by great friends who made my life easier and my acknowledgment would be incomplete without mentioning their contributions in my PhD journey. I want to express my gratitude to Manisha, Heera, Paromita, Sunanda, Tina, Tori, and Upasana, with whom I shared wonderful hostel experiences like cooking, dancing, dinner and birthday parties. I'm grateful to Sunanda for being there for me through all of my emotional ups and downs. I am appreciative of Tina for her generous information sharing, sincere concern, and unwavering support. I will cherish the recent fun swimming sessions with Paromita and Anwesha.

I would want to end by expressing my sincere gratitude to my *Ma* and *Deta*, Mrs Kabita Misra and Mr Madan Misra, for their unwavering love, inspiration, and support. I'm grateful to my parents for all the sacrifices they made to provide me a life that is more privileged than theirs, and for instilling in me the value of willpower, perseverance, and hard work. I'd like to express my thanks to my brother, Dhritiman Misra, and sister-in-law, Chandana Devi, for their care and encouragements. I am really grateful to my fiancé, Rahul Talukdar, for his willingness to put up with my whining and endless babbling while still offering me unfailing moral and emotional support throughout my journey. Having such kind and understanding family makes me feel privileged. Their excessive support has given me the motivation I needed to continue working and finish my PhD.

Sincerely

Himakshi Mishra

TH-3353_166102010

Abstract

A surface acoustic wave (SAW) is a periodic deformation of the surface of an elastic material propagating at the surface primarily as a linear wavefront. Despite the fact that their existence had already been established by Lord Rayleigh in 1885, it wasn't until 1965, through the development of the interdigital transducer (IDT), that they were first utilised for various applications. It is now feasible to stimulate and detect SAWs on a piezoelectric surface in an effective manner. It is established that SAW devices have a very broad range of applications in several fields. Professional radar and communications systems extensively use SAW delay lines, band pass filters, resonators, oscillators, and matched filters. SAW can also be employed as a pressure, humidity, and temperature sensor for chemical sensing and analysis purposes. SAW has very low velocity and narrow wavelengths, reducing size and weight and hence, can be mass manufactured. When a semiconductor comes into interaction with SAW, the acoustic deformations induced by SAW have a significant impact on the semiconductor's energy bands and, consequently, its electrical characteristics. SAW-induced band edge modulation leads to the spatial separation of charge carriers of a semiconductor. Furthermore, the energy and momentum carried by SAW are transmitted to charge carriers resulting in a dragging force on them. This phenomenon is known as the acoustoelectric effect, and the transport caused by this effect is termed acoustic charge transport (ACT). The process of ACT has been demonstrated by several researchers in inorganic semiconductors either by injecting carriers through an input bias or optically generating carriers. Organic semiconductors are increasingly being used as the active layer in a wide variety of innovative technologies due to their solution-processability, lightweight, and flexibility. In contrast to inorganic semiconductors, organic materials form a polycrystalline layer, and their charge transport is mostly limited by grain boundaries. Numerous studies have been done, throughout the past few years, to investigate the factors affecting and contributing to the charge transport of organic semiconductors. However, the interaction of an acoustic wave with these materials has not been reported yet. The primary objective of the thesis is to observe the charge transport of ambipolar electrons and holes in organic semiconductor films by means of acoustic waves and to investigate potential acousto-optic applications that may result from this interaction.

The introduction of this thesis covers the fundamentals of SAW devices, an extensive literature survey on the ACT with different device configurations and measurement techniques, along with a discussion of the problem definition and scope of the thesis.

TH-3353_166102010

The first major contribution of this thesis is the demonstration of an ACT of optically induced excitons in organic semiconductor films up to a distance of 3 mm. The demonstration was done using a novel device structure consisting of a SAW resonator transmitting SAW through a polymer layer and a polymer diode at the end to collect the charges. The theoretical analysis of the ACT is explained, followed by the experimental results. The results validated the SAW-assisted charge transport where excitons are separated, trapped and moved as spatially separated charge carriers along the SAW path and then collected at the collector (polymer) diode. The acousto-optic characteristics, such as the maximum charge capacity and transfer efficiency of the device, were defined, and the observations opened up the possibility of employing SAW-organic interaction for optoelectronic applications.

The second major contribution of this research work is the interaction of two SAWs and witnessing their control over charge transport in an organic semiconductor. The experimental results reported the influence of high-frequency waves on charge transport by low-frequency waves and vice versa. The idea of using one or more SAWs to achieve acoustic control and manipulation of charge carriers was introduced as a result of the mathematical analysis of the acoustic drag forces exerted on the charge carriers by orthogonally interacting SAW beams of various frequencies.

The third major contribution of this thesis is the attainment of long-range chain alignment of a polymer film using a DC electric field (EF) during film formation by a deposition process. The polarised Raman spectroscopy and electrical conductivity results verified that the polymer chains are aligned in the direction of the applied EF. Improved charge transport in the film was observed as a consequence of the long-range alignment of the polymer chains, which tends to disappear the grain-boundaries in the film.

The fourth major contribution of this thesis is developing and demonstrating novel SAW-assisted charge transfer devices with aligned polymer chains. The intrachain and interchain transport of optically excited charge carriers in an organic semiconductor with SAW serving as the control parameter, was demonstrated and analysed. In addition, the charge crossover of the charge transfer devices with aligned chains is calculated and found to be high efficiency compared to random chain orientation.

The conclusion of this thesis provides a vision of the possible future potential of the research work.

TH-3353_166102010

Contents

TH-3353_166102010

TH-3353_166102010

TH-3353_166102010

List of Figures

TH-3353_166102010

TH-3353_166102010

TH-3353_166102010

TH-3353_166102010

List of Tables

TH-3353_166102010

Chapter 1

Introduction & Literature Survey

1.1 Introduction to surface acoustic waves

A surface acoustic waves (SAW) is an electromechanical wave that travels along the surface of an elastic material and has an amplitude that is limited to one wavelength deep from the surface. Lord Rayleigh [1] was the first to discover the SAWs in semi-infinite isotropic solid bodies in 1885. In the 1960s, SAWs were considered valuable since this type of wave motion could be guided along the surface of a solid material. The invention of interdigital transducers (IDTs) by White and Volmert [2] made it feasible to effectively stimulate and detect SAWs on the surface of a piezoelectric material, thus, introducing the possibility of obtaining the wave within its path of propagation and immensely increasing the prospective potential of the devices. A voltage excitation to the IDTs, on a piezoelectric substrate can lead to mechanical stress and strain in the substrate, resulting in the generation of a surface wave travelling with the velocity of sound. Depending on the wave and particle propagation direction in the substrate, the acoustic waves can be classified as Rayleigh, Shear horizontal, Love, and Bleustein–Gulyaev-Shimizu (BGS) waves. The primary feature of SAW is their enormously low velocity [3] (10^{-5} times that of electromagnetic waves), comprising extremely small wavelengths, and thus provide dramatic reductions in size and weight. SAW devices may therefore be mass manufactured utilising semiconductor microfabrication processes, making them cost-competitive in mass-volume applications. SAW devices have a wide variety of applications in different areas. They can be used as sensors (pressure, humidity and temperature) for chemical sensing and analysis by producing a change in the characteristics of the path over which the acoustic waves travel [4]. SAW delay lines, resonators, band pass filters, matched filters and oscillators have also found great application in professional radar and communications systems [5]. Furthermore, the integration of SAW devices and semiconductors has been found helpful in establishing some unique acoustoelectronic devices for parametric and imaging device applications [6].

TH-3353_166102010

1.2 Generation of SAW

As mentioned in the previous section, a SAW is conventionally generated on a piezoelectric substrate by applying a sinusoidal voltage signal to the comb-like metal electrodes, IDTs, formed in the piezoelectric substrate. Due to the piezoelectric effect, strains are produced in the material. In the presence of strains, as particles try to return to their equilibrium condition or unstrained state, internal forces are formed in the material, leading to stresses [7]. This development of stress and strain results in the propagation of acoustic waves in the material. SAW devices are mostly fabricated on anisotropic materials like lithium niobate, lithium tantalate, quartz etc. The material properties, along with the IDT dimension, have a keen impact on the resonance frequency and velocity of the SAW [8]. Figure 1.1 shows the top view of the IDT structure. The IDTs basically consist of metal fingers of width *a*, pitch *p*, and aperture width *W*. The metallization ratio, which is given by the ratio of *a/p,* is usually kept at 0.5. A voltage application with a frequency matched to the IDTs' resonance causes the emission of SAW on both sides of the finger. The waves add constructively and reach maximum only if the adjacent fingers are spaced at a half wavelength of the SAW [9].

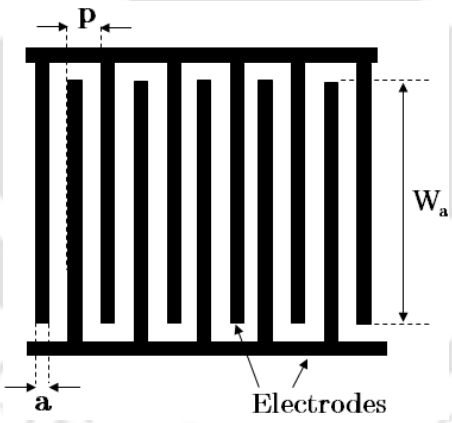

Figure 1.1: IDT structure with finger width *a*, pitch *p*, and aperture width *W*.

The resonance frequency (*f*) of SAW is given by

$$f = \frac{v}{\lambda} \tag{1. 1}$$

$$\lambda = 2p \tag{1. 2}$$

where v is the phase velocity of the SAW, which is constant for a material of specific orientation, and λ is the acoustic wavelength.

TH-3353_166102010

1.2.1 Types of waves

Depending on where the energy is concentrated in the medium space, acoustic waves can either be generated as bulk or surface waves [9]. In a homogeneous, isotropic, limitless material, there are primarily two types of bulk acoustic waves (BAW): longitudinal and transverse (or shear) waves. Longitudinal waves instigate the medium's particles to deviate from their initial positions and move in the wave's direction, as shown in Figure 1.2 (a). Transverse or shear waves, on the other hand, cause the medium's particles to move perpendicular to the direction of the wave, as shown in Figure 1.2 (b). The complete motion of the medium can be horizontal or vertical [10].

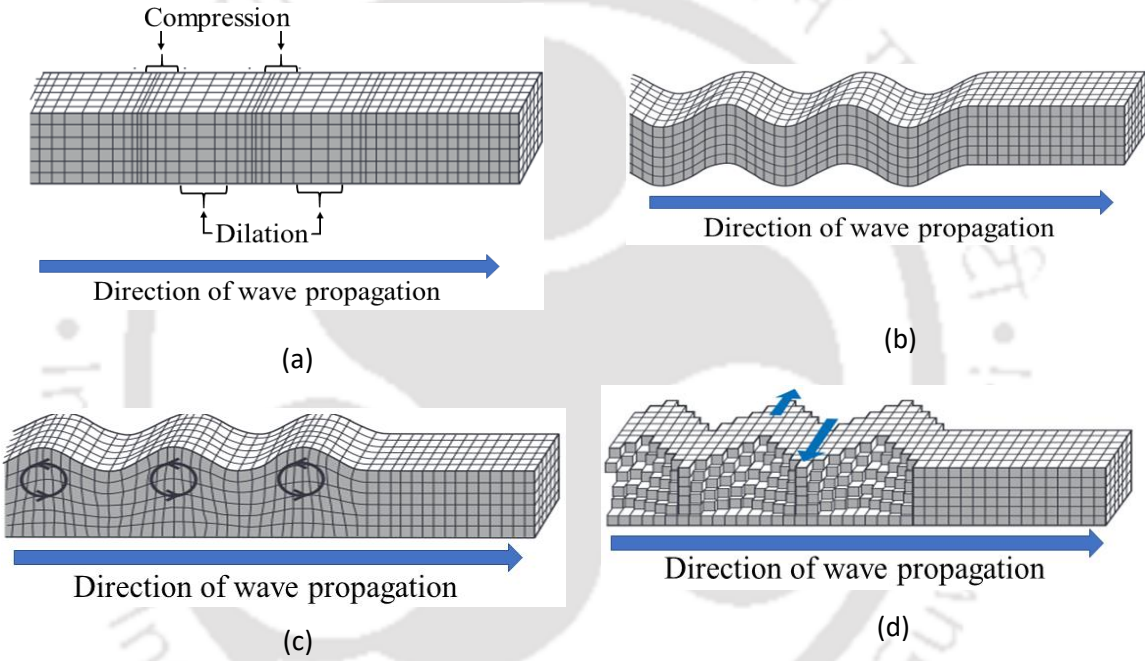

Figure 1.2 (a) Longitudinal wave, (b) Shear horizontal wave, (c) Rayleigh wave, and (d) Love wave. (adapted from [11])

Surface waves are generated along the top surface of a bounded medium. Rayleigh, Sezawa and Love waves are categorized as surface waves. The Rayleigh wave penetrates a material to a depth of one wavelength, with its amplitude decreasing exponentially farther from the surface, as shown in Figure 1.2 (c). The wave movement is in the sagittal plane, which is the plane that contains both the propagation direction and the surface normal; besides, the motion of individual particles is also elliptical [7]. Compared to bulk shear waves, the Rayleigh wave is nondispersive and propagates at a slower velocity [7]. With displacements in the sagittal plane, a second fundamental frequency mode exists called as Sezawa wave. Love waves may be thought of as a modified form of the shear-horizontal plane wave, where the

TH-3353_166102010

presence of a layer with low acoustic velocity transforms the plane wave into a surface wave and produces dispersion [12], as shown in Figure 1.2 (d). Unlike the Rayleigh wave, Sezawa and Love waves are dispersive, and also, the Love wave propagates at a velocity faster than the Rayleigh wave [7].

1.2.2 SAW device configurations

SAW devices are categorised into SAW resonators and SAW delay lines depending on the placement and number of IDTs. In a SAW resonator, the wave travels through a resonant cavity in such a way that the reflector gratings reflect the wave back to the generating IDT. There are two primary types of resonator devices: one port resonator and two port resonators. IDT fingers without reflectors can be used in vast numbers to create a one-port SAW resonator, as shown in Figure 1.3 (a). In this device, multiple reflections between the fingers of the long IDT result in the formation of standing waves and the device resonates at a particular frequency.

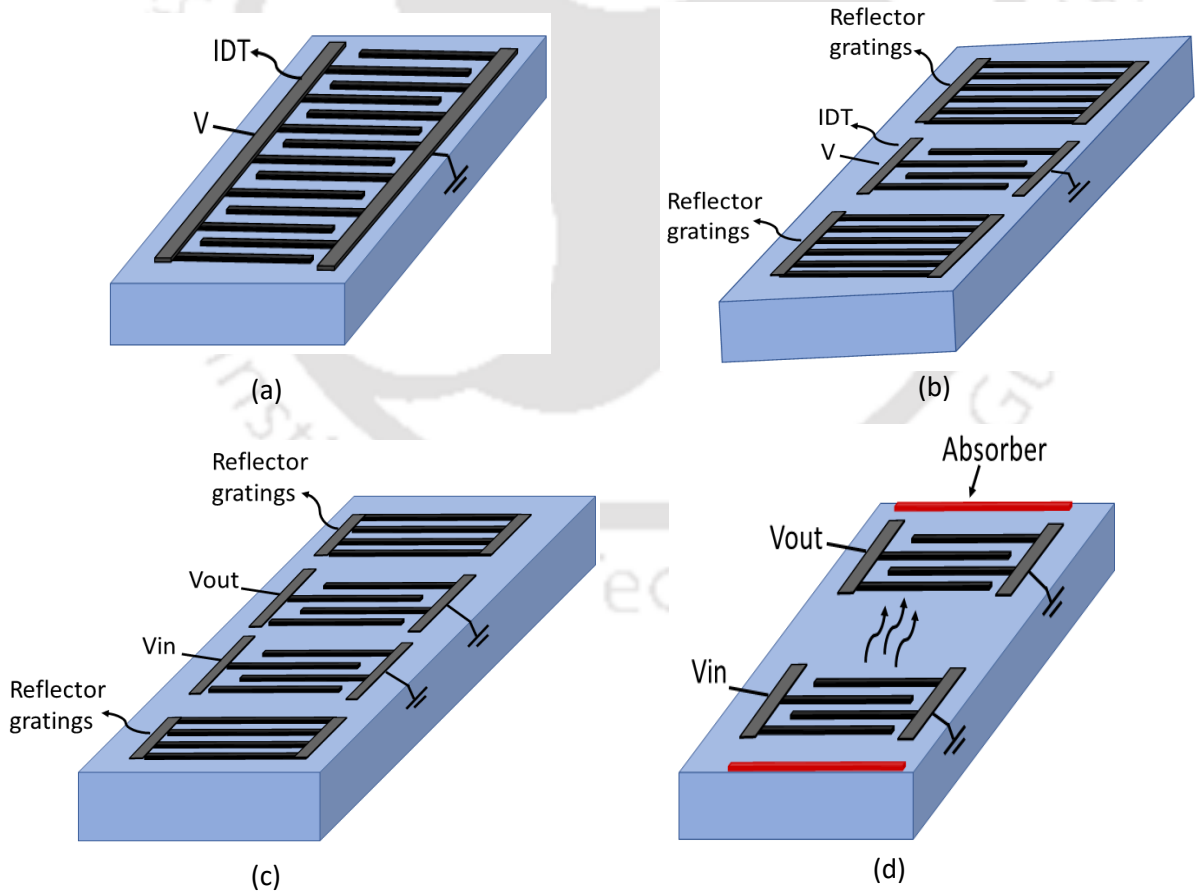

Figure 1.3: SAW device configurations: (a) one-port SAW resonator with large number of IDT fingers, (b) one-port resonator with reflector gratings, (c) two-port SAW resonator, and (d) SAW delay line device with absorbers.

TH-3353_166102010

One port resonator can also be fabricated with a pair of reflector gratings formed on either side of the bi-directional IDT, as illustrated in Figure 1.3(b). The reflector gratings function as mirrors in order to constrain the surface wave that is formed between them and create a standing wave pattern. A shift in the SAW resonator's resonance frequency caused by variations in the mass loading, conductivity, permittivity, and viscosity along the SAW path can be used for sensing applications. A two-port resonator consists of a set of comb electrodes placed between two reflector gratings, as shown in Figure 1.3 (c). The two-port resonator uses a high quality factor, *Q*, and is typically used for oscillators and narrowband filters with a broader frequency range than one-port resonators, despite the fact that it is a narrowband filter due to the construction of the device [13]. SAW delay line consists of an input and output IDT placed at a distance apart from each other, as shown in Figure 1.3(d). An absorber material is placed at the ends of the device so that there are no reflections from the edges as the bi-directional IDT generates surface waves on each side. Considering that the waves are generated on either side of the IDT, only half of the power reaches the output IDT. Due to the piezoelectric effect, only half of the incoming power is transformed into electrical energy at the output IDT. The other half is used up again during SAW formation, which is delivered back in the opposite direction to the input IDT. It results in a 6 dB loss, and when combined with additional second-order effects such as load mismatch and triple transit interference (TTI), which is a loss brought on by repeated SAW reflections between bidirectional input and output IDTs, the losses generally reach 15-20 dB [8]. The delay line is mainly utilised for creating oscillators, sensors, and bandpass filters [7].

1.2.3 SAW device parameters

As mentioned earlier, SAW devices can be employed for applications ranging from sensors to oscillators. The parameters used for the characterization of SAW devices are discussed in the following:

- **SAW frequency** (*f*): The design of the IDT structure and the type of the piezoelectric material employed as a substrate both decide the frequency of the generated SAW.
- **Electromechanical coupling coefficient** (K^2): It is a measurement of how well a particular piezoelectric material transforms an applied electrical signal into mechanical energy linked to a SAW. The substrates with high K^2 value results in attaining low insertion loss (*IL*) devices. Consider the wave velocities of a free unconstrained surface and a metallized surface as v_f and v_m, respectively. The perfect metal coating on the surface that prevents mechanical stress but shorts the parallel component of the wave's

TH-3353_166102010

electric field produces the metallized surface velocity. The K^2 are generally expressed [7] as the percentage difference between the unconstrained and metallized surface and are denoted as below-

$$K^2 = 2\left(\frac{v_f - v_m}{v_f}\right) \times 100 \quad (1.3)$$

- **Insertion loss** (*IL*): When a source voltage V_{in} is applied to a two-port SAW device, SAW is generated. This SAW travels a certain distance and experiences propagation loss before being detected as a signal Vout at the output port. This loss, referred to as the insertion loss (IL), is often measured with the help of a network analyzer as a scattering parameter or transmission coefficient S_{21}. The insertion loss is expressed in dB as [8]

$$IL(dB) = 20\ log\left|\frac{V_{out}}{V_{in}}\right| \quad (1.4)$$

- **Reflection coefficient,** S_{11}: S_{11} measures the amount of power reflected from the input port after connecting the signal source and terminating the output port with a matched load, i.e., when the load impedance Z_L matches the characteristic impedance Z_0. The total reflection coefficient, Γ is measured as

$$\Gamma = \frac{Z_L - Z_0}{Z_L + Z_0} \quad (1.5)$$

$$S_{11} = 20\ log|\Gamma| \quad (1.6)$$

- **Temperature coefficient of delay, TCD**: SAW devices are employed as filters and sensors that must function within a narrow temperature range. As a result, thermal stability is another critical characteristic in the design of many SAW devices. The distance, *l*, between the source and receiver IDT fluctuates with temperature due to the thermal expansion of the materials. Thus, TCD is specified as [7]

$$\alpha_T = \frac{1}{T}\frac{dT}{dTemp} = \frac{1}{l}\frac{dl}{dTemp} - \frac{1}{v_f}\frac{dv_f}{dTemp} \quad (1.7)$$

TH-3353_166102010

where *Temp* is the temperature, and $T = l/v_f$ is the delay. In general, piezoelectric materials with high K^2 have low TCD because high K^2 imply great susceptibility to disturbances.

- **Mass sensitivity (S_f)**: The mass sensitivity (S_f) of a SAW device is defined as the relative change in frequency or phase caused by applying incremental surface mass density (Δm) to the active region of the sensor, A. It is expressed [14] as

$$S_f = \frac{C f^2 \Delta m}{A} \qquad (1.8)$$

where C represents a constant.

- **Crystal orientation**: The capability of a material to possess piezoelectricity is the primary emphasis for SAW propagation in a material, and such materials are anisotropic, with material characteristics that are reliant on material orientation, such as wave velocity and hence resonance frequency. As a result, material orientation is critical and must be stated correctly.

Material	**v_0 m/s**	**K^2**	**TCD ppm/°C**
Lithium niobate, $LiNbO_3$			
Y-Z	3488	2.4%	94
128Y-X	3992	2.7%	75
Quartz SiO_2, ST cut 47.5°Y-X	3159	0.06%	0
Lithium tantalate, $LiTaO_3$			
X-112°Y	3300	0.35%	18
ZnO/glass	2576	0.7%	11
$LiNbO_3$, 64°Y-X, LSAW	4742	5.5%	80
41 °Y-X LSAW	4792	8.5%	80
$LiTaO_3$, 36°Y-X LSAW	4212	2.4%	32
Quartz, 36°Y-X+90°	5100	n/a	0

Table 1.1: Material properties of different substrates [15], [16]

TH-3353_166102010

For example, the notation in

1. YZ lithium niobate ($LiNbO_3$), the surface is perpendicular to the Y axis, whereas SAW travels in the direction of the Z axis.
2. 128° YX $LiNbO_3$ denotes that it is rotated with regard to the Y axis. The surface perpendicular makes an angle of 128° with the Y axis, and the SAW travels in the direction of the X axis.
3. ST, X quartz forms a 42.7° angle with the Y axis, and SAW travels in the direction of the X axis.

Table 1.1 shows the material properties of different film substrates. Parameters like crystal orientation, SAW velocity (v_0), coupling coefficient K^2, and temperature coefficient of delay (TCD) have also been mentioned in the table.

1.2.4 Effect of SAW on semiconductors

SAW generated on a piezoelectric substrate is generally a mechanical wave (strain field) accompanied by a piezoelectric field due to the piezoelectric nature of the substrates. The acoustic deformations via the mechanical wave significantly impact the semiconductors when interacting with SAW. As the atoms in the piezoelectric substrate follow the wave's elliptic movement, their lattice constant changes, creating stress and strain. The mechanical amplitude and potential of the SAW are directly proportional to this pressure. In theory, this could also be used to calculate the acoustic power by measuring the energy shift caused by the deformation potential. The sinusoidal deformation would also affect the energy bands of the semiconductor. It would result in the spatial dependence of the bandgap on the mechanical deformational energy transferred to the semiconductor. The piezoelectric field associated with acoustic deformation, however, has a significant influence on the free carriers as well as on the excitons produced in the semiconductor. The piezoelectric field can cause the ionization of excitons and separate them into free carriers preventing their recombination.

Furthermore, the piezoelectric field also causes modulation of the energy bands of the semiconductor with the sinusoidal electric field, causing a spatial, sinusoidal shift of both bands in parallel. The mechanical and electrical field components of SAW, thus, can result in two types of band edge modulation in semiconductors: type I and type II band edge modulation. The interaction of SAW with the energy bands and hence the carriers in the semiconductor causes changes in the semiconductor's electric characteristics. The effect of acoustic waves on the semiconductor characteristics is termed the Acousto-electric effect. The band edge modulation and acoustoelectric effect will be discussed in detail in the next section. The

TH-3353_166102010

propagation of SAW also causes heating on the substrate surface since every mechanical action creates friction, as does the SAW as it travels down the substrate surface. However, the effect of acoustic deformations and electric fields is thought to be far greater than that of SAW heating.

1.3 Literature Survey

1.3.1 Acousto-electric effect

The acousto-electric effect is a concept first predicted by R. H. Parmenter [17] in 1953. Parmenter defined the acoustoelectric effect as the impact of a single moving longitudinal acoustic wave in a crystal on its conduction electrons. The propagation of an acoustic wave through a piezoelectric substrate result in the production of strain fields accompanied by piezoelectric fields. The strain fields generated as a consequence of the uniform dilation and compression of the substrate further induce a deformation in the semiconductor in contact with the substrate. The deformation instigates a shift in the energy bands of the semiconductor, which further leads to the establishment of a deformation potential. This deformation potential is directly proportional to the dilatation of the substrate caused by the acoustic wave propagation [17], [18]. The band modulation caused by the strain-induced field in the semiconductor is considered as Type-I band modulation [19]. Here, the conduction band and valence band are in the same phase. A theoretical and experimental analysis of the acousto-electric effect indicates that the strain-induced field results in the bunching of electrons and holes in the semiconductor [20], [21] and also exerts an average drag force [20] in the direction of wave propagation. In accordance with classical theory, a wave's momentum flux is v^{-1} times greater than its energy flux, and the average energy and momentum transfer rate from the wave establishes as a pull that drags the charges forward [22]. This relation demonstrates that when an acoustic wave propagates, the charges need some time to attain their equilibrium state, lagging behind the wave and being dragged in the direction of the wave propagation [20]. Huston et al. [23] observed a wave amplification in piezoelectric semiconductors instead of wave attenuation when the drift velocity (v_d) of the carriers is greater than the wave velocity (v_s), indicating the momentum, and hence, the energy can also be transferred from the carriers to the wave. Thus, the acoustoelectric effect can also be employed in the idea of acoustic wave amplification [24]–[26]. The acoustoelectric theory has also been used to describe a transient photoconductive modification of acoustoelectric current and flux in GaAs using propagating fields of amplified phonons [27]. The effect of sheer strain has also been observed in a

TH-3353_166102010

semiconductor-insulator-semiconductor structure of GaN-AlN-GaN [28]. The strain produced due to lattice mismatch in the structure generates polarization fields that shift the flat band voltage and thus effect the charge distribution.

The sinusoidal piezoelectric field associated with the strain field also induces a spatial shift of both semiconductor bands. The shift of the bands is in parallel, i.e., the conduction and valence band are out of phase, maintaining a constant band gap, and is termed Type-II modulation [19]. Therefore, both the strain- induced field and piezoelectric fields result in a dynamic bandgap modulation (type-I and type-II), as shown in Figure 1.4, of a semiconductor which also results in the transport of charges in the direction of wave propagation. The charge transport with the assistance of an acoustic wave is termed acoustic charge transport [29] and has been found helpful in many optoelectronic applications.

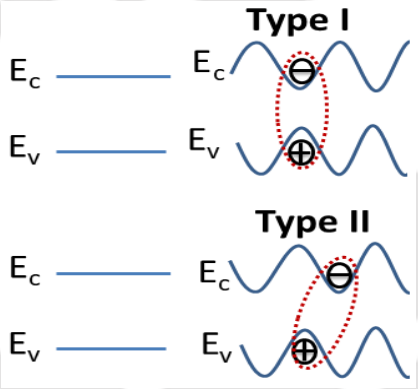

Figure 1.4: Schematic showing the dynamic bandgap modulation: Type-I due to strain-induced fields and Type-II due to piezoelectric fields.

1.3.2 Acoustic charge transport

Acoustic charge transport (ACT) is a fundamental concept of charge carrier transport, predominantly with the assistance of SAW. The process of ACT has been demonstrated by several researchers either by injecting carriers through an input bias or optically generating carriers. The charge carriers are transported unidirectionally along the direction of SAW propagation and are either collected through a collector diode or allowed to recombine, resulting in illuminescence under certain conditions. R. J. Strain [30] was the first to propose an acoustoelectric device in 1972 by realizing a charge-coupled device (CCD) with a sinusoidal travelling wave. He provided a numerical analysis of the CCD travelling wave model by equalizing the CCD operation using a clock cycle with the charge trapped in a traveling potential wave. The charge distribution, potential and power were derived and calculated for the acoustoelectric device. The integration of SAWs with CCDs was then physically realized

TH-3353_166102010

and demonstrated by Gaalema et al. [31] in 1976. They observed that the synchronous drag of minority carriers in the acoustic-optoelectric device by the electric field associated with an acoustic surface wave is possible. A prototype separated media device corresponding to the surface wave interaction CCD (SWICC) has been constructed, as shown in Figure 1.5(a). It was observed that the electric field accompanying the surface wave is creating travelling potential wells along the surface of the adjacent semiconductor which is deep enough to confide the substantial charge and sweep them to a collector diode. Smythe et al. [32] fabricated and tested a fast-in slow-out integrated SAW/CCD buffer memory device in 1978. The device works in a specific "fill and spill" technique, as illustrated in Figure 1.5(b). The device comprises of a CCD shift register with its inputs connected parallel to a set of sampling fingers on silicon (Si) substrate. The Si substrate is pressed against spacer rails on a piezoelectric delay line. A high-speed exchange of charge between the signal well and the storage well is ensured by implanting an n-type ion-implanted buried. The model has been verified for a 100 kHz CCD clock frequency and 80–130 MHz of input signal frequencies, and a dynamic range of 25 dB has been observed. The solid-state device was successful in storing wide-band analog signals and reading them out at a slow data rate. A year later, they demonstrated that the integration of SAW and CCD might result in a range of other signal processing applications as well, such as correlation and matching filter [33].

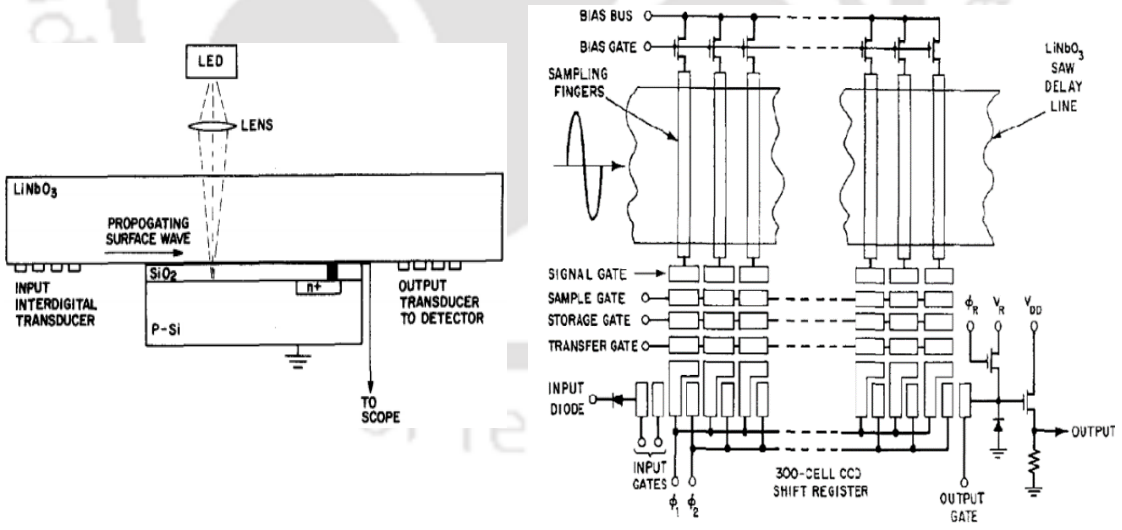

(a) (b)

Figure 1.5 (a) Structure of the SWICC device (Reproduced with permission from [31]. Copyright ©AIP Publishing) (b) Schematic diagram of the SAW/CCD buffer memory. (Reproduced with permission from [32]. Copyright © 1978 IEEE)

TH-3353_166102010

Tsubouchi et al. [34] in 1978 observed the minority charge signal transferred by SAW in a monolithic MIS structure of Al/ZnO/SiO_2/p-Si by developing a configuration of input and output gates and channel-stop bias ring. It was noted that the transit time of the charge packet gives a transfer speed of 2400 m/s, and the group velocity of SAW is 3200 m/s. The difference indicates that the transfer speed is much lower than the group velocity of SAW, and a part of the signal carriers slipped out from the bunching potential of SAW. Papanicolaou et al. [35] proposed that a monolithic ZnO/SiO_2/Si SAW/CCD device can be used in optical applications as solid-state imaging. They defined a parameter, *A*, as the figure of merit. $A = \frac{V_a^2}{2\pi f \mu_s \phi_0} = \frac{V_a/\mu_s}{E_0}$, where μ_s is the surface mobility of the minority carriers in the Si semiconductor and V_a is the surface acoustic wave velocity. If $A > 1$, there is no stable charge in the well. For $A \cong 0$, the charge gets distributed over the entire well, resulting in high charge capacity. While for values of *A* approaching one, only small amount of charge can be gathered by the well and the charge tends to reside in the area of maximum electric field, E_0 . Only the frequency of the travelling potential, *f,* and the surface potential amplitude of the acoustoelectric potential at the Si-SiO_2 interface, ϕ_0, can be used to control the value of *A*. Lastly, they concluded that capturing all charges moving with thermal velocities in either direction of wave propagation is possible. Through device modelling, Augustine et al. [6] in 1981 noted that the Sezawa mode of propagation has a performance advantage over the Rayleigh mode for a monolithic Metal/ZnO/SiO_2/Si (MZOS) device, as shown in Figure 1.6(a) due to better electromechanical coupling of the Sezawa mode. They clarified that the less-than-ideal device performance is owing to a substantial increase in the number of fast surface states after sputtering. The excessive time delay is also a result of the changing trapping by surface states rather than insufficient SAW power. They established that the device performance is constrained by carrier diffusion and the thickness of the SiO_2 layer. They also estimated the charge densities and charge capacity of the SAW in the transport process [36]. Hoskins et al. [37] observed charge transfer in buried channel Schottky np GaAs with an acoustic delay of 0.54 s. They determined that employing SAW as a natural "clock" in a buried channel GaAs structure can create synchronous electron transport at sound velocity, and interfering "clock" signals can be removed via narrowband filtering. After one year, M.J. Hoskins and B.J. Hunsinger [38] explained the fundamental charge transfer characteristics in buried channel structures of GaAs. The charges are transferred by large amplitude SAW creating sinusoidal travelling wave potential wells at adjacent depleted Si surfaces. They observed that in order to enhance the wave's capacity for charge, the active channel layer has to be half an acoustic wavelength or higher. Eventually, they concluded that the performance of the ACT device would not be constrained by the diffusion-induced displacement for wave potentials higher than 1/2 V. The transport efficiency remains unaffected by the electron mobility if the wave's electric field is

TH-3353_166102010

significantly larger than the synchronous field. Furthermore, the transport process is characterised by an increase in its equivalent sheet charge capacity with a rise in the wave frequency [39]. The response of a GaAs ACT device to near-infrared radiation was demonstrated by Beggs et al. [40] and suggests potential applications in systems requiring spatial precision of radiation patterns and optical input signal processing. The research claimed that during the application of light pulses, electrons were separated from holes, picked up by SAW, and collected at the output, yielding an efficiency of 0.09 for the acoustic-opto device [41]. The SAW propagation in the <110> direction on GaAs with an {l00}-cut was used in the non-destructive sensing (NDS) array setup by Hunt et al. [42] in 1990 to transmit charge in discrete packets, as shown in Figure 1.6(b).

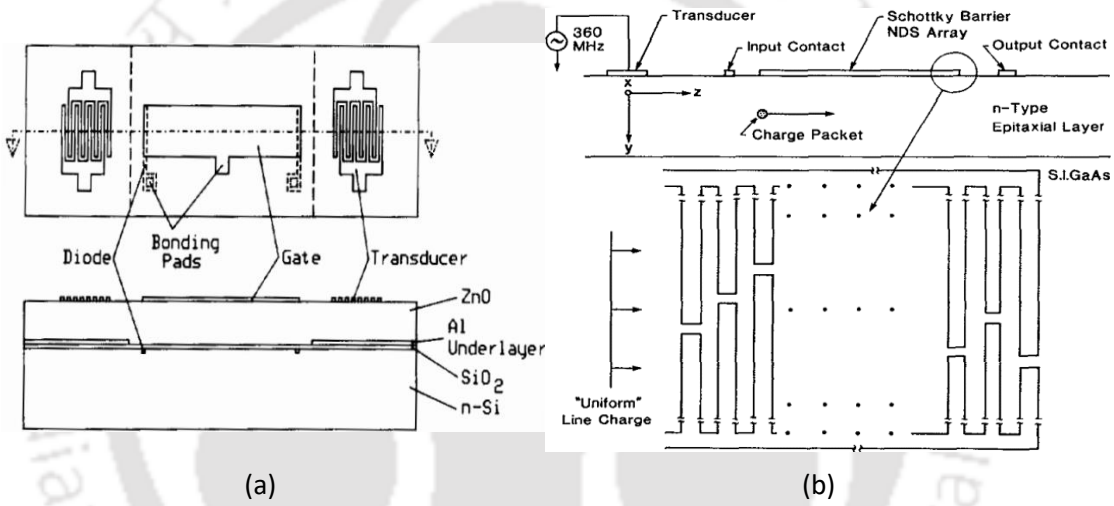

Figure 1.6 (a) Monolithic Metal/ZnO/SiO_2/Si (MZOS) device configuration (Adapted from [6]. Copyright line © 1981 IEEE), (b) Acoustic charge transport device schematic with line charge transport through an NDS array (Reproduced with permission from [42]. Copyright ©AIP Publishing)

These non-destructive arrays are capacitively connected to the charge packets. This setup requires challenging electronic and acoustic design since the NDS array must precisely sense the transferred charge packets while also minimising its impact on the SAW propagation (introduce losses or reflections). The dynamic range for the delay line is determined by the portion of the ACT channel, which is furthest from the SAW transducer. The application of SAW-assisted charge transport in spatial light modulators and optical modulators was established by Jain et al. [43] using a heterostructure ACT device. They achieved the modulation of the transmitted beam by controlling the magnitude of the vertical electric field in the multiple quantum well layers, which in turn, affects the excitonic absorption and degree of modulation. Schmukler [44] investigated a similar form of GaAs ACT devices for single-packet and double-packet charge storage functions. The storage capacity was found to be

TH-3353_166102010

limited by the intercell diffusion, surface extraction, delay line capacity and barrier transition time. This observation provided insight into the dynamics of charge storage in ACT devices. He further tested the charge carrying capacity with different channel gratings size designs and presented an approximate theory to predict the charge capacity losses [45]. Janes et al. [46] associated the charge capacity losses to the various trap distributions in GaAs ACT devices and presented a model of the response characteristics of the trap losses. The charge transfer of a single electron by a high-frequency SAW (2.7 GHz) was attempted by Shilton et al. [47] in a quasi-one-dimensional channel formed in a GaAs-AlGaAs heterostructure. At a SAW wavelength equivalent to the channel length, a current with a magnitude approximately equal to one single electron was observed of high SAW powers. C. Rocke et al. [29], [48] established that the lateral and vertical piezoelectric fields of the acoustic wave ionize the optically generated excitons in a GaAs quantum well and accumulate the resultant electrons and holes in the lateral SAW potential wells spaced apart by a half wavelength. As illustrated in Figure 1.7, SAW propagates along the <110> direction, and the spacing of the IDTs determines an acoustic delay of 1 ms. It was recorded that 30% of the photo-generated and trapped carriers are “lost” along their way. The loss is due to the non-radiative processes along the propagation path, which might be related to the abundance of recombination centres or traps in the quantum well. M. Rotter et al. [49], [50] employed the SAW fields in GaAs-based quantum wells with a high piezoelectric potential amplitude similar to the semiconductor's band gap, which changes the electron system's equilibrium density distribution in a quantum well, splitting it up into spatially isolated charge wires. Decreasing the SAW amplitude expands the observed signal and delays injection and detection. Average electron velocity rises with SAW intensity and saturates at SAW velocity. Strongly nonlinear effects control the acoustoelectric interaction resulting in charging bunching in SAW potential wells. They also observed a carrier phonon drag between weak momentum transfer and an entirely trapped regime [50]. A.O. Govorov et al. [51] demonstrated the quantum theory of the nonlinear interaction between intense SAWs and electrons in a quantum well in moving quantum wires and dots. They revealed that the quantum acoustoelectric interaction results in self-induced transparency for the transmission of SAW. Several researchers used photoluminescence studies to conduct an in-depth investigation of the ACT. Santos et al. [52] performed the micro-photoluminescence (μ-PL) on GaAs at 10 K only to observe a quenching in the photoluminescence (PL) intensity under the influence of SAW, as shown in Figure 1.7(a). The decrease in the μ-PL intensity was related to the ionization of optically induced excitons by the piezoelectric fields associated with SAW. They described a model explaining the effective reduction of the binding energy of the excitons due to the energy gained by the photogenerated carriers in the SAW piezoelectric field. Streibl et al. [53], however, demonstrated the imaging of the ACT at room temperature using two tapered IDTs transmitting SAWs with a bandpass of about 36 MHz and two conventional untapered IDTs,

TH-3353_166102010

as shown in Figure 1.7(b). They also showed the interdependency of the SAW field on the dissociation of photogenerated carriers by varying the intensity of the laser beam. The dynamic screening of the SAW fields prohibits a complete localization of carriers in the potential of the SAW, indicating that the highest transport efficiency is found at lower laser intensities.

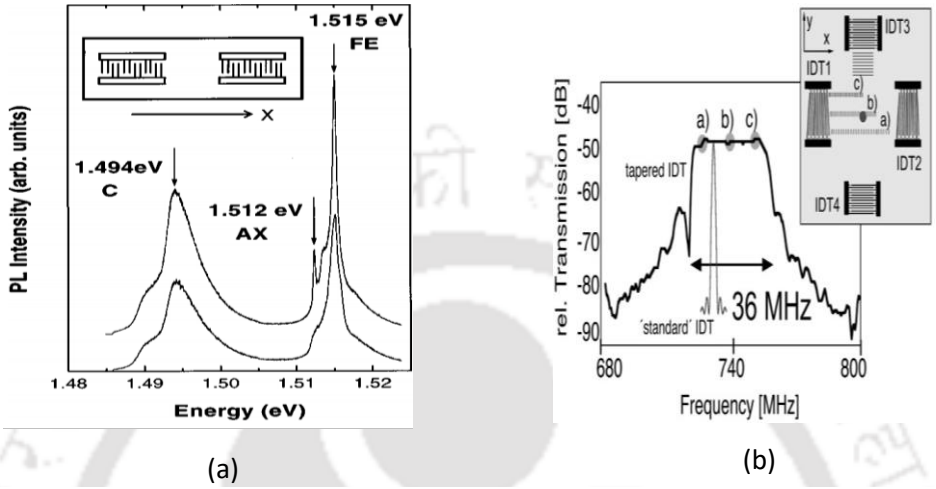

Figure 1.7: (a) GaAs photoluminescence without (upper curve) and under the influence of a SAW (lower curve), (Reproduced with permission from [52]. Copyright ©AIP Publishing). (b) Frequency response of a tapered IDT. The variation of the finger period over the transducer aperture spreads the IDT frequency response to a bandpass of 36 MHz width. (Reproduced with permission from [53]. Copyright ©AIP Publishing).

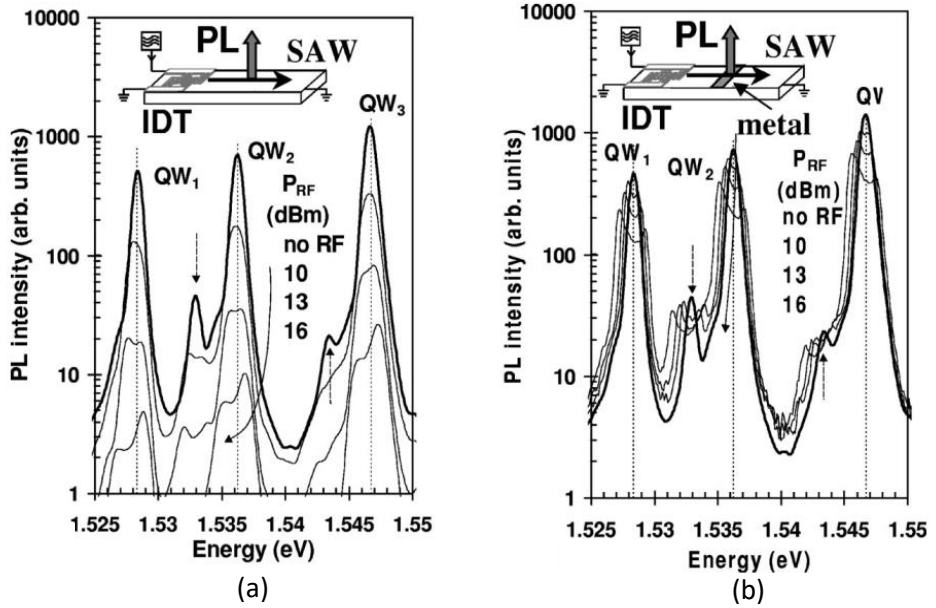

Figure 1.8: Photoluminescence spectra of QW1–QW3 recorded at 16 K (a) on the free sample surface, and (b) over the semi-transparent metal stripe for different RF power levels applied to the SAW transducer (Reprinted with permission from [54]. Copyright ©2001 American Physical Society).

TH-3353_166102010

Sogawa et al. [54] explained the contribution of both the strain field and piezoelectric field of SAW in the dynamic bandgap modulation of the GaAs quantum wells (QWs) with short superlattice barriers by doing PL experiments. At a temperature of 16 K, they noticed that the relative PL intensity was predominately affected by the SAW piezoelectric field. In contrast, the SAW strain field separated from the piezoelectric field by a metal strip induced band splitting in PL spectra, as shown in Figure 1.8(a) and 1.8(b). Santos et al. [55], in their other work, explained the phase relation between the type-I and type-II modulation caused by the strain and piezoelectric fields of SAW in the electronic band structure of GaAs quantum wells, as shown in Figure 1.9(a). The evidence of a reduction in transport efficiency for high SAW fields was deducted from spatially resolved PL measurements of the SAW-induced ambipolar transport of electrons and holes at 15 K. This reduction is thought to be caused by a decrease in hole mobility induced by the VB mixing which increases the transport's sensitivity to potential fluctuations brought on by barrier layer imperfections and interface roughness. Tight binding simulations demonstrating a notable increase in the heavy-hole effective mass under these circumstances lend weight to this view. Rudolph et al. [56] established a long-range transport of excitons with the SAW strain field in (Al, Ga)As double quantum wells at 12 K. The band-gap modulation caused by the SAW strain field captures the long-living indirect excitons in a double quantum well structure inside sub-µm-wide stripes that are parallel to the acoustic wave fronts as demonstrated in Figure 1.9(b). These excitons are then transported over several hundreds of micrometres.

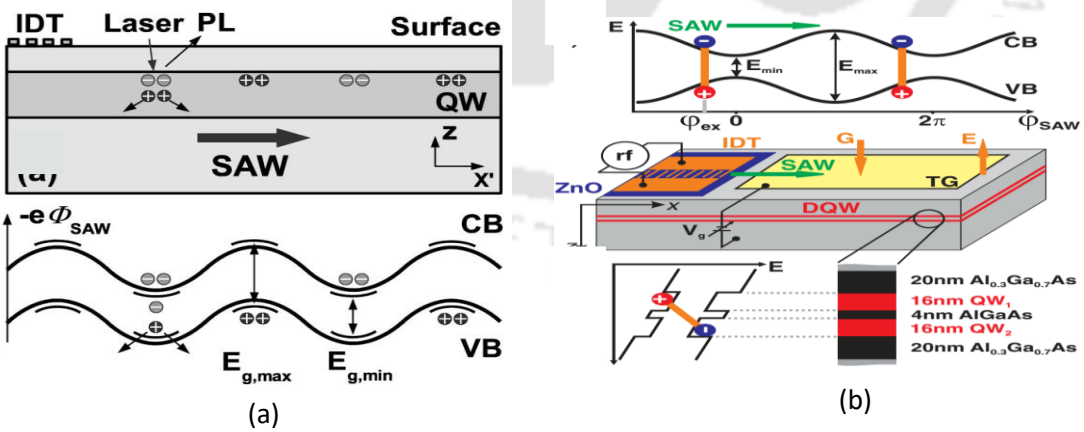

Figure 1.9: (a) Schematic representations of the carrier transport by SAW's and lateral modulation of the band edges by a SAW propagating along the x=[110] direction of the (001) GaAs surface (Reprinted with permission from [55]. Copyright ©2004 American Physical Society). (b) Exciton transport by a surface acoustic wave (SAW): The strain field of a SAW along x=[100] creates a moving lateral type-I modulation of the CB and VB's in a dynamic quantum well (DQW) consisting of QW1 and QW2 which captures and transports long-living indirect excitons (Reprinted with permission from [56]. Copyright ©2007 American Physical Society).

TH-3353_166102010

The strain-induced band modulation decreases, broadens, and splits the PL spectra, demonstrating the onset of long-range acoustic transport. Kataoka et al. [57] investigated the ACT using a two-split gate structure. In a one-dimensional channel, two split gates were connected in series to define the potential for transferring charges carried by SAW. It was discovered that switching the first gate to negative voltages recovers the acoustoelectric current while the second gate is configured to cut off the current, and a set of current-quantization plateaux were detected. The findings showed that the potential gradients control the charge transfer by SAWs in the high transducer-power region. Batista et al. [58] fabricated a photon detector that combines the ambipolar transport of electrons and holes by SAWs with the measurement of electrical charge using a lateral p-i-n junction. This idea allows for the efficient detection of photons without needing additional components. Overall quantum efficiencies of 70% have been reached for ambipolar transport lengths that are more than 100 μm. This efficiency was accomplished by optimising both the photon absorption and the acoustic transport. It is important to note that almost all of these studies with GaAs as substrate were carried out at low temperatures. GaAs have a very low exciton binding energy at room temperature (less than 5 meV) [59] and, as a result, do not completely provide the observation of PL at ambient temperature. Camacho et al. [60] and Palacios et al. [61] both explored the interaction between the photogenerated carriers and SAW in a piezoelectric substrate with a strong coupling coefficient such as GaN. However, PL quenching for the photogenerated e-h pairs in GaN was substantially lower than those observed in GaAs. The low mobility of the carriers inhibiting the spatial segregation of electrons and holes by the SAW field and the high exciton binding energy preventing the ionization of photogenerated e-h pairs were the two processes responsible for the comparatively low quenching effect. Palacios et al. [61] used a metal-semiconductor-metal (MSM) detector to measure the photocurrent that occurred by the collection of carriers swept by the acoustic wave. They have found that the responsivity of the MSM detector varies sub linearly for low RF powers (~ 4 dBm), linearly for RF powers (~7 dBm) and saturates for very high RF powers (greater than 16 dBm). The frequency applied to the SAW transducer, the RF power, and the incident optical power were found to contribute to the responsivity of the MSM detector. Barros et al. [62] investigated the ambipolar transport of electrons and holes using a device structure comprising of a p-i-n junction and a piezoelectric ZnO layer on silicon wafers generating SAWs. The optically generated carriers are subsequently drawn into the shifting SAW piezoelectric field and moved up to a distance of 100 μm toward a lateral p-i-n junction, where they are electrically detected. The characteristics of the lateral p-i-n junction current versus voltage changed due to piezoelectric modulation, and the holes' low mobility constrained the transport efficiency in the medium. These findings pave the way for solar cells and photo-detectors, two types of ambipolar acousto-electric devices made of silicon. Although SAW was proven to carry charge carriers throughout its path

TH-3353_166102010

effectively, these carriers nonetheless suffered losses due to defects and traps present along the propagation path, which affected the transport. Zang et al. [63] reported the radiative recombination of photogenerated electrons and holes at sites located along the SAW propagation path in quantum wells of GaAs. The recombination sites are ascribed to charged defects in or near the quantum well plane that trap the carriers carried by the SAW and cause their recombination. The charged defects produce an electric field causing the transport field acting on the carriers to be smaller than what is required for SAW-induced transport, thus, hindering the transport. Alsina et al. [64] also investigated the dynamics of the radiative trapping centres in the ambipolar transport of electrons and holes induced by SAW. Their work used spatially resolved PL spectroscopy to identify the nature of trapping centres. The primary traps are electron capturing centres for low and moderate acoustic strengths, whereas hole trapping becomes significant for high acoustic power values. The notable characteristic of these trapping centres was the fact that the capture cross sections of the radiative trapping centres depended on acoustic power. Moller et al. [65] justified the PL emission appearing along the transport path of the acoustic waves as a result of the recombination of some carriers at traps such as stacking faults, impurities, or defects. Minguez et al. [66] determined the RF threshold power for the ACT and stated that the fields exceeding the threshold power could even ionize and extract carriers from shallow trapping centres. All the research on SAW-induced charge transport has been done on direct semiconductors like GaAs (a piezoelectric material), and indirect semiconductors like Si deposited on piezoelectric materials. In 2001, Suzuura and Ando [67] provided a study on electron-phonon scattering with effective mass theory in carbon nanotubes. The deformation potential from the change in band structure was deduced from introducing a continuum model for acoustic phonons. This electron-phonon scattering on carbon nanotubes gives an insight to explore the acoustoelectric effect in materials other than Si and GaAs. Ebeckke et al. [68] were first to realize an acoustoelectric current in single wall carbon nanotubes (SWNT) by the use of SAW. The piezoelectric field of the SAW transfers momentum to the electrons in the SWNT, and an acoustoelectric current is observed that oscillates as a function of the applied RF power. This process demonstrates that the potential of the SAW is used to probe the low-dimensional electronic states. During the next couple of years several researchers have investigated the idea of integrating SAW in graphene, a zero-bandgap semiconductor. The electron-phonon interaction in graphene produces a deformation potential [69] which is capable of modifying the graphene band structure. Thalmeier et al. [70] examined the effect of SAW propagation in two-dimensional electron systems of graphene. They performed theoretical analysis correlating the changes in SAW oscillations to the conductivity of graphene and revealed a Dirac to Schrödinger-like crossover, with no attenuation in the Dirac regime. Zhang et al. [71] too proposed a theoretical investigation into the interactions between SAWs and electrons in graphene and discovered that the electronic

TH-3353_166102010

transition associated with the SAW absorption could not be accomplished via inter-band transition channels due to momentum and energy conservation principles. At ambient temperature, substantial SAW absorption by graphene is seen over a broad frequency range up to terahertz, in addition, the intensity of SAW absorption is temperature dependant and can be altered by changing the carrier density. Miseikis et al. [72] demonstrated the directed control of charge carriers using SAWs in graphene grown by chemical vapor deposition on the lithium niobate piezoelectric surface. The transport of p-type charge carriers was discovered to generate a direct current flow when a radio frequency (RF) signal equal to the resonance frequency was supplied to the SAW transducers. The acoustically induced current rises linearly with the applied SAW RF power and can be noticed even in the presence of a bias-generated counter-flow current. Santos et al. [73] investigated their concept of acousto-electric transport in graphene using a Hall bar geometry. The driving mechanism for transport was found to be the drift in a moving piezoelectric field induced by SAW strain field in a semi-insulating SiC substrate. Despite the relatively low piezoelectricity, the SiC piezoelectricity nevertheless serves as the primary driving factor behind ACT. Bandhu et al. [74] demonstrated macroscopic ACT of up to 500 µm in graphene transferred onto lithium niobate piezoelectric substrate. A simple classical relaxation model was used to describe the notion of acousto-electric interaction, and it showed that the acoustoelectric current was proportional to both the strength of the SAW and the attenuation of the wave by the charge transport. Poole et al. [75] studied the acoustoelectric current in graphene as a function of illumination, utilising blue (450 nm) and red (735 nm) light-emitting diodes (LEDs), as well as SAW intensity and frequency. They observed acoustoelectric current increases with illumination more than the measured change in the graphene's conductivity while maintaining a linear relationship with SAW intensity. This observation is consistent with the interaction between the carriers and SAWs represented by the simple classical relaxation model, indicating that the change in the acoustoelectric current is due to the influence of light on the electronic characteristics of graphene. In another work by Poole et al. [76], they examine the acoustoelectric effect in graphene nanorods (GNRs) and show that an acoustoelectric current can be created in GNRs with 200 nm widths at room temperature. As GNR width decreases, acoustoelectric current increases owing to the improved carrier mobility due to increased doping from GNR edge damage-induced doping. Zheng et al. [77] too worked on graphene, manipulated its conductivity by chemical doping and explained the charge transport using a simple classical relaxation model. Doping influences how carriers interact with SAW phonons and make it easier to comprehend the nanoscale acoustoelectric effect. The idea of integrating acoustic waves has been further researched to evaluate its applicability to various materials. Rezk et al. [78] demonstrated that high-frequency sound wave coupling may be used to reversibly tune the PL of single and odd-numbered multi-layered MoS_2. The travelling fields of SAW dissociate the optically induced excitons and trions in MoS_2

TH-3353_166102010

despite possessing a large exciton binding energy of 600 meV. High-frequency acoustic excitation of naturally piezoelectric 2D MoS_2 flakes with an odd number of layers leads to dissociated e-h quasi-particles in the centre regions of the flakes, as shown in Figure 1.10(a). The moving electric field subsequently carried these dissociated quasi-particles to the screening zones towards the flakes' edges, where they recombined radiatively. It is now possible to modify the electronic band structure in odd-numbered layers by incorporating SAW with 2D MoS_2 intrinsic piezoelectric material, creating novel options for optical and electrical applications such as optical delays, beam steering, multiplexing, and demultiplexing. The phenomenon can also be exploited to boost e-h dissociation efficiency in photovoltaic devices. Janker et al. [79] have employed contact-free acoustic-optoelectric spectroscopy to examine the spatiotemporal dynamics of both electrons and holes inside $CsPbI_3$, a halide perovskite, as shown in Figure 1.10(b).

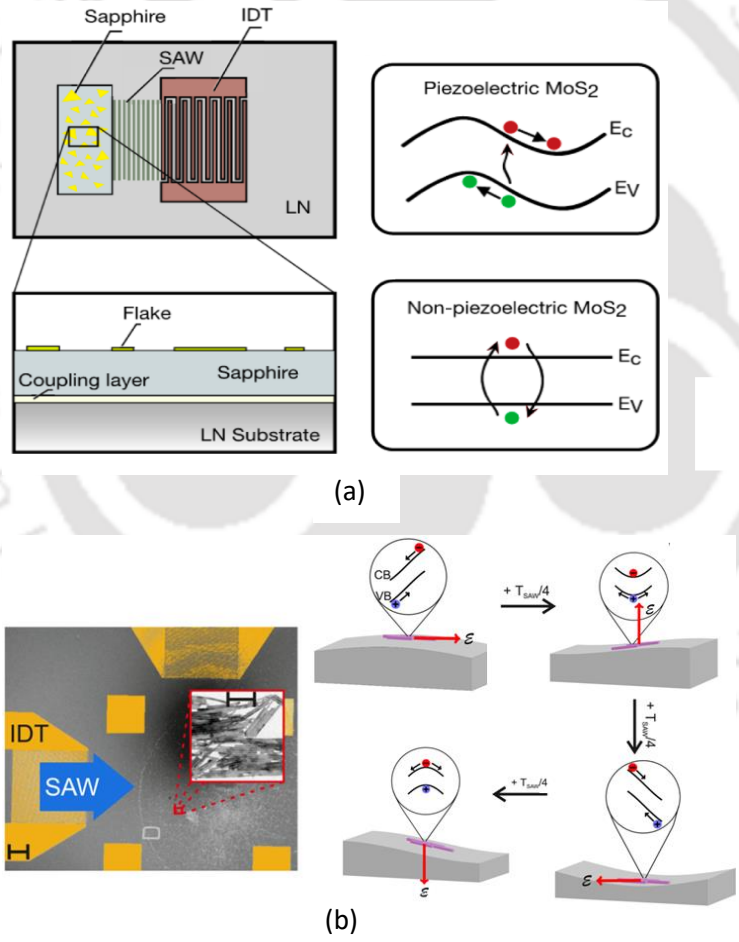

Figure 1.10: (a) Schematic illustration of the experimental setup comprising the SAW device patterned on a lithium niobate substrate with sketches showing the SAW-induced bandgap modulation in 2D MoS_2 with an odd number of layers that is inherently piezoelectric, in contrast to the absence of any modulation of the recombination dynamics in 2D MoS_2 with an even number of layers that is nonpiezoelectric (Adapted with permission from [78]. Copyright © 2016, American Chemical Society). (b) Sample design comprising two IDTs to generate perpendicular SAW beams and individual bundles of aligned $CsPbI_3$ NWs with the illustration of the underlying acoustically driven carrier dynamics. (Adapted from [79]).

TH-3353_166102010

The method distinguishes the quick dynamics of mobile charge carriers from slow ion migration, which stands in contrast to static electrical approaches. The 1D geometry of the $CsPbI_3$ nanowires leads to a significant directionality as there is limited carrier transfer between the nanowires in the loosely arranged bundles. Interparticle hopping can occur in super crystals made from monodisperse nanocrystals, depending on their spacing.Since hopping mobility for both carrier species is critical for nanocrystal- and nanowire-based optoelectronic and photovoltaic systems, the contact-free technique has been found ideal for studying it. In contrast to conventional semiconductors like GaAs, nonradiative surface recombination losses are substantially reduced in these materials. The acoustically induced modulation of the nanowire emission has provided a potential and adaptable path to the high-speed modulation of perovskite light-emitting devices. Halide perovskites are dynamic and starkly different from conventional photoconductive materials. Hence, SAWs can directly examine the photoconductivity of thin films and 2D systems, broadening its scope in sophisticated wirelessly interrogable sensors. Lately, SAWs have been utilised to transport excitons without dissociating them, expanding their usage as an excitonic transistor. Peng et al. [80] in 2022, presented a directional exciton transport in bilayer WSe_2 driven by SAW-induced potential traps at 100 K. The excitonic transport is triggered only by SAWs beyond a threshold acoustic power and reaches 20 µm, ten times the diffusion length of excitons in WSe_2.

In most works, ACT has been illustrated by utilizing a single SAW beam by applying an RF signal to a single IDT constructed on a piezoelectric substrate and the interaction of the SAW beam with charge carriers. On the other hand, a separate charge-regulating behaviour can be achieved by employing two or more SAW beams, as reported by several researchers. The application of ACT into charge carrier manipulation, routing, and directing to their successful extraction or recombination utilising contactless acoustic beams can be regarded as state-of-the-art in solid-state information processing. Lee et al. [81] implemented a logic switch in graphene with two pairs of IDTs to launch SAWs on a $LiNbO_3$ substrate, as shown in Figure 1.11, with the implementation of two IDTs, they alter the propagation direction of acoustoelectric current and purposefully influence the observed current to be positive, negative or even zero by concurrently tuning the input power on the IDTs. By varying the amplitude of the input RF-signal applied to IDTs, they showed that the dynamic switch rate of the acoustoelectric current might be up to 50 kHz. Eventually, they offered a way to transform incoming acoustic waves modulated by digital data sequence onto electric signals with a frequency band suited for digital audio modulation.

TH-3353_166102010

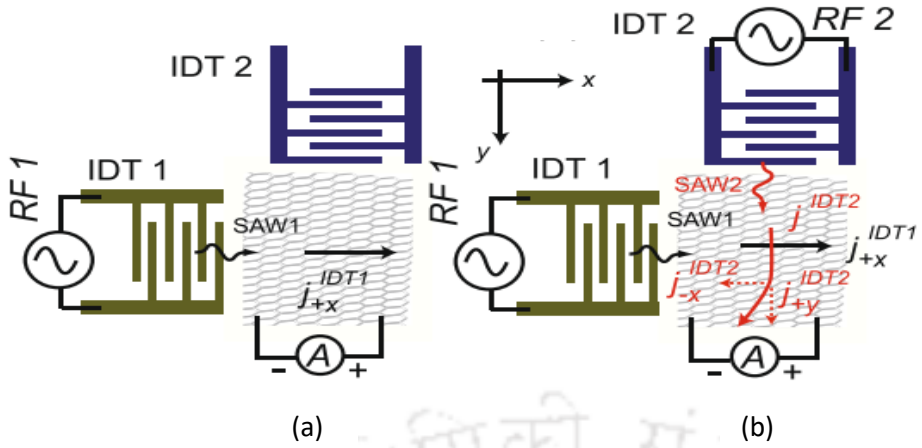

Figure 1.11 Schematics of the design concept for graphene acoustoelectric transducer (a) The acoustoelectric current j_{+x}^{IDT1} in graphene is generated by IDT1 and measured along the positive x-direction. (b) Both IDT1 and IDT2 are activated by two different RF signals. The measured acoustoelectric current is the sum of j_{+x}^{IDT1} and j_{-x}^{IDT2}. (Adapted from [81] Copyright © 2019 Springer Nature).

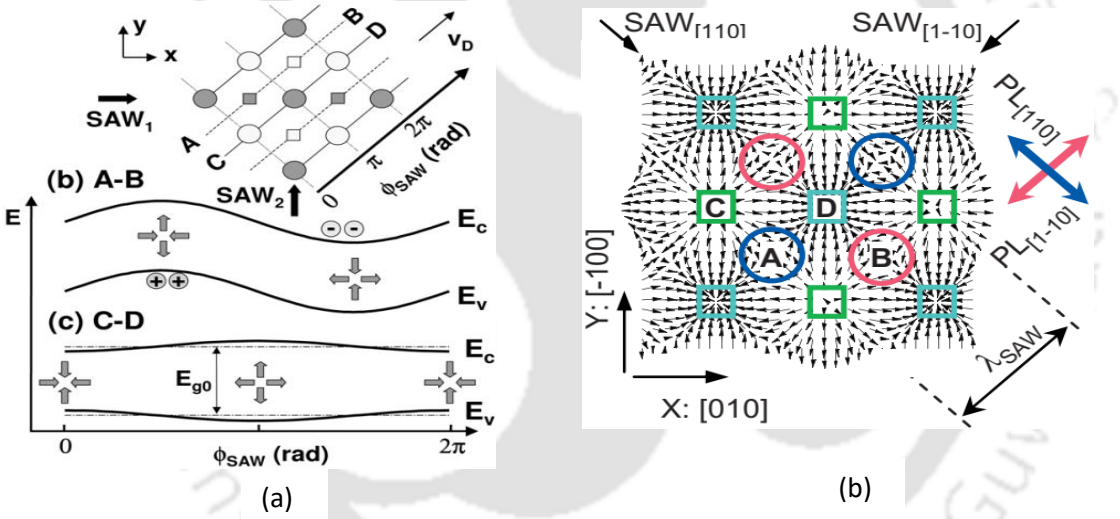

Figure 1.12: (a) Minima and maxima formed by the interference of two SAWs. The conduction (E_c) and valence (E_v) band profiles as a function of the SAW phase f_{SAW} along the lines A–B and C –D, respectively (Reproduced from [82]. Copyright © 2003 Elsevier Ltd.), (b) Schematic illustration of the in-plane components of the particle displacement field with electron-attractive p-DDs denoted by red blue circles, and tensile compressive s-DDs denoted by green light blue squares (Reprinted with permission from [83]. Copyright ©2009 American Physical Society).

Alsina et al. [82] investigated the transport of e-h pairs via type-II dynamic dots formation as well as the dynamic modulation of the band structure by interacting two SAWs. A peculiar distribution, as shown in Figure 1.12(a), of the strain and piezoelectric fields of SAW partially decouples the dynamic dots into channels in the interference zone and determines the internal structure of the dots. The dynamic optical properties of excitons in dynamic quantum dots generated in GaAs/AlAs by the interference of orthogonally propagating SAW beams, as

TH-3353_166102010

shown in Figure 1.12(b), were explored by Sogawa et al. [83]. The formation of two interpenetrating square arrays of dynamic quantum dots, one composed of potential dynamic dots produced by the SAW piezoelectric potential and the other composed of dynamic strain dots produced by the strain-induced band-gap modulation, is shown by spatially and temporally resolved PL measurements using a synchronised excitation method. To comprehend the fundamental concepts behind synchronised excitation PL-mapping spectra, carrier dynamics under SAW fields, which affect exciton diffusion length and PL quenching duration, were used. Lima et al. [84] investigated the viability of employing the interaction of two SAW beams as a means of controlling and modifying the charges that are present in a semiconductor substrate. They showed the variation in charge carriers in a GaAs based quantum well structure by creating a basic control RF switch. The interference of the coherent SAW beams causes the development of a square lattice of dynamic dots with periodicity $\lambda_{SAW}/2$ that move along channels establishing an angle of 45° with the initial beams. By encasing the transported carriers in potential dots or wires positioned in the SAW path, it has been possible to promote the recombination of e-h couples.

1.4 Charge transport in organic semiconductor

Organic semiconductors have significantly changed how current electronic devices are manufactured today due to their inexpensive manufacturing costs, straightforward processing, and large-area fabrication. The investigation of charge transport in organic semiconductors has always been an exciting topic to research. Compared to inorganic crystalline semiconductors, charge transport in organic semiconductors is different. For organic semiconductors, the band gap energy is the energy difference between the lowest unoccupied molecular orbital (LUMO) and the highest occupied molecular orbital (HOMO). These bands are analogues to the valence and conduction bands of the inorganic semiconductors. One advantage of organic semiconductors over their inorganic counterparts is the ability to alter the energy band gap and the position of HOMO and LUMO levels by molecular alignment or by varying the properties of the constituent atoms and functional groups. The hydrocarbons that are π-conjugated give the organic semiconductors their conductivity. Organic semiconductors can be classified as small molecules if the hydrocarbons have a low molecular weight and only a few base molecular units or classified as polymers if the hydrocarbons have a high molecular weight and numerous lengthy repeating monomer units. Polymers possess larger molecular sizes and can be readily dissolved in a variety of solvents, enabling solution processing techniques such as spin coating, dip coating, inkjet printing, and spray coating. These techniques offer advantages

TH-3353_166102010

in terms of scalability and ease of fabrication, allowing for the deposition of polymer thin films over large areas with relatively low cost and complexity. Organic semiconductors have a significant topological disorder, which results in defect levels with a wide energy distribution that extends as band tails into the bandgap. It is widely known that the defect states in thin films control charge transport and impact electrical and optical properties. As per research, it can be said that the charge transport in organic semiconductors is governed by the thin film's crystallinity and charge injection, limited by charge trapping and grain boundary barriers, and altered by applied temperature and field [85], [86]. The transport that enables the charges to move quickly without being trapped is considered efficient [87]. Correspondingly, a vast amount of research has been reported to improve charge transport in organic semiconductor-based devices. These methods have primarily focused on improving surface morphology, carrier injection and conductivity, predominantly by enhancing film formation. The film enhancement approaches involve the introduction of dopant materials [88], the solvent used [89], annealing effects [90], [91] and morphology control [86], choice of the electrode [92]–[95], the inclusion of monolayer [94], [96], and also straining of the thin film [97]. All these methods can be considered an internal process of improving charge transport. Nonetheless, to the best of our knowledge there is no reported analysis for an externally induced charge transport in an organic semiconductor.

1.4.1 Chain alignment and its effect on the charge transport

Numerous studies have demonstrated that the essential building block of all organic electrical and optoelectronic devices, the active organic layer, has considerable effects on the charge transport properties and overall device performance. It has been found that the size, shape, crystallinity, and chain orientation of the conjugated polymers significantly affect the charge-carrier mobility and overall device characteristics [98], [99]. Conjugated polymers still perform significantly worse than their inorganic counterparts in electrical devices. Delocalized electronic states and band structures in inorganic semiconductors lead to long-range crystallinity inside the atomic lattice. The conformation of the polymer backbone, which regulates the capacity of the conjugated electronic states in the frontier molecular orbitals (MOs) to delocalize along the polymer backbone, dramatically influences the charge transport and optoelectronic characteristics of conjugated polymers at the single molecular level. The orientation of the macromolecular chains significantly affects the overall characteristics of the film due to the anisotropy of the polymer chains. Polymer chain alignment has acquired significance in promoting crystallinity in conjugated polymers and overcoming the limits imposed by grain boundaries [100], [101].

TH-3353_166102010

The proper alignment of semiconducting polymer chains is vital to accomplish the required charge transport in organic devices. It has been shown that controlling the chain orientation can raise the charge mobility in organic field effect transistors by an order magnitude [102], improve the conductivity in photovoltaic cells [103], and improve the power conversion efficiency in polymer solar cells [104]. A few techniques, such as spin coating [105], chose of solvent [106], floating film transfer [107], and solvent drying process [108], have been found helpful to some extent in controlling polymer chain orientation and crystallinity, in addition, to other processing methods such as electrospinning [109], nanorubbing [110], and nanoimprint lithography [111]. However, modulating the chain orientation can be done more efficiently and effectively by using external sources, such as the application of magnetic fields [112], shear-flow fields, laser beams [113], and electric fields [109], [114]. Applying an electric field would be considered the easiest way to reverse the chain's orientation out of the available possibilities. In the presence of an electric field, the polarizability of the conductive polymers produces a dipole. An electrostatic charge will be present on the dipole, contributing to electrostatic energy generation. The electric field's existence may impact any particle having electrostatic potential energy [115]. The electrostatic charge of a polymer particle can be changed by an electric field, which will change the direction of the polymer particle relative to the applied electric field. Tassinari [116] et al. examined how a vertical electric field affected the structural characteristics and alignment of thin films made of chiral polybithiophene-based conductive polymers that had protected L-cysteine amino acids functionalized into them. Both drop-casting and spin-coating techniques were used to produce thin films. The electric characteristics, the polarised Raman spectrum, the UV–vis spectrum, and the CD spectra were all measured in relation to the strength of the electric field used to produce the films. Xi [117] et al. investigated the effect of an alternating current (AC) electric field on poly(3-alkylthiophene) (P3AT) polymer and studied the aligned polymer's structural, mechanical and electrical properties. AC electric fields efficiently orient P3AT fibers while undergoing one-dimensional crystallization. Various analytical techniques such as X-ray diffraction (XRD), microscopy, atomic force microscopy (AFM), UV-Vis spectroscopy, rheology, small angle neutron scattering (SANS), and dielectric spectroscopy have been utilized to explore the structural, mechanical, and electrical characteristics. The alignment is confirmed to persist across both micro and nanoscale lengths through optical microscopy, SANS, and XRD. Analysis via small amplitude oscillatory shear rheology reveals that aligned fibers exhibit a insreased shear modulus. Furthermore, enhancements in electrical conductivity, as indicated by dielectric spectroscopy, are associated with the observed structural modifications.

TH-3353_166102010

1.5 Problem statement and scope of the thesis

As it is clear from the literature survey, ACT is a transport process of charge carriers with the help of SAWs in a manner different from usual electric field drift. Here, the carriers are separated and trapped by the SAW-induced fields and transported along with them. The reported work on ACT using SAW mainly operates on inorganic semiconductors such as GaAs, graphene, Si and WSe_2. Organic semiconductors are an intriguing possibility to investigate the integration of acoustic waves and monitor charge transport due to their high exciton binding energy. It is interesting to note that the SAW and charge transport are surface processes in organic semiconductors. The influence of the SAW-induced fields on the separation of charge carriers and transport in organic materials can pave the way for a broad range of applications. It has been assumed that the ACT phenomenon is a less explored area for optoelectronic applications. The acoustic-optoelectric devices present an opportunity to build charge transfer devices for image sensing and other optoelectronic applications.

The main objective of this thesis work is to study and investigate the mechanism of acoustic charge transfer of optically induced charges in organic semiconductor materials, P3HT and MEH-PPV, using a SAW device. The potential integration of SAW with polymeric semiconductors lets one understand how charge transport can be achieved acoustically in organic semiconductors. Consequently, the thesis work analyses and examines the frequency dependence of the acoustic drag force on the charge carriers by orthogonally interacting SAW beams of various frequencies and proposes the notion of employing one or more SAWs to accomplish acoustical control of charge carriers. Further, this thesis presents a method to obtain a semiconducting polymer film with highly aligned chains over a large area by applying a DC electric field during the formation of the polymer film by drop casting. Such an approach is expected to improve crystallinity of organic thin films, overcome limitations of grain boundaries, and is required for fabricating planar ACT devices. In the end, the thesis demonstrates the construction of a SAW-assisted charge transfer device on a perfectly aligned organic thin film which will have a scope in future image sensing and other optoelectronic applications.

Thus, the critical problem statement that has been addressed in the thesis is:

a) Surveying organic materials like conducting polymers that can be used for optoelectronic applications in SAW-assisted acoustic charge transfer devices.
b) Studying and investigating the integration of acoustic waves and organic material and the influence of SAW-induced fields on charge transport.

TH-3353_166102010

c) Designing, fabricating and testing parametric devices based on SAW-organic semiconductor interface for acoustic charge transfer devices.

1.6 Organization of the thesis

The thesis is organized into seven chapters, and its contents are briefly summarised as follows.

Chapter 1 introduces the fundamentals of SAW, the types of SAWs, and basic SAW device configurations and parameters. The fundamental effect of SAW on semiconductors is explained succeeding to a concept of acoustoelectric effect. An extensive literature survey on ACT is presented with different device configurations and measurement techniques. The integration of SAW on the charge transport of organic semiconductors and factors assisting the charge transport is illuminated, along with a discussion of the problem definition and scope of the thesis.

Chapter 2 describes the 3D-Finite element simulation of Rayleigh SAW devices with different IDT dimensions using COMSOL Multiphysics 5.3 and the process for fabrication and characterization of these SAW devices. The resonance frequencies obtained through theoretical analysis, simulation and experimentally fabricated SAW devices are compared.

Chapter 3 demonstrates the ACT of optically induced excitons in organic semiconductor films deposited on $LiNbO_3$ substrates using Rayleigh SAW. The theoretical analysis of the ACT is explained, followed by an acousto-optic and acousto-electric analysis of the fabricated device. Acousto-optic characteristics such as the maximum charge capacity and transfer efficiency of the device have also been defined and calculated.

Chapter 4 implements the directional ACT of optically generated charge carriers in an organic semiconductor experimentally utilizing an easy and straightforward structure of two counter-opposite IDTs. The effect of acoustic drag force on the charge carriers has been studied by interacting two orthogonal SAWs, followed by the analysis of frequency dependence of the drag force. The diagonal propagation of charge carriers through orthogonal SAW beams of the same frequency was also experimentally proven, allowing for the potential of an acoustic charge transfer device that may be used as a fundamental gate for SAW-based information processing.

Chapter 5 presents a technique for long-range chain alignment of a polymer film using a DC electric field (EF) during film formation by a deposition process. The chain alignment is

TH-3353_166102010

verified using the polarized Raman spectra analysis and dichroic ratio (DR) estimation of the Raman peaks in the presence and absence of EF. The conductivity of the film from parallel to perpendicular angles with respect to the direction of EF is calculated and studied to confirm the direction of chain alignment. A simple and easy-to-use electrical setup is proposed and demonstrated for applying EF during polymer deposition.

Chapter 6 demonstrates and analyses the SAW-controlled intrachain and interchain transport of optically excited charge carriers in an organic semiconductor. The operation and performance of the acoustic charge transfer device (CTD) with aligned polymer chains for optoelectronic applications are demonstrated and explained. The charge crossover of the charge transfer devices for aligned and random polymer chain orientations is studied and compared.

Chapter 7 lists the conclusions of the thesis work and recommendations for future work.

TH-3353_166102010

1.7 References

[1] Lord Rayleigh, "On waves propagated along the plane surface of an elastic solid," *Proc. London Math. Soc.*, vol. s1-17, no. 1, pp. 4–11, 1885, doi: 10.1112/plms/s1-17.1.4.

[2] R. M. White and F. W. Voltmer, "Direct piezoelectric coupling to surface elastic waves," *Appl. Phys. Lett.*, vol. 7, no. 12, pp. 314–316, 1965.

[3] D. M. Ştefănescu, "Handbook of force transducers - Principles and components," in *Acoustic Force transducers*, Berlin, Heidelberg: Springer, 2011, pp. 251–274.

[4] D. S. Ballantine, Jr., G. C. Frye, H. Wohltjen, and E. T. Zellers, *Acoustic Wave Sensors: Theory, Design and Physico-Chemical Applications*. 2006.

[5] J. W. Gardener, V. K. Varadan, and O. O. Awadelkarim, *Microsensors MEMS and Smart Devices*. New York, USA, 2001.

[6] F. L. Augustine, R. J. Schwartz, and R. L. Gunshor, "Experimental observation of charge transfer by surface acoustic waves in a monolithic Metal/ZnO/SiO_2/Si (MZOS) device," *Ultrason. Symp.*, pp. 769–773, 1981.

[7] D. Morgan, *Surface Acoustic Wave Filters: With Applications to Electronic Communications and Signal Processing*. Academic Press, 2010.

[8] C. Campbell, *Surface Acoustic Wave Devices and Their Signal Processing Applications*. Academic Press, 1989.

[9] D. Royer and E. Dieulesaint, *Elastic Waves in Solids II: Generation, Acousto-optic Interaction, Applications*. Springer Science & Business Media, 1999.

[10] "Wavesimulations."[Online].Available http://www.nojigon.webs.upv.es/%0Asimulations_waves.php.

[11] J. Santos, A. N. Catapang, and E. D. Reyta, "Understanding the fundamentals of earthquake signal sensing networks," *AnalogDialogue*, 2019. [Online]. Available https://www.analog.com/en/analog-dialogue/articles/understanding-the-fundamentals-of-earthquake-signal-sensing-networks.html#.

[12] G. McHale, M. I. Newton, F. Martin, E. Gizeli, and K. A. Melzak, "Resonant conditions for Love wave guiding layer thickness," *Appl. Phys. Lett.*, vol. 79, no. 21, pp. 3542–3543, 2001, doi: 10.1063/1.1420776.

[13] T. Nomura, A. Saitoh, Y. Horikoshi, and S. Furukawa, "Liquid sensing system based on two port SH-SAW resonator," *Ultrason. Symp. Proceedings, IEEE*, vol. 1, pp. 477–480, Jan. 1999, doi: 10.1109/ULTSYM.1999.849443.

[14] Z. Chen *et al.*, "Ultrahigh-frequency surface acoustic wave sensors with giant mass-loading effects on electrodes," *ACS Sensors*, vol. 5, no. 6, pp. 1657–1664, 2020, doi: 10.1021/acssensors.0c00259.

TH-3353_166102010

[15] A. A. Oliner, *Acoustic Surface Waves*,. *Topics In Applied Physics*: Volume 24. Springer-Verlag, 1978.

[16] G. S. Kino, *Acoustic Waves: Devices, Imaging, and Analog Signal Processing*, vol. 100. Prentice-Hall, Inc., 1987.

[17] R. H. Parmenter, "The Acousto-electric effect," *Phys. Rev.*, vol. 89, no. 5, pp. 990–998, 1953.

[18] G. Weinreich, "Acoustodynamic effects in semiconductors," *Phys. Rev.*, vol. 104, no. 2, pp. 321–324, 1956.

[19] R. Fandan, J. Pedrós, and F. Calle, "Exciton-plasmon coupling in 2d semiconductors accessed by surface acoustic waves," *ACS Photonics*, vol. 8, no. 6, pp. 1698–1704, 2021, doi: 10.1021/acsphotonics.1c00173.

[20] G. Weinreich, T. M. Sanders, Jr., and H. G. White, "Acoustoelectric effect in n-type germanium," *Phys. Rev.*, vol. 114, no. 1, pp. 33–44, 1959.

[21] G. Weinreich and H. G. White, "Observation of the acoustoelectric effect," *Phys. Rev.*, vol. 106, no. 1, pp. 1–3, 1957.

[22] G. Weinreich, "Ultrasonic attenuation by free carriers in germanium," *Phys. Rev.*, vol. 107, pp. 1–2, 1957.

[23] A. R. Hutson, "Acousto-electric explanation of non-ohmic behavior in piezoelectric semiconductors and bismuth," *Phys. Rev. Lett.*, vol. 9, no. 7, pp. 296–298, 1962, doi: 10.1103/PhysRevLett.9.296.

[24] P. K. Tien, "Nonlinear theory of ultrasonic wave amplification and current saturation in piezoelectric semiconductors," *Phys. Rev.*, vol. 171, no. 3, pp. 970–986, 1968.

[25] S. G. Eckstein, "Acoustoelectric effect," *J. Appl. Phys.*, vol. 35, no. 9, pp. 2702–2707, 1964, doi: 10.1063/1.1713826.

[26] J. S. Heyman, "Phase insensitive acoustoelectric transducer," *J. Acoust. Soc. Am.*, vol. 64, no. 1, pp. 243–249, 1978, doi: 10.1121/1.381968.

[27] G. K. Celler and R. Bray, "Modulation of acoustoelectric domains by intense 1.06-μm laser excitation of electrons in GaAs," *Phys. Rev. B*, vol. 13, no. 12, pp. 5397–5409, 1976.

[28] A. Bykhovski, B. Gelmont, and M. Shur, "The influence of the strain-induced electric field on the charge distribution in GaN-AlN-GaN structure," *J. Appl. Phys.*, vol. 74, no. 11, pp. 6734–6739, 1993, doi: 10.1063/1.355070.

[29] C. Rocke, S. Zimmermann, A. Wixforth, and J. P. Kotthaus, "Acoustically driven storage of light in a quantum well," *Phys. Rev Lett.*, pp. 4099–4102, 1997.

[30] R. J. Strain, "Properties of an idealized traveling-wave charge-coupled device," *IEEE*

TH-3353_166102010

Trans. Electron Devices, vol. 19, no. 10, pp. 1119–1130, 1972, doi: 10.1109/T-ED.1972.17559.

[31] S. D. Gaalema, R. J. Schwartz, R. L. Gunshor, S. D. Gaalema, R. J. Schwartz, and R. L. Gunshor, "Acoustic surface wave interaction charge-coupled device," *Appl. Phys. Lett.*, vol. 82, pp. 1–3, 1976.

[32] D. L. Smythe, R. W. Ralston, B. E. Burke, and E. Stern, "An acoustoelectric SAW/CCD device," *1978 Ultrason. Symp. Proceedings, IEEE*, pp. 16–19, 1978.

[33] D. L. Smythe and Ral, "Integrated surface acoustic wave/charge-coupled (SAW/CCD) signal processing devices," *SPIE Opt. Signal Process. C3I*, vol. 209, pp. 152–158, 1979.

[34] K. Tsubouchi, T. Higuchi, M. Nagao, and N. Mikoshiba, "Charge transfer by surface acoustic waves on a monolithic MIS structure," *Appl. Phys. Lett.*, vol. 33, no. 8, pp. 762–765, 1978, doi: 10.1063/1.90496.

[35] N. H. Papanicolauo and H. C. Lin, "A surface acoustic wave (SAW) charge transfer imager," *SPIE Mosaic Focal Pl. Methodol.*, vol. 244, pp. 145–152, 1980.

[36] F. L. Augustine, R. J. Schwartz, and R. L. Gunshor, "Modelling of charge transfer by surface acoustic waves in a monolithic Metal/ZnO/SiO2/Si System," *IEEE Trans. Electron Devices*, vol. 29, no. V, pp. 1876–1883, 1982.

[37] M. J. Hoskins, H. Morkoç, B. J. Hunsinger, M. J. Hoskins, H. Morkoc, and B. J. Hunsinger, "Charge transport by surface acoustic waves in GaAs charge transport by surface acoustic waves in GaAs," *Appl. Phys. Lett.*, vol. 332, no. 1982, 2003, doi: 10.1063/1.93526.

[38] M. J. Hoskins and B. J. Hunsinger, "Simple theory of buried channel acoustic charge transport in GaAs," *J. Appl. Phys.*, vol. 55, no. 2, pp. 413–426, 1984, doi: 10.1063/1.333089.

[39] M. J. Hoskins and B. J. Hunsinger, "Recent developments in acoustic charge transport devices," pp. 439–450, 1986.

[40] B. C. Beggs, L. Young, and R. R. Johnson, "Response of an acoustic charge transport device to near-infrared radiation.," *Int. Electron Devices Meet.*, pp. 294–297, 1987, doi: 10.1109/iedm.1987.191413.

[41] B. C. Beggs, L. Young, and R. R. Johnson, "Optical charge injection into a gallium arsenide acoustic charge transport device," *J. Appl. Phys.*, vol. 63, no. 7, pp. 2425–2430, 1988, doi: 10.1063/1.341037.

[42] W. D. Hunt, Y. Kim, and F. M. Fliegel, "A synopsis of surface acoustic wave propagation on {100}-cut 〈110〉 -propagating gallium arsenide," *J. Appl. Phys.*, vol. 69, no. 4, pp. 1936–1941, 1991, doi: 10.1063/1.348765.

[43] F. C. Jain and K. K. Bhattacharjee, "Two-dimensional spatial light modulators utilizing HACT-controlled quantum confined Stark effect," *Opt. Inf. Process. Syst. Archit. II,*

TH-3353_166102010

vol. 1347, 1990, p. 614, 1990, doi: 10.1117/12.23451.

[44] B. C. Schmukler, “Dynamics of charge storage in acoustic charge transport devices on GaAs,” *J. Appl. Phys.*, vol. 69, no. 5, pp. 3335–3344, 1991, doi: 10.1063/1.348562.

[45] B. C. Schmukler, “The effects of grating size on acoustic charge transport properties on GaAs,” *J. Appl. Phys.*, vol. 71, no. 8, pp. 3853–3858, 1992, doi: 10.1063/1.350875.

[46] D. B. Janes and M. J. Hoskins, “Response characteristics of trapping loss in acoustic charge transport devices,” *IEEE Trans. Electron Devices*, vol. 39, no. 11, pp. 2452–2458, 1992.

[47] J. M. Shilton *et al.*, “High-frequency single-electron transport in a quasi-one-dimensional GaAs channel induced by surface acoustic waves,” *J. Phys. Condens. Matter*, vol. 8, pp. 531–539, 1996.

[48] C. Rocke, A. O. Govorov, and A. Wixforth, “Exciton ionization in a quantum well studied by surface acoustic waves,” *Phys. Rev. B*, vol. 57, no. 12, pp. 6850–6853, 1998.

[49] M. Rotter, A. Wixforth, W. Ruile, D. Bernklau, and H. Riechert, “Giant acoustoelectric effect in GaAs/LiNbO3 hybrids,” *Appl. Phys. Lett.*, vol. 73, no. 15, pp. 2128–2130, 1998, doi: 10.1063/1.122400.

[50] M. Rotter, A. V Kalameitsev, A. O. Govorov, W. Ruile, and A. Wixforth, “Charge conveyance and nonlinear acoustoelectric phenomena for intense surface acoustic waves on a semiconductor quantum well,” *Phys. Rev. Lett.*, vol. 82, pp. 2171–2174, 1999.

[51] A. O. Govorov, A. V. Kalameitsev, V. M. Kovalev, H.-J. Kutschera, and A. Wixforth, “Self-induced acoustic transparency in semiconductor quantum films,” *Phys. Rev. Lett.*, vol. 88, no. 22, p. 226803, 2001, doi: 10.1103/PhysRevLett.87.226803.

[52] P. V. Santos, M. Ramsteiner, and F. Jungnickel, “Spatially resolved photoluminescence in GaAs surface acoustic wave structures,” *Appl. Phys. Lett.*, vol. 72, no. 17, pp. 2099–2101, 1998, doi: 10.1063/1.121288.

[53] M. Streibl, A. Wixforth, J. P. Kotthaus, A. O. Govorov, C. Kadow, and A. C. Gossard, “Imaging of acoustic charge transport in semiconductor heterostructures by surface acoustic waves,” *Appl. Phys. Lett.*, vol. 75, no. 26, pp. 4139–4141, 1999, doi: 10.1063/1.125562.

[54] T. Sogawa, P. V. Santos, S. K. Zhang, S. Eshlaghi, A. D. Wieck, and K. H. Ploog, “Dynamic band-structure modulation of quantum wells by surface acoustic waves,” *Phys. Rev. B - Condens. Matter Mater. Phys.*, vol. 63, no. 12, pp. 3–5, 2001, doi: 10.1103/PhysRevB.63.121307.

[55] P. V. Santos, F. Alsina, J. A. H. Stotz, and R. Hey, “Band mixing and ambipolar transport by surface acoustic waves in GaAs quantum wells,” *Phys. Rev. B*, vol. 69, p. 155318, 2004, doi: 10.1103/PhysRevB.69.155318.

TH-3353_166102010

[56] J. Rudolph, R. Hey, and P. V. Santos, “Long-range exciton transport by dynamic strain fields in a gaas quantum well,” *Phys. Rev. Lett.*, vol. 99, p. 047602, 2007, doi: 10.1103/PhysRevLett.99.047602.

[57] M. Kataoka, C. H. W. Barnes, H. E. Beere, D. A. Ritchie, and M. Pepper, “Experimental investigation of the surface acoustic wave electron capture mechanism,” *Phys. Rev. B - Condens. Matter Mater. Phys.*, vol. 74, no. 8, pp. 2–5, 2006, doi: 10.1103/PhysRevB.74.085302.

[58] P. D. Batista, R. Hey, and P. V. Santos, “Efficient electrical detection of ambipolar acoustic transport in GaAs,” *Appl. Phys. Lett.*, vol. 92, no. 26, pp. 1–4, 2008, doi: 10.1063/1.2955522.

[59] G. Bastard, E. E. Mendez, L. L. Chang, and L. Esaki, “Exciton binding energy in quantum wells,” *Phys. Rev. B*, vol. 26, no. 4, pp. 1974–1979, 1982, doi: 10.1103/PhysRevB.26.1974.

[60] J. Camacho *et al.*, “Modulation of the electronic properties of GaN films by surface acoustic waves,” *J. Appl. Phys.*, vol. 94, no. 3, pp. 1892–1897, 2003, doi: 10.1063/1.1582556.

[61] T. Palacios, F. Calle, and J. Grajal, “Remote collection and measurement of photogenerated carriers swept by surface acoustic waves in GaN,” *Appl. Phys. Lett.*, vol. 84, no. 16, pp. 3166–3168, 2004, doi: 10.1063/1.1711172.

[62] A. D. Barros, P. D. Batista, A. Tahraoui, J. A. Diniz, and P. V Santos, “Ambipolar acoustic transport in silicon,” *J. Appl. Phys.*, vol. 112, no. 1, 2012, doi: 10.1063/1.4733966.

[63] S. K. Zhang, P. V. Santos, and R. Hey, “Radiative recombination during ambipolar carrier transport by surface acoustic waves in GaAs quantum wells,” *Appl. Phys. Lett.*, vol. 80, no. 13, pp. 2320–2322, 2002, doi: 10.1063/1.1463706.

[64] F. Alsina, J. A. H. Stotz, R. Hey, and P. V. Santos, “Radiative recombination during acoustically induced transport in GaAs quantum wells,” *J. Vac. Sci. Technol. B Microelectron. Nanom. Struct.*, vol. 24, no. 4, p. 2029, 2006, doi: 10.1116/1.2214715.

[65] M. Möller *et al.*, “Polarized recombination of acoustically transported carriers in GaAs nanowires,” *Nanoscale Res. Lett.*, vol. 7, pp. 1–7, 2012, doi: 10.1186/1556-276X-7-1.

[66] A. Hernández-Mínguez *et al.*, “Acoustically driven photon antibunching in nanowires,” *Nano Lett.*, vol. 12, no. 1, pp. 252–258, 2012, doi: 10.1021/nl203461m.

[67] H. Suzuura and T. Ando, “Phonons and electron-phonon scattering in carbon nanotubes,” *Phys. Rev. B - Condens. Matter Mater. Phys.*, vol. 65, no. 23, pp. 1–15, 2002, doi: 10.1103/PhysRevB.65.235412.

[68] J. Ebbecke, C. J. Strobl, and A. Wixforth, “Acoustoelectric current transport through single-walled carbon nanotubes,” *Phys. Rev. B - Condens. Matter Mater. Phys.*, vol. 70, no. 23, pp. 1–4, 2004, doi: 10.1103/PhysRevB.70.233401.

TH-3353_166102010

[69] K. Kaasbjerg, K. S. Thygesen, and K. W. Jacobsen, "Unraveling the acoustic electron-phonon interaction in graphene," *Phys. Rev. B - Condens. Matter Mater. Phys.*, vol. 85, no. 16, pp. 7–9, 2012, doi: 10.1103/PhysRevB.85.165440.

[70] P. Thalmeier, B. Dóra, and K. Ziegler, "Surface acoustic wave propagation in graphene," *Phys. Rev. B*, vol. 81, no. 4, p. 041409, 2010, doi: 10.1103/PhysRevB.81.041409.

[71] S. H. Zhang and W. Xu, "Absorption of surface acoustic waves by graphene," *AIP Adv.*, vol. 1, no. 2, p. 022146, 2011, doi: 10.1063/1.3608045.

[72] V. Miseikis, J. E. Cunningham, K. Saeed, R. O'Rorke, and A. G. Davies, "Acoustically induced current flow in graphene," *Appl. Phys. Lett.*, vol. 100, no. 13, p. 133105, 2012, doi: 10.1063/1.3697403.

[73] P. V. Santos, T. Schumann, M. H. Oliveira, J. M. J. Lopes, and H. Riechert, "Acousto-electric transport in epitaxial monolayer graphene on SiC," *Appl. Phys. Lett.*, vol. 102, no. 22, 2013, doi: 10.1063/1.4809726.

[74] L. Bandhu, L. M. Lawton, and G. R. Nash, "Macroscopic acoustoelectric charge transport in graphene," *Appl. Phys. Lett.*, vol. 103, no. 133101, pp. 1–4, 2013, doi: 10.1063/1.4822121.

[75] T. Poole, L. Bandhu, and G. R. Nash, "Acoustoelectric photoresponse in graphene," *Appl. Phys. Lett.*, vol. 106, no. 13, 2015, doi: 10.1063/1.4916940.

[76] T. Poole and G. R. Nash, "Acoustoelectric current in graphene nanoribbons," *Sci. Rep.*, vol. 7, no. 1, pp. 1–9, 2017, doi: 10.1038/s41598-017-01979-8.

[77] S. Zheng *et al.*, "Acoustic charge transport induced by the surface acoustic wave in chemical doped graphene," *Appl. Phys. Lett.*, vol. 109, no. 18, p. 183110, 2016, doi: 10.1063/1.4967192.

[78] A. R. Rezk *et al.*, "Acoustically-driven trion and exciton modulation in piezoelectric two-dimensional MoS_2," *Nano Lett.*, vol. 16, no. 2, pp. 849–855, 2016, doi: 10.1021/acs.nanolett.5b02826.

[79] L. Janker, Y. Tong, L. Polavarapu, J. Feldmann, A. S. Urban, and H. J. Krenner, "Real-time electron and hole transport dynamics in halide perovskite nanowires," *Nano Lett.*, vol. 19, no. 12, pp. 8701–8707, 2019, doi: 10.1021/acs.nanolett.9b03396.

[80] R. Peng *et al.*, "Long-range transport of 2D excitons with acoustic waves," *Nat. Commun.*, vol. 13, no. 1, pp. 1–7, 2022, doi: 10.1038/s41467-022-29042-9.

[81] C. P. Lee *et al.*, "Employing graphene acoustoelectric switch by dual surface acoustic wave transducers," *Sci. Rep.*, vol. 9, no. 1, pp. 1–9, 2019, doi: 10.1038/s41598-019-44689-z.

[82] F. Alsina, J. A. H. Stotz, R. Hey, and P. V. Santos, "Acoustically induced potential dots in GaAs quantum wells," *Solid State Commun.*, vol. 129, no. 7, pp. 453–457, 2004, doi:

TH-3353_166102010

10.1016/j.ssc.2003.11.014.

[83] T. Sogawa, H. Sanada, H. Gotoh, H. Yamaguchi, S. Miyashita, and P. V. Santos, "Spatial and temporal modulation of exciton photoluminescence properties in GaAs/AlAs dynamic quantum dots formed by surface acoustic waves," *Phys. Rev. B - Condens. Matter Mater. Phys.*, vol. 80, no. 7, pp. 1–8, 2009, doi: 10.1103/PhysRevB.80.075304.

[84] M. M. De Lima, R. Hey, J. A. H. Stotz, and P. V. Santos, "Acoustic manipulation of electron-hole pairs in GaAs at room temperature," *Appl. Phys. Lett.*, vol. 84, no. 14, pp. 2569–2571, 2004, doi: 10.1063/1.1695636.

[85] S. Giannini and J. Blumberger, "Charge transport in organic semiconductors: The perspective from nonadiabatic molecular dynamics," *Acc. Chem. Res.*, vol. 55, no. 6, pp. 819–830, 2022, doi: 10.1021/acs.accounts.1c00675.

[86] H. Dong and W. Hu, "Multilevel investigation of charge transport in conjugated polymers," *Acc. Chem. Res.*, vol. 49, no. 11, pp. 2433–2435, 2016, doi: 10.1021/acs.accounts.6b00368.

[87] V. Coropceanu, J. Cornil, D. A. da S. Filho, Y. Olivier, R. Silbey, and J.-L. Bredas, "Charge transport in organic semiconductors," *Chem. Rev.*, vol. 107, no. 4, pp. 926–952, 2012, doi: 10.1007/128_2011_218.

[88] M. Koopmans *et al.*, "Electrical conductivity of doped organic semiconductors limited by carrier-carrier interactions," *ACS Appl. Mater. Interfaces*, vol. 12, no. 50, pp. 56222–56230, 2020, doi: 10.1021/acsami.0c15490.

[89] B. A. Weir, E. A. Marseglia, S. M. Chang, and A. B. Holmes, "Changes in structure and morphology in the conjugated polymer MEH-PPV," *Synth. Met.*, vol. 101, no. 1, pp. 154–155, 1999, doi: 10.1016/S0379-6779(98)00560-8.

[90] N. A. N. Ismail, S. Shaari, N. Juhari, N. Sabani, M. F. Ahmad, and N. F. Zakaria, "Temperature effects on electrical and structural properties of MEH-PPV/PEIE OLED Device," *J. Phys. Conf. Ser.*, vol. 1535, no. 1, p. 012020, 2020, doi: 10.1088/1742-6596/1535/1/012020.

[91] B. S. Ong, Y. Wu, P. Liu, and S. Gardner, "High-performance semiconducting polythiophenes for organic thin-film transistors," *J. Am. Chem. Soc.*, vol. 126, no. 11, pp. 3378–3379, 2004, doi: 10.1021/ja039772w.

[92] P. V. Necliudov, M. S. Shur, D. J. Gundlach, and T. N. Jackson, "Contact resistance in pentacene thin film transistors," *Solid State Electron.*, vol. 47, no. 2, pp. 259–262, 2001, doi: 10.1109/ISDRS.2001.984512.

[93] K.-J. Baeg *et al.*, "High mobility top-gated poly(3-hexylthiophene) field-effect transistors with high work-function Pt electrodes," *Thin Solid Films*, vol. 518, no. 14, pp. 4024–4029, 2010, doi: 10.1016/j.tsf.2010.01.026.

[94] K. Baeg, G. Bae, and Y. Noh, "Efficient charge injection in p - type polymer field-effect

TH-3353_166102010

transistors with low-cost molybdenum electrodes through V_2O_5 interlayer," *ACS Appl. Mater. Interfaces*, vol. 5, no. 13, pp. 5804–5810, 2013.

[95] V. P. Liyana, A. M. Stephania, K. Shiju, and P. Predeep, "Influence of gate dielectrics, electrodes and channel width on OFET characteristics," *J. Phys. Conf. Ser.*, vol. 619, no. 1, pp. 2–6, 2015, doi: 10.1088/1742-6596/619/1/012029.

[96] Y. Lin *et al.*, "Improved performances of inkjet-printed poly(3-hexylthiophene) organic thin-film transistors by inserting an ionic self-assembled monolayer," *RSC Adv.*, vol. 6, no. 47, pp. 40970–40974, 2016, doi: 10.1039/c6ra02032a.

[97] D. Gargi, R. J. Kline, D. M. Delongchamp, D. A. Fischer, M. F. Toney, and B. T. O'Connor, "Charge transport in highly face-on Poly(3-hexylthiophene) films," *J. Phys. Chem. C*, vol. 117, no. 34, pp. 17421–17428, 2013, doi: 10.1021/jp4050644.

[98] T. L. Benanti and D. Venkataraman, "Organic solar cells : An overview focusing on active layer morphology," *Photosynth Res .*, vol. 87, pp. 73–81, 2006, doi: 10.1007/s11120-005-6397-9.

[99] A. L. Briseno *et al.*, "Self-assembly , molecular packing , and electron transport in n-type polymer semiconductor nanobelts," *Chem. Mater.*, pp. 4712–4719, 2008.

[100] A. R. Aiyar, J. Il Hong, and E. Reichmanis, "Regioregularity and intrachain ordering: Impact on the nanostructure and charge transport in two-dimensional assemblies of poly(3-hexylthiophene)," *Chem. Mater.*, vol. 24, no. 15, pp. 2845–2853, 2012, doi: 10.1021/cm202700k.

[101] Y. Yao, H. Dong, and W. Hu, "Ordering of conjugated polymer molecules: Recent advances and perspectives," *Polym. Chem.*, vol. 4, no. 20, pp. 5197–5205, 2013, doi: 10.1039/c3py00131h.

[102] C. Luo *et al.*, "General strategy for self-assembly of highly oriented nanocrystalline semiconducting polymers with high mobility," *Nano Lett.*, vol. 14, no. 5, pp. 2764–2771, 2014, doi: 10.1021/nl500758w.

[103] F. C. Tang *et al.*, "Alignment of poly(3,4-ethylenedioxythiophene) polymer chains in photovoltaic cells by ultraviolet irradiation," *J. Mater. Chem.*, vol. 22, no. 42, pp. 22409–22417, 2012, doi: 10.1039/c2jm34556k.

[104] Y. Yang, K. Mielczarek, A. Zakhidov, and W. Hu, "Effects of nanostructure geometry on polymer chain alignment and device performance in nanoimprinted polymer solar cell," *Org. Photonic Mater. Devices XV*, vol. 8622, no., p. 862211, 2013, doi: 10.1117/12.2008394.

[105] D. M. Delongchamp *et al.*, "Variations in semiconducting polymer microstructure and hole mobility with spin-coating speed," *Chem. Mater*, vol. 17, no. 23, p. 5610, 2005.

[106] M. Liu *et al.*, "Controlling morphology and aggregation in semiconducting polymers: The role of solvents on lasing emission in poly[2-methoxy-5-(20-ethylhexyloxy)- 1,4-phenylene-vinylene]," *Materials (Basel).*, vol. 10, no. 7, pp. 1–14, 2017, doi:

TH-3353_166102010

10.3390/ma10070706.

[107] D. S. Yang, K. Chung, and J. Kim, “Controlled alignment of polymer chains near the semiconductor-dielectric interface,” *Org. Electron.*, vol. 76, p. 105484, 2020, doi: 10.1016/j.orgel.2019.105484.

[108] D. H. Kim, Y. Jang, Y. D. Park, and K. Cho, “Controlled one-dimensional nanostructures in poly(3-hexylthiophene) thin film for high-performance organic field-effect transistors,” *J. Phys. Chem. B*, vol. 110, no. 32, pp. 15763–15768, 2006, doi: 10.1021/jp062899y.

[109] M. V. Kakade, S. Givens, K. Gardner, K. H. Lee, D. B. Chase, and J. F. Rabolt, “Electric field induced orientation of polymer chains in macroscopically aligned electrospun polymer nanofibers,” *J. Am. Chem. Soc.*, vol. 129, no. 10, pp. 2777–2782, 2007, doi: 10.1021/ja065043f.

[110] S. Nagamatsu *et al.*, “Backbone arrangement in ‘friction-transferred’ regioregular poly(3-alkylthiophene)s,” *Macromolecules*, vol. 36, no. 14, pp. 5252–5257, 2003, doi: 10.1021/ma025887t.

[111] D. Cui, H. Li, H. Park, and X. Cheng, “Improving organic thin-film transistor performance by nanoimprint-induced chain ordering,” *J. Vac. Sci. Technol. B Microelectron. Nanom. Struct.*, vol. 26, no. 6, pp. 2404–2409, 2008, doi: 10.1116/1.3013301.

[112] T. Kimura, H. Ago, M. Tobita, S. Ohshima, M. Kyotani, and M. Yumura, “Polymer composites of carbon nanotubes aligned by a magnetic field,” *Adv. Mater.*, vol. 14, no. 19, pp. 1380–1383, 2002.

[113] W. M. Gibbons, P. J. Shannon, S.-T. Sun, and B. J. Swetlin, “Surface-mediated alignment of nematic liquid crystals with polarised laser light,” *Nature*, vol. 351, pp. 49–50, 1991.

[114] Y. Xi and L. D. Pozzo, “Electric field directed formation of aligned conjugated polymer fibers,” *Soft Matter*, vol. 13, no. 21, pp. 3894–3908, 2017, doi: 10.1039/c7sm00485k.

[115] J. M. J. LaFreniere, E. J. Roberge, and J. M. Halpern, “Review— Reorientation of polymers in an applied electric field for electrochemical sensors,” *J. Electrochem. Soc.*, vol. 167, no. 3, p. 037556, 2020, doi: 10.1149/1945-7111/ab6cfe.

[116] F. Tassinari, S. P. Mathew, C. Fontanesi, L. Schenetti, and R. Naaman, “Electric-field-driven alignment of chiral conductive polymer thin films,” *Langmuir*, vol. 30, no. 16, pp. 4838–4843, 2014, doi: 10.1021/la500657e.

[117] Y. Xi and L. D. Pozzo, “Electric field directed formation of aligned conjugated polymer fibers,” *Soft Matter*, vol. 13, no. 21, pp. 3894–3908, 2017, doi: 10.1039/c7sm00485k.

TH-3353_166102010

Chapter 2

Simulation, Fabrication and Characterisation of SAW Devices

In today's world, SAW devices are used widely for applications ranging from passive sensors to wireless communications. As a result, theoretical simulation and modelling of these devices become fundamental, significantly impacting the development of SAW devices. Several modelling techniques, including the coupling-of-mode (COM) approach, equivalent circuit method, impulse response method, delta function method, and P-matrix method[1], [2], are available to characterise the function of IDTs constructed on the piezoelectric substrate in a SAW device. This chapter describes the 3D-Finite element simulation using COMSOL Multiphysics 5.3 for Rayleigh SAW resonator devices, their fabrication process, and the outcomes of the RF characterisation needed for this thesis work. The SAW resonator devices were developed and fabricated utilising negative photoresist-based UV-photolithography on YZ $LiNbO_3$ piezoelectric substrates. The Centre for Nanotechnology, IIT Guwahati, India, used an ISO5 (class 100) and ISO6 (class 1000) cleanroom facilities to fabricate the devices. Vector network analyzer (VNA) and RF probe stations were used to characterise SAW devices, and the input reflection coefficient, S_{11}, was evaluated. Comparisons were made between the resonance frequencies found through the theoretical estimation, Eigenmode analysis from simulation, and experimental observations in the manufactured SAW devices.

2.1 Finite element simulation

The finite element method (FEM) is a numerical approach for doing finite element analysis (FEA) of any given physical phenomenon. It is frequently used to solve partial differential equations that regulate natural phenomena. It has proved helpful in finding solutions to

TH-3353_166102010

challenging issues in various domains, including fluid flow, heat transfer, electrochemistry, optics, acoustics, and structural mechanics[3], [4]. Finite element (FE) simulation of a specific device can be performed using the constituent material properties of the designated geometrical structure with the enormously popular simulation tool COMSOL Multiphysics[5], [6]. In COMSOL Multiphysics, the appropriate device structure can be created in 2D or 3D, and the material properties and a set of interdisciplinary physics can be provided. For a set of applied boundary conditions, the response of the device to an excitation source can then be visualised. Over the years, several FE simulations in 2D and 3D have been performed[7], [8]. In this thesis, SAW resonator devices are simulated with the help of the COMSOL Multiphysics 5.3 software, which includes modules for solid mechanics, electrostatics, and piezoelectric multiphysics. A typical SAW device has vast dimensions, which increases the computational time for solving equations. FEM splits a large complex system into smaller parts known as finite elements, and accurate approximations are typically applied to lower the size of the device structure. A SAW device consists of IDTs which are periodic metal electrodes with specific widths and gaps between them. Infinite periodic boundary conditions taking one wavelength, λ, of the geometry, or anti-periodic boundary conditions for a geometry of one-half of the wavelength, $\lambda/2$, can be used to decrease this structure. Additionally, SAW propagates along its material surface, making it possible to simulate a depth of just a few wavelengths. These factors make computation easier and take less time, but the simulation still includes the necessary resonance frequency analysis for all SAW modes.

2.1.1 Eigenmode analysis

The eigen frequency analysis was done for the geometry with three different IDT finger widths. FE simulations were started by defining the dimensions of each unit cell and materials for each domain. Figure 2.1 shows the geometry of a SAW resonator used for the COMSOL simulation. Aluminium was used as the material for the IDT domain, and YZ $LiNbO_3$ was used as the piezoelectric substrate. Several material parameters were applied, including density, Poisson's ratio, Young's modulus, elasticity matrix, coupling matrix, and relative permittivity. The sides of the geometry were then selected with the required boundary conditions. The structure was then applied to meshing using free triangular pieces. The natural vibrational frequencies associated with the specified geometry were finally determined using eigenmode analysis. For this analysis, the IDT was kept at open or short instead of any voltage application.

TH-3353_166102010

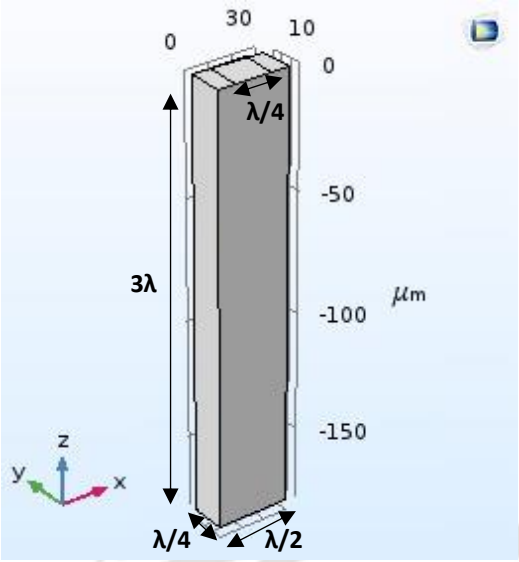

Figure 2.1: SAW resonator geometry used for COMSOL simulation.

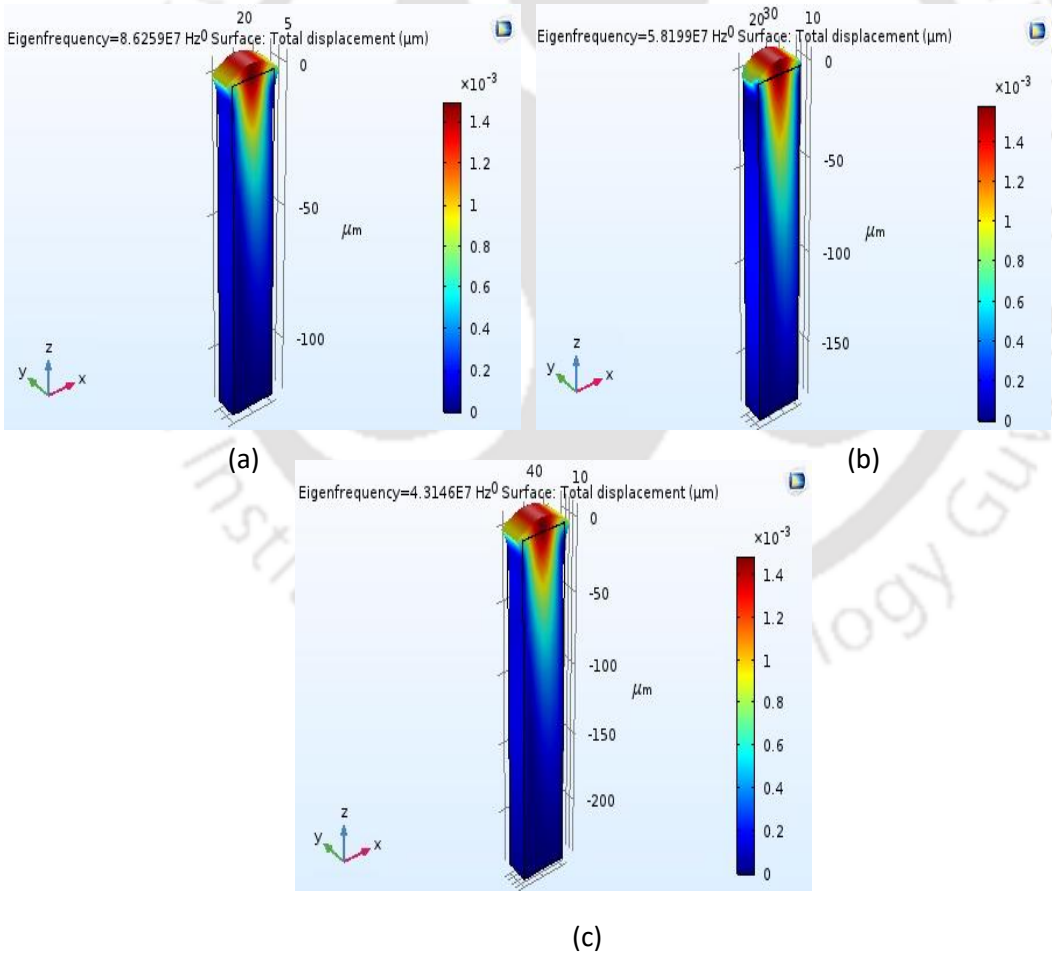

Figure 2.2: COMSOL Multiphysics 5.3 simulation displaying the displacement profiles (in μm) of the Rayleigh SAW modes at the resonance frequencies corresponding to wavelength, λ equal to (a) 40 μm, (b) 60 μm, and (c) 80 μm, obtained for YZ $LiNbO_3$.

TH-3353_166102010

This analysis determines the solutions to the underlying differential equations and provides the values of eigen frequencies with corresponding shape and surface displacement for the different wave modes. An aluminium IDT of finger width equal to 10 µm, 15 µm, and 20 µm on the piezoelectric substrates of YZ $LiNbO_3$ was simulated to generate a Rayleigh SAW of wavelength equal to 40 µm, 60 µm and 80 µm, respectively. The total displacement profile of the Rayleigh SAW modes for the three geometries at their resonance frequencies is shown in Figure 2.2. The figure shows that the maximum deformation occurs at the IDT area at the resonance frequency and that the maximum displacement limits up to one wavelength from the surface.

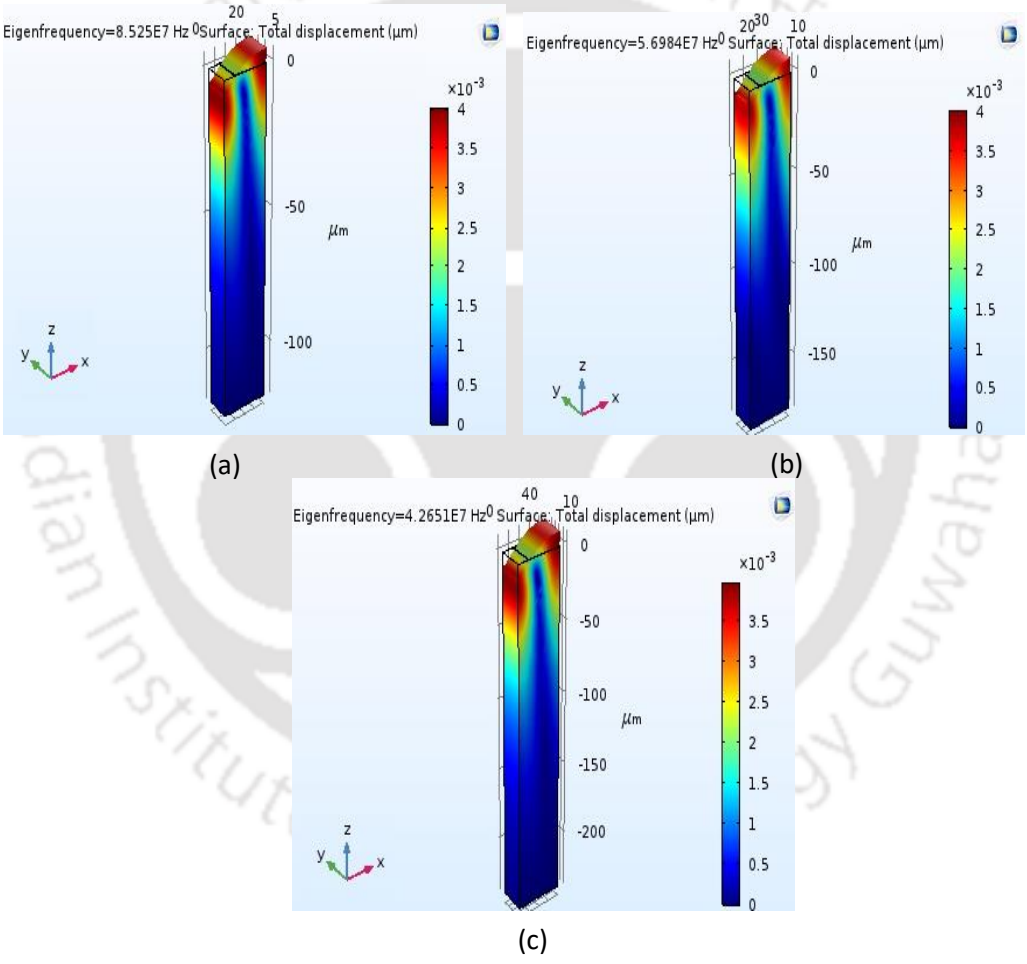

Figure 2.3: COMSOL Multiphysics 5.3 simulation displaying the displacement profiles (in µm) of the Rayleigh SAW modes at the anti-resonance frequencies corresponding to wavelength, λ equal to (a) 40 µm, (b) 60 µm, and (c) 80 µm, obtained for YZ $LiNbO_3$.

We know that frequency, *f*, is represented as *f* = (velocity/λ); therefore, resonance frequencies calculated assuming velocity of 3488 m/s for YZ $LiNbO_3$ for λ = 40 µm, 60 µm and 80 µm are 87.20 MHz, 58.13 MHz and 43.60 MHz, respectively [1] and corresponding frequencies

TH-3353_166102010

obtained from COMSOL simulations are 85.25 MHz, 56.98 MHz and 42.65 MHz, respectively. The displacement profile of the Rayleigh SAW modes at the anti-resonance frequencies for each of the three geometries is shown in Figure 2.3. All of the devices display behaviour that is in good agreement with the predicted values for the IDT finger width and $LiNbO_3$ substrate.

2.1.2 Frequency analysis

The maximum and minimum admittance at the resonance and anti-resonance frequencies were determined through the frequency analysis. It can be seen in Figure 2.4 that the admittance varies for a specific range of applied input signal frequencies.

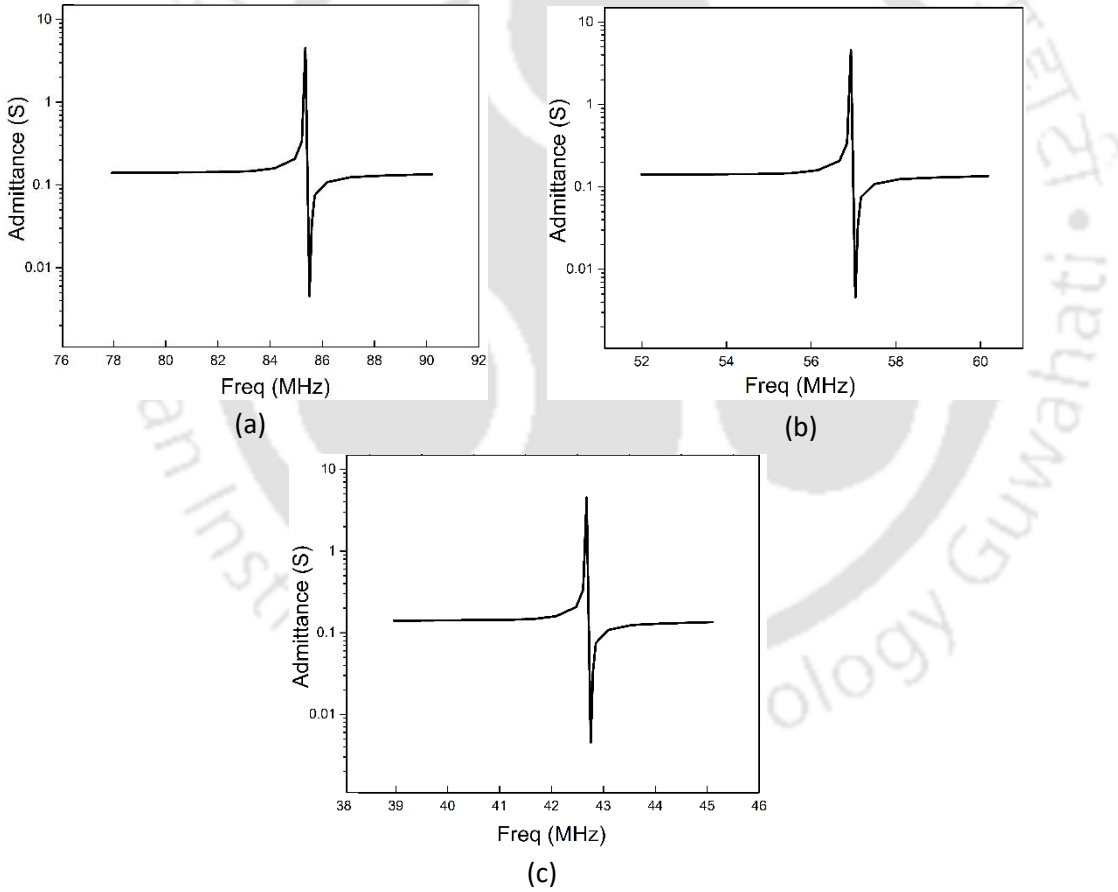

Figure 2.4: Variation of admittance values for IDT finger widths of (a) 10 µm, (b) 15 µm, and (c) 20 µm.

Supporting the results of the eigenmode analysis, a peak was seen at the resonance frequency, suggesting a maximum admittance of around 10 Siemens. In contrast, a drop was seen at the anti-resonance frequency, indicating minimum admittance of roughly 10^{-2} Siemens.

TH-3353_166102010

2.2 Fabrication of SAW resonator

The SAW resonator devices were fabricated using a negative photolithography approach. In order to start with the photolithography process, the layout of the device was first designed. Subsequently, a hard photomask containing the layout design was prepared, and it was then used to directly expose UV light via the patterned design onto photoresist-coated piezoelectric substrates. Substrates that had been patterned with metal were then used in constructing various organic semiconductor-based devices integrated with SAW. The particulars of this process are discussed in the chapters to follow.

2.2.1 Layout & mask design

The CleWin software was used to graphically design the single IDT structure layout for the SAW resonator geometry. The IDT consisted of finger width and gap equal to $\lambda/4$. Ground-source-ground (GSG) contact of 150 µm pitch was designed to connect the GSG probe of the RF probe station during the characterization of devices. A total of 20 IDT pairs, N_p were designed for the RF port along with a single electrode at a distance from the RF port. The distance of the single electrode from the RF port is kept at 100-125λ. This design with a single electrode has been used in the work discussed in Chapter 3. Figure 2.5 depicts the final layout design. Using the equation of aperture optimization [9], the required values of the set of parameters for the SAW resonator, as mentioned above, were finalised taking the input resistance, $R_{in,}$ close to 50 Ω and thus, assuring port matching at a later stage while doing RF characterization with VNA.

$$W_a = \left(\frac{1}{R_{in} \times 2 \times f_0 \times C_s \times N_p}\right)\left(\frac{4k^2 N_p}{(4k^2 N_p)^2 + \pi^2}\right) \tag{2.1}$$

Here, f_0 is the resonance frequency, N_p is the number of finger pair, C_s is the capacitance per unit length of a single finger pair, and k^2 is the electromechanical coefficient of the $LiNbO_3$ substrate.

Table 2.1 lists the optimized IDT parameters used in the fabricated devices for all three wavelengths. The design of the layout for the hard photomask is shown in Figure 2.5. The photomask is made out of soda lime glass coated with iron oxide at a thickness of 500 Å and has a layer of AZ 1518 photoresist put on top of it, having a thickness of 5300 Å. Following

TH-3353_166102010

the exposure with the Dilase 250- Kloe direct laser writing equipment, the iron oxide photomask was developed with the AZ326 MIF developer solution for 10 seconds, and the laser exposed area was etched in iron oxide etchant solution for an additional 10 seconds. After each treatment with the solution, the mask was thoroughly rinsed with DI water and dried with nitrogen blow.

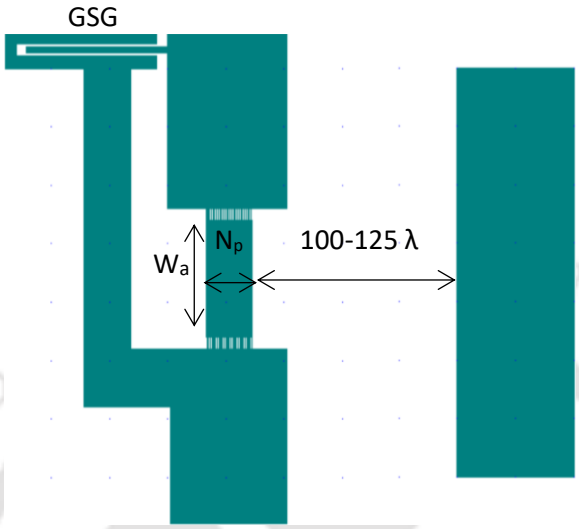

Figure 2.5: Device layout design of a SAW resonator for the photomask.

Table 2.1: Optimized IDT parameters for the fabricated devices.

IDT finger widths (µm)	Substrate	Capacitance, C_s (pF/cm)	Resonance frequency, f_0 (MHz)	Aperture width, W_a (mm)
10	$LiNbO_3$	4.6	86.2	1.9
15			58.2	2.9
20			43.1	3.89

TH-3353_166102010

2.2.2 Photolithography

The SAW resonator device has been designed and fabricated on YZ $LiNbO_3$ using a negative photoresist-based photolithography approach. Figure 2.6(a) shows the basic process flow of the fabrication.

1. Firstly, YZ $LiNbO_3$ wafers were cleaned using acetone and isopropyl alcohol (IPA) and dried using N_2 gas.
2. Aluminium was deposited on the substrate surface through a thermal evaporator under a high vacuum (~10^{-6} torr).
3. The substrates were then annealed on a hot plate for 10–15 mins by gradually increasing the temperature to 110°C and then cooled down to room temperature.
4. Al deposited substrates were spin-coated with HMDS primer at 4000 rpm for 60 s and annealed at 175°C for 10 mins.
5. After cooling to room temperature, the substrates were coated with negative photoresist (SU8 -2002) at 4500 rpm for 60 s and then soft baked at 110°C for 1 min.
6. Substrates were then exposed through the hard mask for 4 seconds using the Kloe direct UV exposure unit and then baked at 110 °C for 3 mins.
7. The substrate was then developed in the SU8 developer and IPA solutions to get the IDT pattern.
8. The patterned substrates were hard baked by gradually increasing the temperature to 150°C and baking it for 10 minutes. The substrates were then left to cool down to room temperature.
9. Later, aluminium was etched from the UV-exposed area using an aluminium etchant (H_2O: H_3PO_4: HNO_3 = 4:19:1), and the photoresist was removed by dipping it in a photoresist removal solution [10] at 150 °C.
10. SAW resonators with IDT of 10 µm, 15 µm and 20 µm finger widths were fabricated for this thesis work. Figure 2.6(b) shows the optical image of the IDT electrode with finger width and gap for $\lambda/4$ = 10 µm.

TH-3353_166102010

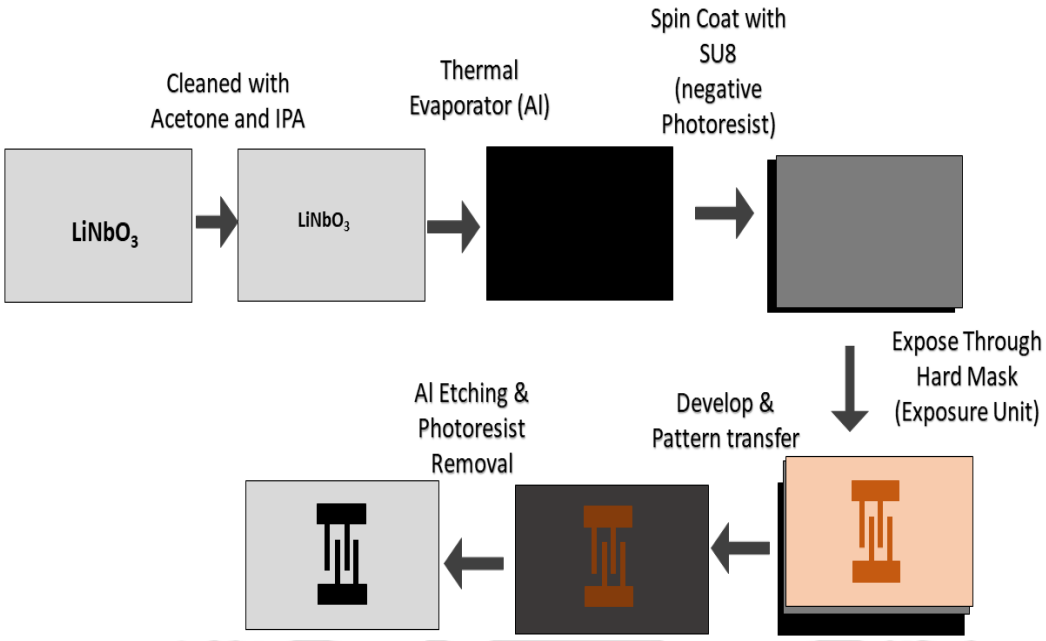

(a)

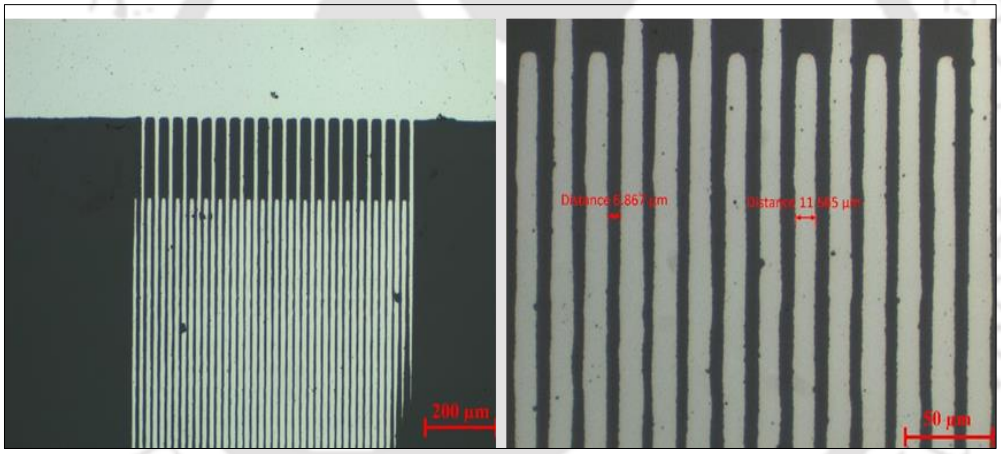

(b)

Figure 2.6: (a) Fabrication flow of the photolithography process. (b) Optical images of the IDT of finger width 10 µm fabricated for the thesis work.

2.3 Characterization of SAW resonator

The performance of the SAW device was evaluated by measuring the S-parameters of the IDT using a Keysight PNA-L Network Analyzer (Vector Network Analyzer) (Model number: PNA-L N5232A, Frequency range: 300 kHz to 20 GHz) and a Cascade MPS 150 RF probe station (two RF probes of GSG pitch: 150 m, four SMUs accompanying DC). All of the

TH-3353_166102010

measurements were carried out at room temperature. The values found through characterisation agree well with the theoretical and simulation estimation validating the fabrication.

2.3.1 Port matching

To make a SAW device function efficiently, port matching is crucial. In most cases, SAW transducers are built to have an input impedance close to 50 ohms and equal to the characteristic impedance, Z_0. The port matching ensures no return loss once the device has been connected to the RF signal source. However, exact port impedance matching can be challenging to achieve at times. This is because the IDT structure has a significant capacitance, and there can be anomalies in the fabrication process. As a result, port matching is typically accomplished by connecting a two-component *LC* matching network to the RF signal source and the SAW device under test (the DUT), as depicted in Figure 2.7.

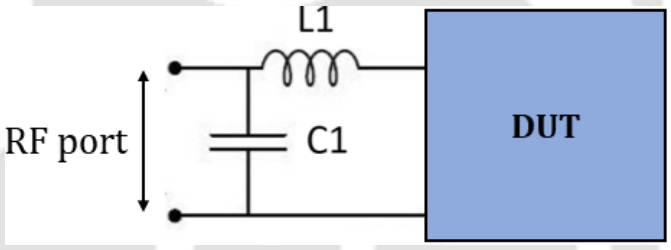

Figure 2.7: *LC* matching circuit for a one port network.

Table 2.2: *LC* parameters used to perform port matching in the fabricated devices

IDT finger width (μm)	Substrate	Impedance (Ω)	Matching network	
			L (nH)	*C* (pF)
10	$LiNbO_3$	(45.63-j1.88)	29.61	11.45
15		(42.03-j54.12)	204.7	24.62
20		(46.34-j20.2)	124.2	21.02

After the matching has been completed, the maximum power from the RF source is delivered to the SAW device, which reduces the amount of signal that is reflected. The unmatched SAW

TH-3353_166102010

device was first characterised, and then a virtual port matching in the VNA was carried out by computing the inductance, *L*, and capacitance, *C* values using the observed smith chart of the unmatched device. The matched SAW device was characterised after port matching. Table 2.2 presents the port matching network characteristics for SAW devices made with different IDT widths. The *LC* components were used in the shunt capacitor and series inductance arrangement.

2.3.2 Resonance frequency analysis

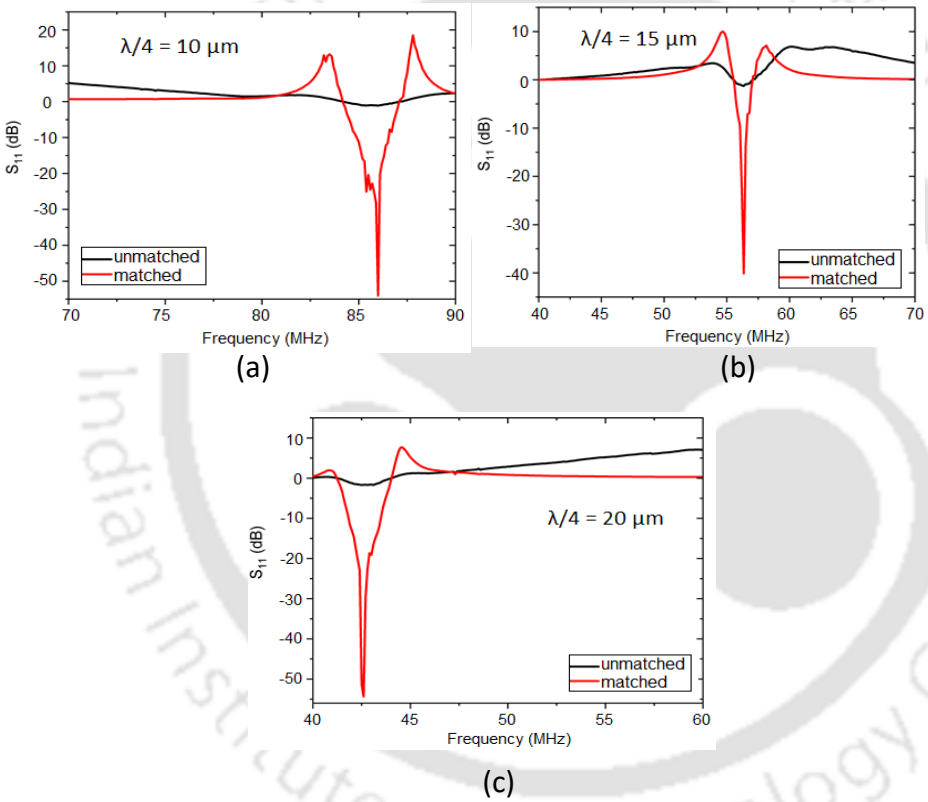

Figure 2.8: S_{11} (dB) plots of Rayleigh SAW devices fabricated on YZ $LiNbO_3$ substrates having IDT electrode width equal to (a) 10 µm, (b) 15 µm, and (c) 20 µm.

The input reflection coefficient, denoted by S_{11}, was determined for the Rayleigh SAW resonator devices. Figure 2.8 depicts the frequency response before and after the port matching and illustrates the resonance frequency peaks corresponding to the IDT of various finger widths. The YZ $LiNbO_3$ had a resonance frequency of 86 MHz for a wavelength $\lambda = 40$ µm. In addition, for YZ $LiNbO_3$, resonance frequencies of 56.3 MHz and 42.56 MHz were obtained when the wavelength was equal to 60 µm and 80 µm, respectively. Table 2.3 compares the resonance

TH-3353_166102010

frequency values acquired theoretically, via simulation, and experimentally. This comparison reveals that the experimental frequency values differ slightly from the simulated and theoretical values.

Table 2.3: Comparison of resonance frequency values

IDT finger width (µm)	Resonance frequency (MHz)		
	Experimental	Theoretical	Simulation
10	85.6	87.2	86.2
15	56.3	58.1	56.9
20	42.6	43.6	43.1

2.4 Summary

The chapter describes the FE simulation process for Rayleigh SAW resonator devices using COMSOL Multiphysics 5.3. Here, the resonance frequency of the corresponding wave has been evaluated using eigenmode analysis of the simulated SAW devices. All the required approximations for the simulation geometry, boundary conditions, and Euler angles have been considered. Subsequently, a thorough description of the photolithographic fabrication procedure for the resonator devices has been presented. The design of the necessary device structure as well as the optimization of the aperture width and its effects on port matching, have been covered. The RF characterisation of the manufactured devices is examined next, and the values of the practically relevant *LC* components for port matching are listed.

TH-3353_166102010

2.5 References

[1] D. Morgan, *Surface Acoustic Wave Filters: With Applications To Electronic Communications And Signal Processing*. Academic Press, 2010.

[2] D. Royer and E. Dieulesaint, *Elastic Waves in Solids II: Generation, Acousto-Optic Interaction, Applications.*, 1st ed. Springer Science & Business Media, 1999.

[3] J. N. Reddy, *Introduction to the Finite Element Method*, 4th ed. McGraw-Hill Education, 1984.

[4] O. C. Zienkiewicz, R. L. Taylor, and J. Z. Zhu, *The Finite Element Method: Its Basis and Fundamentals*, 6th ed. Elsevier, 2005.

[5] A. Abdollahi, Z. Jiang, and S. A. Arabshahi, "Evaluation on mass sensitivity of saw sensors for different piezoelectric materials using finite element analysis," *IEEE Int. Symp. Appl. Ferroelectr.*, vol. 54, no. 12, pp. 734–737, 2007, doi: 10.1109/ISAF.2007.4393386.

[6] M. I. Rocha-Gaso, R. Fernández-Díaz, A. Arnau-Vives, and C. March-Iborra, "Mass sensitivity evaluation of a Love wave sensor using the 3D finite element method," *2010 IEEE Int. Freq. Control Symp. FCS 2010*, pp. 228–231, 2010, doi: 10.1109/FREQ.2010.5556338.

[7] S. Trivedi and H. B. Nemade, "ZnO nanorod-based Love wave delay line for high mass sensitivity: A finite element analysis," *IET Sci. Meas. Technol.*, vol. 13, no. 9, pp. 1245–1253, 2019, doi: 10.1049/iet-smt.2018.5239.

[8] R. Lerch, "Simulation of piezoelectric devices by two- and three-dimensional finite elements," *IEEE Trans. Ultrason. Ferroelectr. Freq. Control*, vol. 37, no. 3, pp. 233–247, 1990, doi: 10.1109/58.55314.

[9] W. C. Wilson and G. M. Atkinson, "Mixed modeling of a SAW delay line using VHDL," *BMAS 2006 - Proc. 2006 IEEE Int. Behav. Model. Simul. Work.*, pp. 34–39, 2006, doi: 10.1109/BMAS.2006.283466.

[10] J. H. Baik, C. I. Oh, S. D. Lee, W. L. Kim, and C. S. Yoo, "Photoresist remover composition," US006140027A, 2000.

TH-3353_166102010

Chapter 3

Acoustic Charge Transport in Organic Semiconductor Films

A SAW device typically consists of comb-shaped metal electrodes created on a piezoelectric substrate, known as an IDT, and when the IDT is excited by voltage, a SAW is produced that travels through the substrate at the speed of sound. The semiconductor formed on or in contact with a piezoelectric substrate experiences the strain and electric fields as a result of the SAW propagation, as discussed in the previous chapters. SAWs are employed in a process known as ACT [1]–[3] that transports charge carriers in a manner distinct from the conventional electric field drift. ACT is the charge transport assisted by SAW-induced travelling fields [4], [5]. SAW-semiconductor interaction leads to the spatial modulation[6] of energy bands in the semiconductor which creates potential wells [7] at the troughs and crusts of SAW, causing the charge carriers to accumulate in the potential wells and travel along with SAW. SAWs have been used to facilitate contactless charge transport in a range of electronic structures comprising silicon charge-coupled register devices [8], monolithic metal-insulator-semiconductor structures [9], low-dimensional quantum well [10] and two-dimensional electron gas systems [11]. Although numerous studies have supported the acoustic charge transfer in inorganic layers created on a piezoelectric substrate, the use of SAW to facilitate charge transport in organic semiconductors is still a relatively unexplored field.

Organic materials are widely available, cheap, and accessible to mass production using low-cost, high-volume, and room-temperature processes. Organic semiconductors have developed in recent years to become a competitive commercial alternative to more conventional inorganic materials. Understanding charge transport mechanisms in organic semiconductors has long been of interest to researchers. Correspondingly, a vast amount of research has been reported to improve the charge transport in organic semiconductors, predominantly by enhancing the film formation, which involves the introduction of dopant materials [12], the solvent used [13],

TH-3353_166102010

annealing effects [14] and morphology control [15]. All these methods can be considered an internal process of improving charge transport. However, no investigation of an externally induced charge transport in an organic semiconductor has ever been reported. Such a possibility can be facilitated by the incorporation of acoustic fields in organic material. The influence of the SAWs on the organic semiconductor's charge transport electrically and potentially will be an exciting feature to observe.

This chapter demonstrates the ACT of optically induced excitons in two organic semiconductors, P3HT and MEH-PPV, up to a distance of 3 mm. The device consists of a SAW resonator transmitting SAW through a polymer layer where ACT takes place and a polymer collector diode at the end to collect the charges. The voltage excitation is provided by applying a continuous RF signal using a Keysight PNA-L Network Analyzer (VNA) cascaded with MPS 150 RF probe station to the IDT on a piezoelectric YZ lithium niobate substrate producing Rayleigh SAW. Optical illumination up to 15 mW/cm^2 intensity is applied to induce excitons in the polymer layer deposited on the lithium niobate substrate. The charge transport was characterised in terms of direct current using the Keithley 4200A-SCS Parameter Analyzer with the source-measurement units (SMUs) connected to the two metal electrodes of the fabricated device. Acousto-optic characteristics such as the maximum charge capacity and charge transfer efficiency of the acoustic transport have also been defined and calculated. In addition, a theoretical analysis of charge carrier dynamics in the presence of a moving SAW field is also performed using a semi-classical Hamiltonian of the system.

3.1 Device fabrication

The device fabrication is configured in three parts: i) SAW resonator, ii) polymer layer, and iii) collector diode. SAW resonator structure consists of 20 pairs (N_p) of IDT of 20 µm finger width ($\lambda/4$) spaced at 20 µm and GSG contact for the RF probing. In contrast, a typical metal-semiconductor-metal (MSM) configuration with the extended polymer layer forms the collector diode. The first step in device fabrication was patterning the IDT and the bottom electrode (BE) of the collector diode using a negative photoresist photolithography approach. Aluminium, Al, was deposited through thermal evaporation (~10^{-6}) on clean samples of YZ $LiNbO_3$ piezoelectric substrates. IDT and BE were then patterned employing Kloe direct UV exposure unit with a hard photomask, SU-8 photoresist and Al etchant. The polymer film was coated in the space between IDT and BE, covering the BE shown in Figure 3.1. The film was then etched off from one side of the BE for probing as metal contact. Finally, the MSM collector diode was

TH-3353_166102010

completed at BE end by thermally depositing gold, Au as the top electrode (TE) at 8.4×10^{-6} mbar vacuum by shadow masking.

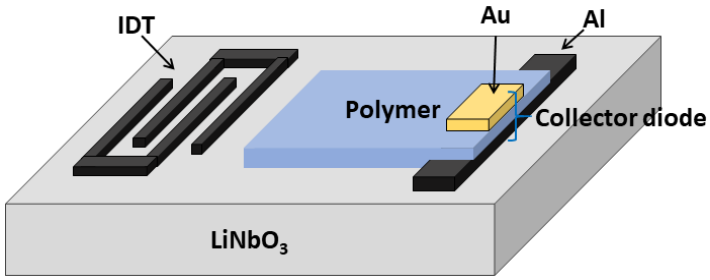

Figure 3.1: Schematic of the device fabricated to study ACT .

The charge transport was examined in two organic semiconductors, P3HT and MEH-PPV (commercially purchased from Sycon Polymers India Private Ltd. and Sigma Aldrich). A 10 mg/ml solution of the polymer in chlorobenzene was prepared by magnetically stirring the solution for 15–30 mins at a temperature of 50–70 ^{O}C and then cooled down to room temperature. Three types of polymer coatings were tested, viz. spin-coated P3HT, drop-casted P3HT and drop-casted MEHPPV. The thickness of the IDT and BE were measured using a surface profiler to be 180–200 nm and the Au electrode ~100 nm.

3.2 Theoretical analysis

An RF voltage excitation to the IDT causes strain in the piezoelectric substrate. The strain propagates on the surface of the elastic substrate resulting in the generation of SAW. The resonance condition is met when the applied frequency is equal to the resonance frequency of the device given as $f = \frac{v}{\lambda}$, where v is the phase velocity of the wave and λ is the periodicity in IDT [16]. The propagation of SAW causes acoustic deformations in the organic semiconductor deposited on the surface of the substrate, as shown in Figure 3.2, and instigates a shift in the energy bands of the organic semiconductor. The perturbation of the energy band leads to the establishment of a deformation potential which is proportional to the dilatation of the crystal [17]. The corresponding strain field will have a longitudinal (u_x) and traverse component (u_z) accompanied by an additional piezoelectric field (ζ_x, ζ_z) in the piezoelectric material.

TH-3353_166102010

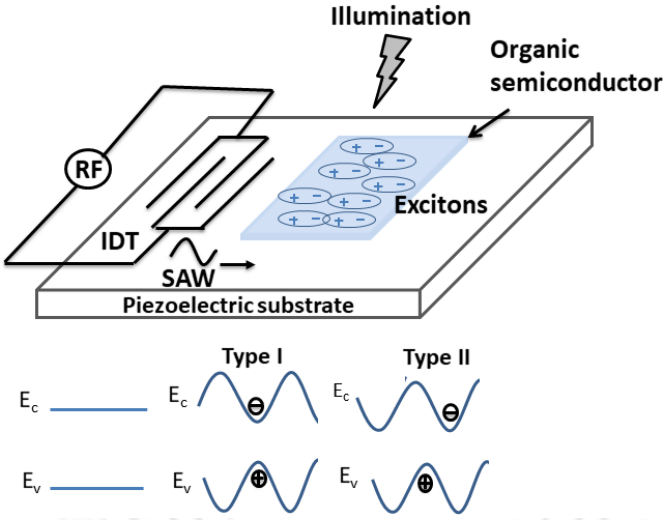

Figure 3.2: Schematic of device structure describing the energy band modulation leading to exciton splitting.

To understand the classical dynamics, we consider a travelling SAW of the form

$$\Phi = \Phi_0 \sin(kx-\omega t) \tag{3.1}$$

propagating in the positive x direction. Here, Φ is the SAW field strength, Φ_0 is the maximum amplitude of SAW, k is the wave number and $\omega = 2\pi f$ refers to the angular frequency. The deformation potential [2], [18] can be described as

$$V = c\nabla\Phi \tag{3.2}$$

and from equation (3.1), we can write

$$V = V_0 \cos(kx-\omega t) \tag{3.3}$$

where c and $V_0 = \frac{c\Phi_0}{k}$ are constant terms. The SAW field (consisting of both strain and piezoelectric fields) causes dynamic band-gap modulation [5], [19] in the organic semiconductor , as shown in Figure 3.2. The strain-induced type-I modulation [20] with the conduction band (CB) and valence band (VB) at the same SAW phase results in the formation of acoustic traps with a moving SAW potential [5], [16]. However, the piezoelectric fields with type-II modulation [21], where CB and VB are at different SAW phases, will cause ionization

TH-3353_166102010

of the excitons [22]. The SAW field will separate and confine the free carriers to the precincts analogous to the maxima and minima of the SAW. The equation of motion of electrons (or holes) exposed to the SAW field can be represented using Newton's equation of motion [23], [24]

$$\frac{d^2x}{d^2t} = \frac{q}{m}\frac{\partial V}{\partial x} \tag{3.4}$$

$$\frac{d^2x}{d^2t} + \frac{qV_0}{mk} sin(kx\text{-}\omega t) = 0 \tag{3.5}$$

where, q, m, x denote the charge, effective mass and coordinate of the charge carrier. The carrier dynamics can be described by formulating a model using a semi-classical Hamiltonian of the system. A solution to equation (3.5) will be of the form

$$x(t) = X(t) + \xi(X, \dot{X}, \omega t) \tag{3.6}$$

comprising of the slow part of the motion denoted by $X(t)$ and the fast part is represented by ξ. Neglecting the higher harmonics, the standard method of separation in time scales [25], [26] lets to choose a value of ξ such that the equation of motion for X is explicitly time independent. The carrier dynamics in a periodic system are usually described by a time dependent Hamiltonian [16], [26]

$$H(t) = \frac{p^2}{2m} + V_0 \, cos(kx\text{-}\omega t) \tag{3.7}$$

$H(t)$ is a periodic function where x and p represent the position and momentum of the particle. An effective time-independent Hamiltonian may be calculated up to the order of (ω^{-2}) to derive the slow dynamics of the motion. H_{eff} can be computed in a systematic expansion [25] as

$$H_{eff} = \frac{p^2}{2m} + V_0 \, cos^2(kx\text{-}\omega t) \tag{3.8}$$

The second term $V_0 cos^2(kx\text{-}\omega t) = V_0 \{\frac{1 + cos[2(kx\text{-}\omega t)]}{2}\}$ establishes the formation of time-independent acoustic traps with potential minima at $x = \frac{n\pi}{2}$ and maxima at $x = (n+1)\pi$

TH-3353_166102010

for $n = 0,1,2,\ldots$. Hence, modulation of energy bands will detain the electrons to the potential minima and holes to the potential maxima of the SAW. These spatially separated and captured carriers will be transported through the drift [27], [28] caused by the SAW field with the velocity of sound in the positive x direction.

3.3 Acousto-optic analysis

The experimental set-up consists of three parts: a VNA cascaded with an RF probe station to generate SAW, a parameter analyser with SMUs for measuring the current of the fabricated device, and a white light with a beam diameter of 3 mm and maximum intensity of 15 mW/cm^2 for the optical illumination. The IDT of the SAW resonator was excited using an RF signal source of 42 MHz, and Rayleigh waves were generated on the surface of YZ lithium niobate. The SAW propagates through the polymer material deposited on the substrate.

3.3.1 Photovoltaic current

The polymer layer between the IDT and the collector diode was illuminated to generate the excitons without the collector diode being exposed. The anticipated charge transport was characterised by measuring the photovoltaic current of the collector diode using Keithley 4200A-SCS Parameter Analyzer without applying a bias. The output current density for spin-coated P3HT as a function of time is plotted for the following four cases in Figure 3.3(a). 'No light no SAW': neither RF nor illumination applied; 'Only SAW': RF on and illumination off; 'Only light': illumination on and RF off; 'Light+SAW': both illumination and RF on. The measurements have been taken for the four cases in the order mentioned. It can be seen from Figure 3.3(a) that only for the 'Light+SAW' case, a current density of 7.5 nA/cm^2 is witnessed, and for the other three cases, no current is observed. The occurrence of current in the presence of both SAW and light clearly indicates the acoustically induced charge transport in the polymer material. Similar behaviour in current density has been seen for the drop-casted P3HT and MEH-PPV films as shown in Figure 3.3(b, c)). The current density value under the RF-on condition for the drop-casted film of P3HT is slightly lower than the spin-coated P3HT film, mainly because of the increased collection losses in the collector diode for the thicker active layer.

TH-3353_166102010

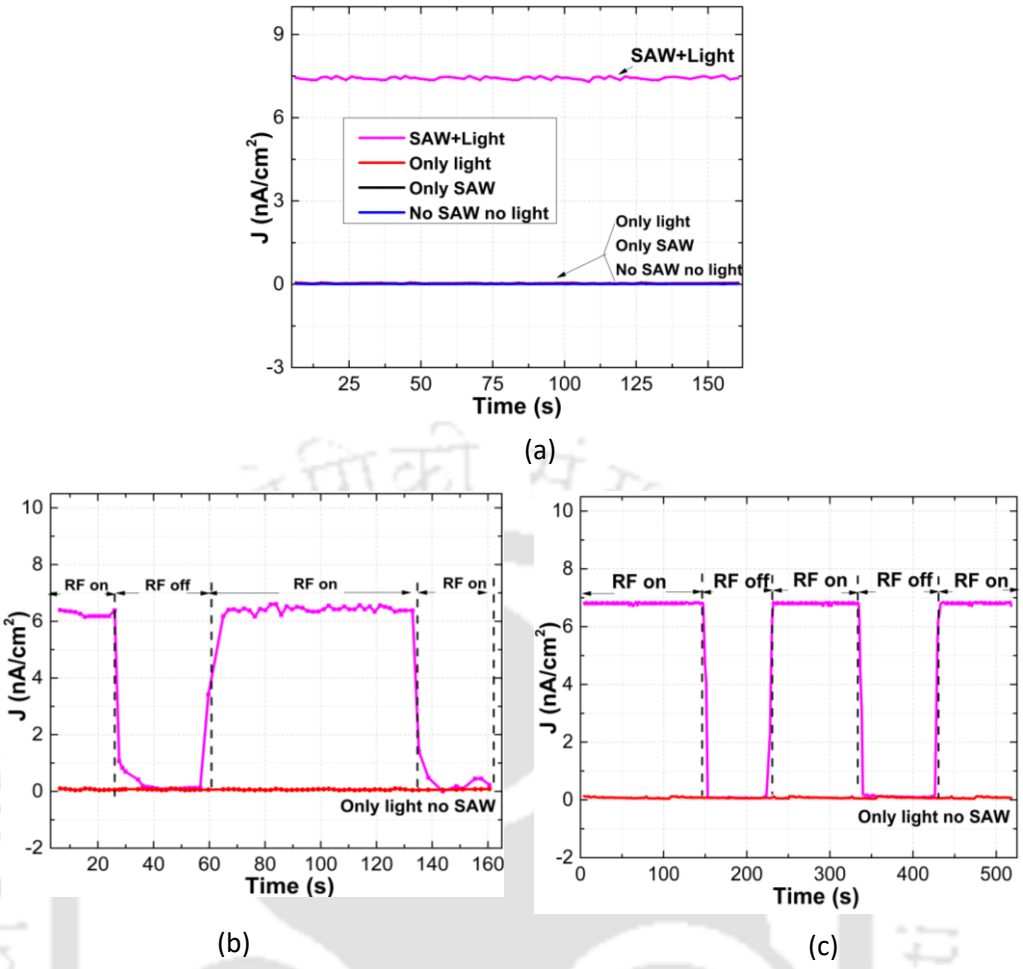

Figure 3.3: (a) Time response of current density measured in spin-coated P3HT for four modes without any applied bias. Current density for SAW and light with RF on and off for (b) P3HT and (c) MEH-PPV.

The travelling SAW field ionizes the optically created excitons in the polymer, preventing recombination [33], and drags the spatially separated charges to the collector diode, where they are completely dissociated and collected to produce current in photovoltaic mode. Figure 3.4 illustrates an atomic force microscope (AFM) image depicting the surface morphology of the spin-coated P3HT film, drop-casted P3HT, and drop-casted MEH-PPV film. The spin-coated P3HT film seems to have an average rms surface roughness of 3.24–3.4 nm, whereas the drop-casted P3HT and MEHPPV films exhibit rms surface roughness of 6.07 nm and 7.2 nm, respectively.

TH-3353_166102010

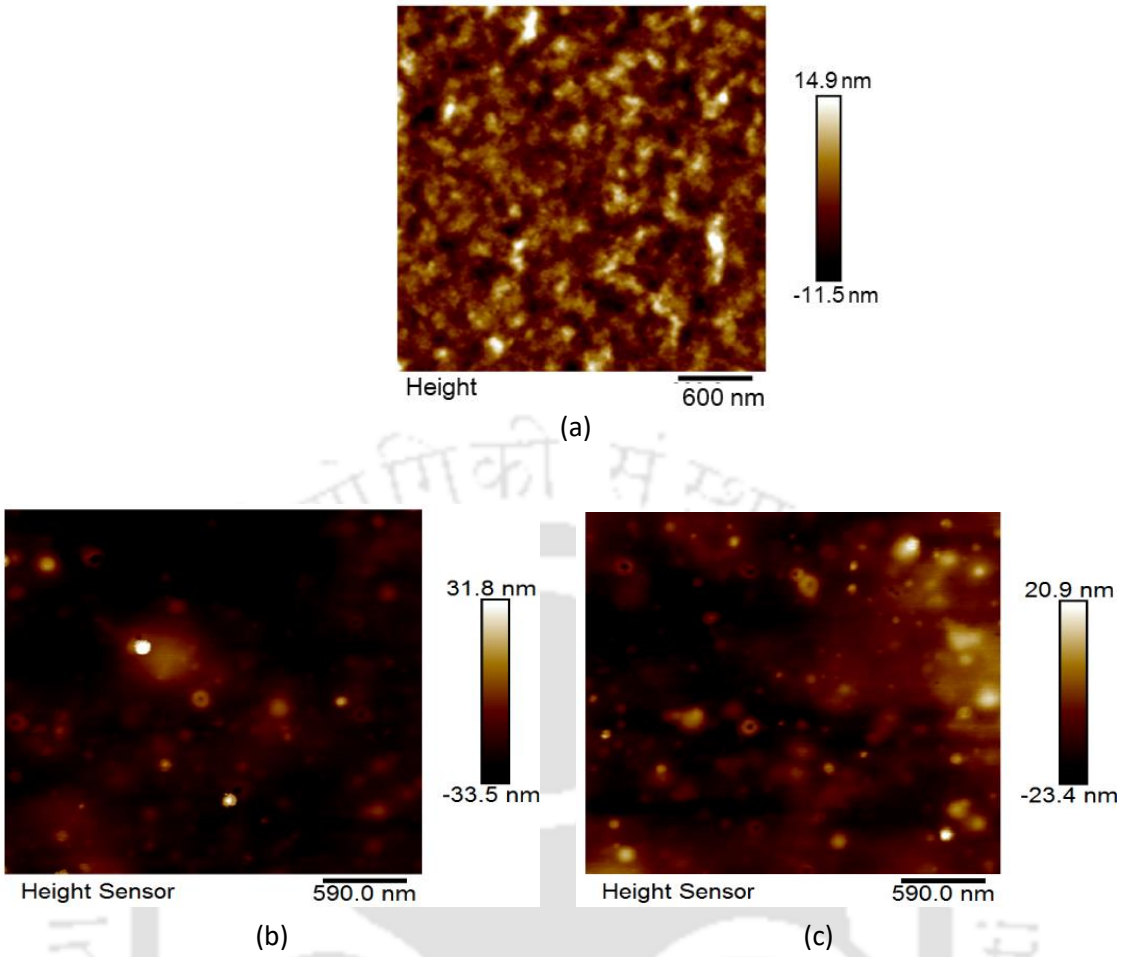

Figure 3.4: 3×3 μm^2 AFM image of (a) spin-coated P3HT film, and drop-casted film of (b) P3HT, and (c) MEH-PPV.

3.3.2 Photoluminescence study

The driving mechanism for the ACT is already discussed above in the section on Theoretical analysis. Consequently, the piezoelectric and strain fields of SAW are considered to be collectively contributing in providing energy (E_{SAW}) sufficient to overcome the exciton binding energy of the polymer and ionize the excitons. The ionization of excitons has been verified by conducting instantaneous photoluminescence (PL) measurements for P3HT and MEH-PPV in the absence of SAW and with RF powers of -15 dBm and -8 dBm, as shown in Figure 3.5.

TH-3353_166102010

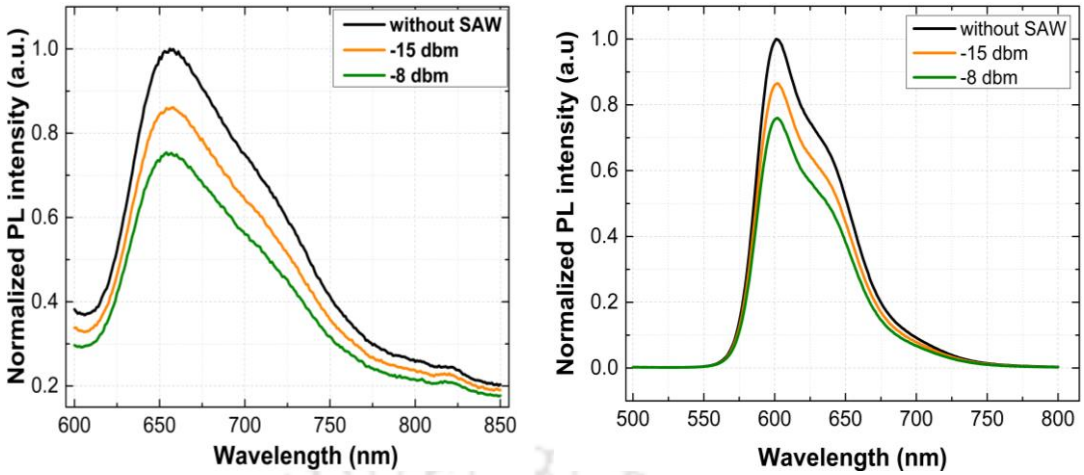

Figure 3.5: Instantaneous normalised PL showing the effect of SAW in exciton ionization in (a) P3HT and (b) MEH-PPV.

The decrease in the PL intensity in the presence of SAW implies that the SAW field has ionized the excitons and prevented recombination resulting in PL quenching. The drop in PL intensity observed in Figure 3.5(a) is 15% and 26%, respectively, for the SAW powers of -15 dBm and -8 dBm. As a result, it may be inferred that 15% and 26% of the photogenerated charges have been ionized, spatially separated by SAW with RF powers of -15 dBm and -8 dBm, respectively and then delivered to the collector diode. A similar trend can be seen from the PL intensity plot for MEH-PPV in Figure 3.5(b), having a drop of 14% and 25%, respectively, for the SAW powers of -15 dBm and -8 dBm. The effective reduction in the exciton binding energy in the presence of a SAW field ($\mathcal{E}_{SAW}$) can be written [29] as $\Delta E_{BE} = E_{BE}(0) - E_{SAW}$, where E_{SAW} is the energy obtained from the wave and $E_{BE}(0)$ is the binding energy of the polymer in absence of SAW. The energy density of the wave can be summed as the kinetic energy due to the piezoelectric field and potential energy from the elastic deformations of the wave [30]. Hence, the total energy offered by the wave to the polymer material can be defined as

$$E_{SAW} = \frac{1}{2} m^* (\mu\zeta)^2 + \frac{1}{2} \rho A^2 (\omega)^2 \qquad (3.9)$$

The first term is the kinetic energy gained by the charges in the piezoelectric field ζ and is given by

$$E_P = \frac{1}{2} m^* (\mu\zeta)^2 \qquad (3.10)$$

TH-3353_166102010

The second term, the maximum potential energy offered by the strain field, is given by

$$E_s = \frac{1}{2}\rho A^2(\omega)^2 \tag{3.11}$$

Here, m^* is the effective mass, μ is the mobility of the material, ρ is the density of the substrate, A is the amplitude of the SAW beam, and ω is the SAW frequency. Substituting the values of $m^* = 0.75\ m_0$, $\mu = 0.7$ cm^2/Vs [31]–[33], $\rho = 4650$ kg/m^3, $A = 1\ \lambda = 80\times10^{-6}$, $\omega = 42.6$ MHz and considering the exciton length as 1.5 Å [34], [35] and the effective reduction in the exciton binding energy, $E_{SAW} = 0.65$ eV≈ 0.7 eV. The computed value of E_{SAW} at -8 dBm falls within the reported values of $E_{BE}(0)$ in the range of 0.35–0.7 eV for the both the polymers [36]–[39]. The equivalence of E_{SAW} with E_{BE} of P3HT supports the fact that the total energy offered by SAW will be enough to ionize the optically induced excitons in P3HT. The current density values for MEHPPV shown in Figure 3.3 is close to that of P3HT as their exciton binding energies are close and are subdued by the SAW wave energy.

3.3.3 Acousto-optic characteristics

For the purpose of gaining an understanding of the acousto-optic charge properties, we developed a set-up where white light is projected through a slit. Figure 3.6(a) shows that for a fixed slit size of 700 μm, the current density varies linearly as a function of light intensity, and it saturates at light intensity beyond 13 mW/cm^2. The saturation of current is due to the compensation of the SAW field ($\mathcal{E}_{\mathrm{SAW}}$) by the field produced by photogenerated charges [29]. The field screening could therefore be characterised as the maximum number of charge carriers that a single acoustic wavelength can transport and deliver to the collector diode. For the calculation of the maximum charge capacity (N) and also the corresponding maximum output current, we considered that in the presence of the field of $\mathcal{E}_{SAW}$, the charges are separated in the crest and troughs of the equivalent SAW-induced field in the HOMO and LUMO levels of the organic semiconductor. As a result, the charges can be considered as two clusters of opposite charges ($Q = Nq$) separated by a distance of half acoustic wavelength, as shown in Figure 3.6(b). SAW force between the two clusters of charges can be written as

$$F_{SAW} = Nq\mathcal{E}_{SAW} \tag{3.12}$$

TH-3353_166102010

In addition, the electrostatic force between two clusters of charges separated by (λ/2) can be written as $F_E = \frac{k_e(Nq)^2}{\left(\frac{\lambda}{2}\right)^2}$, where k_e is the Coulomb's constant.

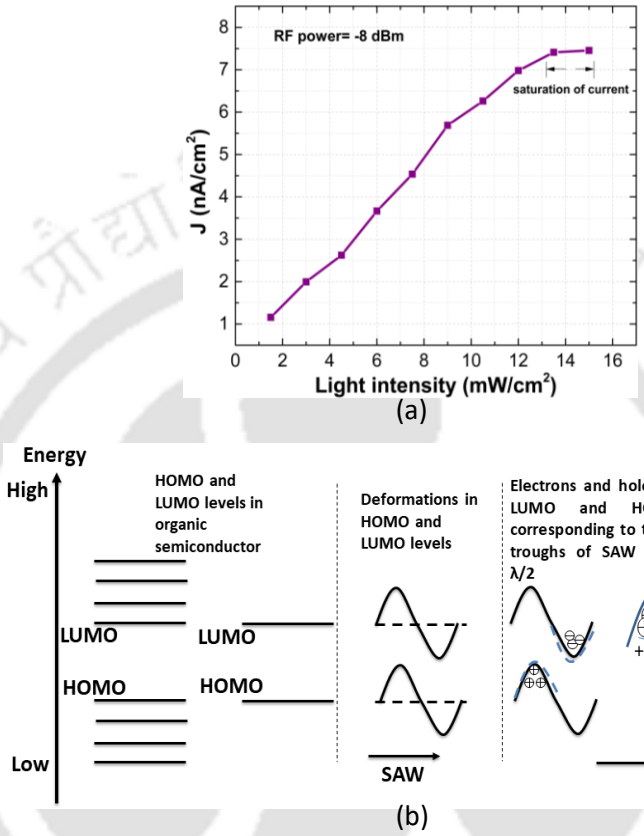

Figure 3.6: (a) Current density as a function of light intensity measured experimentally using a fixed width slit for SAW RF power -8 dBm. (b) Representation of charge separation as two clusters +Q and -Q under the influence of SAW in the HOMO and LUMO level of the organic semiconductor.

Thus, the maximum number of charges (N) that can be transported in each acoustic wavelength can be derived by equating the two forces as

$$F_{SAW} = F_E \tag{3.13}$$

$$N = \frac{\varepsilon_{SAW}\lambda^2}{4qk_e} \tag{3.14}$$

It can be seen from equation (3.14) that the maximum charge capacity is greater for higher wavelengths. Now the current for carrying N number of charges by SAW travelling at a time

TH-3353_166102010

period of $T = \frac{1}{f}$ can be written as $I = \frac{Nq}{T}$, where q is the charge of an electron. Substituting equation (12), we get

$$I = \frac{\mathcal{E}_{SAW}\,\lambda^2}{4k_e T} \tag{3.15}$$

Using equation (3.15), the calculated maximum current density value comes out to be 23 nA/cm^2 for a charge transport at -8 dBm RF power and 42 MHz acoustic frequency and the experimental value is 7.5 nA/cm^2 as observed in Figures 3.3(a) and 3.6(a). Similarly, for RF powers -10 dBm and -12 dBm, the calculated values of maximum current density are 18 nA/cm^2 and 11 nA/cm^2, while the experimental values are 5.6 nA/cm^2 and 2.2 nA/cm^2, respectively. The difference between calculated and experimental values of current density can be attributed to the transport loss (~ 30%) due to traps [40]–[42] encountered in the SAW path and charge collection losses (~30–35 %) in the collector diode [43]–[46].

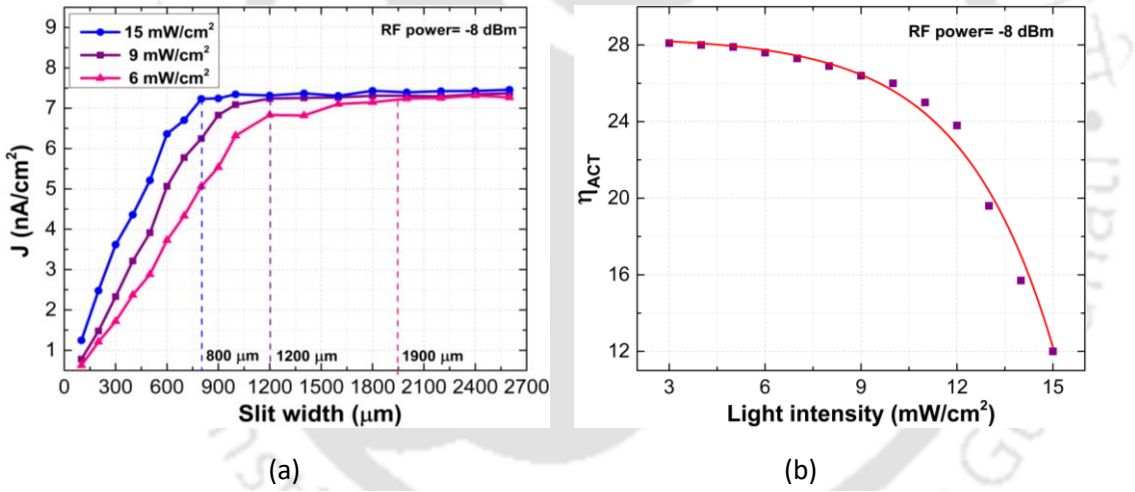

Figure 3.7: (a) Current density for three light intensities as a function of slit size at constant SAW RF power -8 dBm. (b) Theoretically calculated η_{ACT} plotted as a function of light intensities at RF power of -8 dBm.

Figure 3.7(a) shows the effect of the illuminated area on the output current by varying the slit width from 100 μm to 3000 μm. The current density initially increases linearly with an increase in illuminated area and reaches the saturation at 800 μm slit width for the optical power of 15 mW/cm^2. For the light intensity of 9 mW/cm^2 and 6 mW/cm^2, the saturation was observed at slit widths of 1200 μm and 1900 μm, respectively. As the SAW propagates through the illuminated area, it will ionize the excitons generated in its propagation path and accumulate the segregated charges until the maximum capacity is reached, as discussed above. As a consequence, at lower light intensities, the slit width at which saturation occurs further

TH-3353_166102010

increases. Thus, in general, the maximum charge capacity increases with the SAW power and wavelength and is independent of the light intensity. The acoustic charge transfer efficiency [47] (η_{ACT}) for a particular illumination intensity is defined as the ratio of charges transported by SAW at the collector diode (Q_{out}) to the total number of charges optically generated (Q_{gen}) in the polymer film.

$$\eta_{ACT} = \frac{Q_{out}}{Q_{gen}} \times 100 \tag{3.16}$$

For the acoustic wavelength of 80 μm and –8 dBm acoustic power, η_{ACT} values are calculated (details in Appendix A) and plotted against light intensity in Figure 3.7(b). As the light intensity increases, η_{ACT} gradually decreases, attributed to the gradual screening of the SAW field since with the increase in light intensity, more charges accumulate in the potential well. Thus, after the light intensity of 13 mW/cm^2, SAW reaches its maximum charge capacity, resulting in the maximum screening of the SAW field. Moreover, this screening of the SAW field reduces the ionization of further photogenerated excitons. Hence, the decrease in η_{ACT} is significant for higher light intensity values. The same can be verified from the current saturation region beyond 13 mW/cm^2 in Figure 3.6(a). The maximum value of $\eta_{ACT} = 28\%$ is in agreement with the PL quenching intensity value, which has been observed to be equal to 26% and 25% in the presence of SAW with an RF power of -8 dBm in Figure 3.5. The comparison establishes that the SAW-assisted acoustic charge transfer has been observed in both the instantaneous PL and the current measurements.

3.3.4 Effect of RF power

Figure 3.8 describes the plot of the photovoltaic current density as a function of SAW RF power. The threshold behaviour of the curve at -16 dBm of acoustic power accounts for the minimum field requisite for the charge transport. The minimum field required was calculated theoretically from equation (3.9) at -15 dBm, which is close to what has been observed experimentally. Only for power levels greater than -16 dBm charges were confined and transported by SAW. Between the range of -14 to -8 dBm, the SAW could carry a more significant number of carriers for the same optical injection, and an increase in the current is observed.

TH-3353_166102010

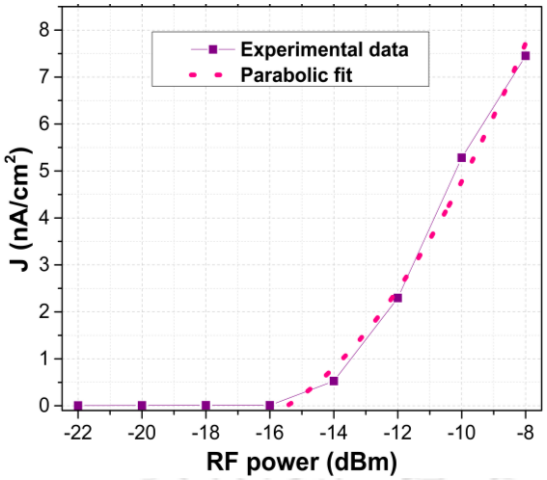

Figure 3.8: Experimental data of photovoltaic current density versus RF power showing parabolic dependency for RF power > -16 dBm.

Accordingly, η_{ACT} also increases with SAW power. A parabolic fit considering equation (3.9) with μ as the variable parameter was done for the current density using Origin 9.0 software. The best fit was estimated for $\mu = 0.7$ cm^2/Vs, which agrees well with reported mobility values for the polymer [32], [33], [48]. With the best fit for μ, the theoretical values for current densities are 7.66, 5.22 and 2.29 nA/cm^2 for the RF values of -8, -10 and -12 dBm respectively. The corresponding experimental values for the current densities are 7.45, 5.28 and 2.19 nA/cm^2, respectively.

3.4 Acousto-electric analysis

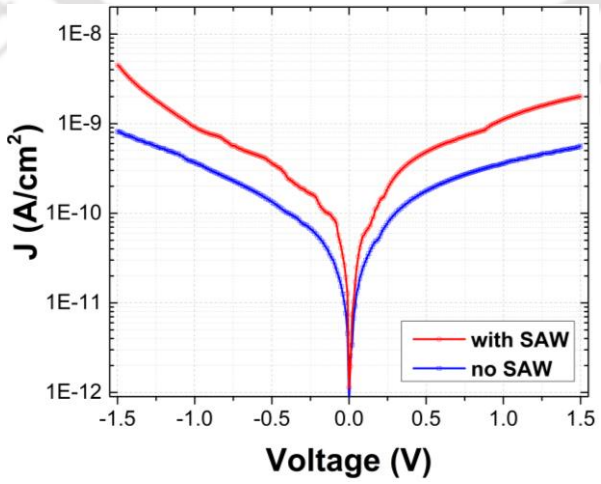

Figure 3.9: Semi-log plot of the current density (J) versus voltage for the collector diode applying a voltage bias with and without SAW.

TH-3353_166102010

The acousto-electric analysis is performed by injecting charge carriers to the collector diode through electrical bias and observing the behaviour of the current in the absence and presence of SAW. Figure 3.9 presents the semi-log *J-V* plot for the acoustic charge transport device applying a voltage bias ranging from -1.5 V to 1.5 V with and without SAW. Acoustic waves produce an electric potential that varies in space and is proportional to acoustic deformation. As a result of the interaction of SAW with the injected charge carriers, the wave's energy and momentum could be transferred to the charge carriers. The charge transport in an organic semiconductor with disordered energy states is primarily controlled by the hopping of charges through localised energy states distributed randomly in space [49]. In the presence of a SAW, the effective energy difference between these states will decrease, while the hopping probability will increase [50]. This decrease in the effective energy attributes to the higher current for charge injection in the presence of SAW, helping the injected charge carriers to overcome any traps/barriers along its path.

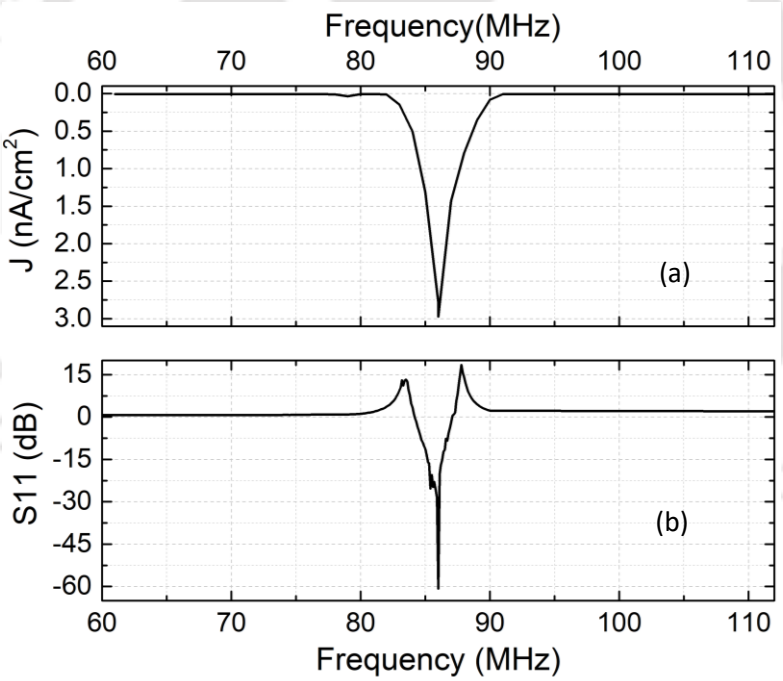

Figure 3.10: Frequency dependence of (a) current density of the fabricated device, and (b) S_{11} power reflection coefficient of the IDT.

The acousto-electric analysis is concluded by measuring the current density of the device and compared to the reflection coefficient for the same spectrum of frequency for which SAW is propagated. The experiments were performed for the fabricated device with IDT of 10 μm dimension. Figure 3.10(a) displays the frequency dependence of the current density obtained for the fabricated device having a dip at the resonance frequency. Figure 3.10(b) shows the RF

TH-3353_166102010

power reflection coefficient S_{11}, which exhibits a dip at the resonance frequency of 86.7 MHz signifying SAW excitation and propagation. It can be established from the plot that at the resonance frequency, maximum power is transferred from the source to the load resulting in the attainment of the maximum peak of current density.

3.5 Summary

In summary, with the assistance of SAW, an ambipolar charge transport of electrons and holes optically generated in organic semiconductors, P3HT and MEH-PPV, has been demonstrated and analysed. The excitons are separated, trapped and moved as spatially separated charge carriers along the SAW path and then collected at the collector diode. The maximum charge capacity is found to be the function of SAW power and wavelength and is independent of light intensity. η_{ACT} gradually decreases with an increase in light intensity because of the screening effect. However, at high intensities, SAW potential well reaching its maximum charge capacity limits the exciton ionization and η_{ACT} drops significantly. In order to realise the acoustic charge transport, the energy of the SAW must be greater than the exciton binding energy. The energy and momentum of the wave are transferred to the charge carriers as a result of the interaction between the SAW and the charge carriers.

TH-3353_166102010

3.6 References

[1] G. Weinreich and H. G. White, "Observation of the acoustoelectric effect," *Phys. Rev.*, vol. 106, no. 1, pp. 1–3, 1957.

[2] R. H. Parmenter, "The acousto-electric effect," *Phys. Rev.*, vol. 89, no. 5, pp. 990–998, 1953.

[3] B. C. Beggs, L. Young, and R. R. Johnson, "Response of an acoustic charge transport device to near-infrared radiation.," *Int. Electron Devices Meet.*, pp. 294–297, 1987, doi: 10.1109/iedm.1987.191413.

[4] G. Weinreich, T. M. Sanders, Jr., and H. G. White, "Acoustoelectric effect in n-type germanium," *Phys. Rev.*, vol. 114, no. 1, pp. 33–44, 1959.

[5] J. Rudolph, R. Hey, and P. V. Santos, "Long-range exciton transport by dynamic strain fields in a GaAs quantum well," *Phys. Rev. Lett.*, vol. 99, no. July, p. 047602, 2007, doi: 10.1103/PhysRevLett.99.047602.

[6] A. Violante, K. Cohen, S. Lazić, R. Hey, R. Rapaport, and P. V. Santos, "Dynamics of indirect exciton transport by moving acoustic fields," *New J. Phys.*, vol. 16, 2014, doi: 10.1088/1367-2630/16/3/033035.

[7] C. Rocke, S. Zimmermann, A. Wixforth, and J. P. Kotthaus, "Acoustically driven storage of light in a quantum well," *Phys. Rev. B*, vol. 57, pp. 4099–4102, 1997.

[8] D. L. Smythe and Ral, "Integrated surface acoustic wave/charge-coupled (SAW/CCD) signal processing devices," *SPIE Opt. Signal Process. C3I*, vol. 209, pp. 152–158, 1979.

[9] K. Tsubouchi, T. Higuchi, M. Nagao, and N. Mikoshiba, "Charge transfer by surface acoustic waves on a monolithic MIS structure," *Appl. Phys. Lett.*, vol. 33, no. 8, pp. 762–765, 1978, doi: 10.1063/1.90496.

[10] A. O. Govorov, A. V. Kalameitsev, V. M. Kovalev, H.-J. Kutschera, and A. Wixforth, "Self-induced acoustic transparency in semiconductor quantum films," *Phys. Rev. Lett.*, vol. 88, no. 22, p. 226803, 2001, doi: 10.1103/PhysRevLett.87.226803.

[11] M. Rotter, A. Wixforth, W. Ruile, D. Bernklau, and H. Riechert, "Giant acoustoelectric effect in GaAs/$LiNbO_3$ hybrids," *Appl. Phys. Lett.*, vol. 73, no. 15, pp. 2128–2130, 1998, doi: 10.1063/1.122400.

[12] M. Koopmans *et al.*, "Electrical conductivity of doped organic semiconductors limited by carrier-carrier interactions," *ACS Appl. Mater. Interfaces*, vol. 12, no. 50, pp. 56222–56230, 2020, doi: 10.1021/acsami.0c15490.

[13] B. A. Weir, E. A. Marseglia, S. M. Chang, and A. B. Holmes, "Changes in structure and morphology in the conjugated polymer MEH-PPV," *Synth. Met.*, vol. 101, no. 1, pp. 154–155, 1999, doi: 10.1016/S0379-6779(98)00560-8.

[14] N. A. N. Ismail, S. Shaari, N. Juhari, N. Sabani, M. F. Ahmad, and N. F. Zakaria, "Temperature effects on electrical and structural properties of MEH-PPV/PEIE OLED device," *J. Phys. Conf. Ser.*, vol. 1535, no. 1, p. 012020, 2020, doi: 10.1088/1742-6596/1535/1/012020.

TH-3353_166102010

[15] H. Dong and W. Hu, “Multilevel investigation of charge transport in conjugated polymers,” *Acc. Chem. Res.*, vol. 49, no. 11, pp. 2433–2435, 2016, doi: 10.1021/acs.accounts.6b00368.

[16] M. J. A. Schuetz, J. Knörzer, G. Giedke, L. M. K. Vandersypen, M. D. Lukin, and J. I. Cirac, “Acoustic traps and lattices for electrons in semiconductors,” *Phys. Rev. X*, vol. 7, no. 4, p. 041019, 2017, doi: 10.1103/PhysRevX.7.041019.

[17] G. Weinreich, “Acoustodynamic effects in semiconductors,” *Phys. Rev.*, vol. 104, no. 2, pp. 321–324, 1956.

[18] G. Weinreich, “Acoustodynamic effects in semiconductors,” *Phys. Rev.*, vol. 104, no. 2, pp. 321–324, 1956.

[19] J. B. Kinzel *et al.*, “Directional and dynamic modulation of the optical emission of an individual GaAs nanowire using surface acoustic waves,” *Nano Lett.*, vol. 11, no. 4, pp. 1512–1517, 2011, doi: 10.1021/nl1042775.

[20] F. Grasselli, A. Bertoni, and G. Goldoni, “Classical and quantum dynamics of indirect excitons driven by surface acoustic waves,” *Phys. Rev. B*, vol. 98, no. 16, p. 165407, 2018, doi: 10.1103/PhysRevB.98.165407.

[21] F. Alsina, J. A. H. Stotz, R. Hey, and P. V. Santos, “Acoustically induced potential dots in GaAs quantum wells,” *Solid State Commun.*, vol. 129, pp. 453–457, 2003, doi: 10.1016/j.ssc.2003.11.014.

[22] P. V. Santos, F. Alsina, J. A. H. Stotz, R. Hey, S. Eshlaghi, and A. D. Wieck, “Band mixing and ambipolar transport by surface acoustic waves in GaAs quantum wells,” *Phys. Rev. B - Condens. Matter Mater. Phys.*, vol. 69, no. 15, pp. 1–11, 2004, doi: 10.1103/PhysRevB.69.155318.

[23] D. Leibfried, R. Blatt, C. Monroe, and D. Wineland, “Quantum dynamics of single trapped ions,” *Rev. Mod. Phys.*, vol. 75, pp. 281–324, 2003, doi: 10.1103/RevModPhys.75.281.

[24] W. Paul, “Electromagnetic traps for charged and neutral particles (nobel lecture),” *Angew. Chemie Int. Ed. English*, vol. 29, no. 7, pp. 739–748, 1990, doi: 10.1002/anie.199007391.

[25] S. Rahav, I. Gilary, and S. Fishman, “Time independent description of rapidly oscillating potentials,” *Phys. Rev. Lett.*, vol. 91, no. 11, pp. 110404–1, 2003, doi: 10.1103/PhysRevLett.91.110404.

[26] S. Rahav, I. Gilary, and S. Fishman, “Effective Hamiltonians for periodically driven systems,” *Phys. Rev. A*, vol. 68, no. 1, p. 013820, 2003, doi: 10.1103/PhysRevA.68.013820.

[27] P. V. Santos, T. Schumann, M. H. Oliveira, J. M. J. Lopes, and H. Riechert, “Acousto-electric transport in epitaxial monolayer graphene on SiC,” *Appl. Phys. Lett.*, vol. 102, no. 22, p. 221907, 2013, doi: 10.1063/1.4809726.

[28] M. J. Hoskins and B. J. Hunsinger, “Simple theory of buried channel acoustic charge transport in GaAs,” *J. Appl. Phys.*, vol. 55, no. 2, pp. 413–426, 1984, doi: 10.1063/1.333089.

TH-3353_166102010

[29] P. V. Santos, M. Ramsteiner, and F. Jungnickel, "Spatially resolved photoluminescence in GaAs surface acoustic wave structures," *Appl. Phys. Lett.*, vol. 72, no. 17, pp. 2099–2101, 1998, doi: 10.1063/1.121288.

[30] L. J. F. Broer, "On the propagation of energy in linear conservative waves," *Appl. Sci. Res.*, vol. A2, pp. 329–343, 1951.

[31] J. E. Northrup, "Atomic and electronic structure of polymer organic semiconductors : P3HT , PQT , and PBTTT," *Phys. Rev.*, vol. 76, pp. 245202-1–6, 2007, doi: 10.1103/PhysRevB.76.245202.

[32] H. C. Avila *et al.*, "High hole-mobility of rrP3HT in organic field-effect transistors using low-polarity polyurethane gate dielectric," *Org. Electron.*, vol. 58, pp. 33–37, 2018, doi: 10.1016/j.orgel.2018.03.033.

[33] K. J. Baeg *et al.*, "High mobility top-gated poly(3-hexylthiophene) field-effect transistors with high work-function Pt electrodes," *Thin Solid Films*, vol. 518, no. 14, pp. 4024–4029, 2010, doi: 10.1016/j.tsf.2010.01.026.

[34] J. P. Wolfe and A. Mysyrowicz, "Excitonic matter," *Sci. Am.*, vol. 250, no. 3, pp. 98–107, 1984.

[35] T. Wang *et al.*, "Tuning electron-hole distance of the excitons in organic molecules using functional groups," *Chem. Phys. Lett.*, vol. 618, pp. 142–146, 2015, doi: 10.1016/j.cplett.2014.10.072.

[36] C. Deibel *et al.*, "Energetics of excited states in the conjugated polymer Poly(3-hexylthiophene)," *Phys. Rev. B*, vol. 81, p. 085202, 2010.

[37] A. Dkhissi, "Excitons in organic semiconductors," *Synth. Met.*, vol. 161, no. 13–14, pp. 1441–1443, 2011, doi: 10.1016/j.synthmet.2011.04.003.

[38] S. F. Alvarado, P. F. Seidler, D. G. Lidzey, and D. D. C. Bradley, "Direct determination of the exciton binding energy of conjugated polymers using a scanning tunneling microscope," *Phys. Rev. Lett.*, vol. 81, no. 5, pp. 1082–1085, 1998, doi: 10.1103/PhysRevLett.81.1082.

[39] D. Moses, J. Wang, A. J. Heeger, N. Kirova, and S. Brazovski, "Exciton binding energy in poly(phenylene vinylene)," *Synth. Met.*, vol. 125, no. 1, pp. 93–98, 2001, doi: 10.1016/S0379-6779(01)00515-X.

[40] F. Alsina, J. A. H. Stotz, R. Hey, and P. V. Santos, "Radiative recombination during acoustically induced transport in GaAs quantum wells," *J. Vac. Sci. Technol. B Microelectron. Nanom. Struct.*, vol. 24, no. 4, p. 2029, 2006, doi: 10.1116/1.2214715.

[41] S. K. Zhang, P. V. Santos, and R. Hey, "Radiative recombination during ambipolar carrier transport by surface acoustic waves in GaAs quantum wells," *Appl. Phys. Lett.*, vol. 80, no. 13, pp. 2320–2322, 2002, doi: 10.1063/1.1463706.

[42] C. Rocke, S. Zimmermann, A. Wixforth, J. P. Kotthaus, G. Böhm, and G. Weimann, "Acoustically driven storage of light in a quantum well," *Phys. Rev. Lett.*, vol. 78, no. 21, pp. 4099–4102, 1997, doi: 10.1103/PhysRevLett.78.4099.

[43] T.-H. Lai, S.-W. Tsang, J. R. Manders, S. Chen, and F. So, "Properties of interlayer for

TH-3353_166102010

organic photovoltaics," *Mater. Today*, vol. 16, no. 11, pp. 424–432, 2013, doi: 10.1016/j.mattod.2013.10.001.

[44] J. Guo *et al.*, "Easy-processing saccharin doped ZnO electron extraction layer in efficient polymer solar cells," *Sol. Energy*, vol. 220,pp. 706–712, 2021, doi: 10.1016/j.solener.2021.03.083.

[45] R. Jansen-van Vuuren, A. Armin, A. Pandey, P. Burn, and P. Meredith, "Organic photodiodes: The future of full color detection and image sensing," *Adv. Mater.*, vol. 28, pp. 4766–4802, 2016, [Online]. Available: https://onlinelibrary.wiley.com/doi/epdf/10.1002/adma.201505405.

[46] M. Cheng *et al.*, "Charge-transport layer engineering in perovskite solar cells," *Sci. Bull.*, vol. 65, no. 15, pp. 1237–1241, 2020, doi: 10.1016/j.scib.2020.04.021.

[47] B. C. Beggs, L. Young, and R. R. Johnson, "Optical charge injection into a gallium arsenide acoustic charge transport device," *J. Appl. Phys.*, vol. 63, no. 7, pp. 2425–2430, 1988, doi: 10.1063/1.341037.

[48] J. E. Northrup, "Atomic and electronic structure of polymer organic semiconductors: P3HT, PQT, and PBTTT," *Phys. Rev. B - Condens. Matter Mater. Phys.*, vol. 76, no. 24, pp. 1–6, 2007, doi: 10.1103/PhysRevB.76.245202.

[49] A. V. Nenashev, F. Jansson, S. D. Baranovskii, R. Österbacka, A. V. Dvurechenskii, and F. Gebhard, "Effect of electric field on diffusion in disordered materials. I. One-dimensional hopping transport," *Phys. Rev. B - Condens. Matter Mater. Phys.*, vol. 81, no. 11, 2010, doi: 10.1103/PhysRevB.81.115203.

[50] P. Bhattacharjee, H. Mishra, P. K. Iyer, and H. B. Nemade, "Acoustically assisted charge transport in Poly(3-hexylthiophene)," *ACS Appl. Electron. Mater.*, vol. 4, no. 7, 2022, doi: 10.1021/acsaelm.2c00524.

TH-3353_166102010

Chapter 4

Acoustical Control of Charge Movement in an Organic Semiconductor

In optical fibre technology, data encryption in the form of light pulses is considered an efficient way to transmit signals over large distances. This technology involves efficient systems for encoding, decoding and transporting light pulses. Pure optical processing techniques are limited owing to the weak interaction of the photon beams and thus are primarily performed electronically. An emerging approach to information processing is the conversion of photons into charge carriers, controlling and routing the carriers, directing to their successful extraction or recombination. Photon–exciton conversion systems typically involve eminent charge-coupled and CMOS devices but possess complex circuitry. Acoustic waves generally generated in a piezoelectric material have been receiving attention for their contribution to charge carrier transport [1]–[3]. ACT over a few micrometres has been well established in inorganic semiconductors using SAW beams [4]–[6]. The first acoustic charge transfer device generating optically excited excitons using infrared radiation of 730 nm wavelength and transporting the separated charge carriers was demonstrated experimentally in 1987 by Beggs et al. [7] The spatial separation [8], [9] and dragging of photogenerated charge carriers using SAW [10], [11] in a semiconductor lattice creates a prospect for easy charge carrier transport. The moving SAW potential transported the charge carriers in the semiconductor lattice as a conveyor belt [12] of carriers validated by the photoluminescence measurements [13], [14]. ACT in organic semiconductors such as P3HT and MEH-PPV has been observed and explained in the previous chapter. Despite the predominance of transistor-based charge transport devices, acoustically induced charge transport using contactless acoustic beams can be seen as the new

TH-3353_166102010

state-of-art in solid-state information processing. A distinctive charge-controlling behaviour has also been reported by a few researchers utilising two or more SAW beams. Alsina et al. [15] investigated the formation of dynamic dots in a semiconductor quantum well structure by designing two IDTs orthogonal to each other. Lima et al. [16] explored the possibility of manipulating and controlling the charges in a semiconductor substrate through the interaction of two SAW beams. They showed the alteration in charge carriers in a GaAs based quantum well structure by establishing a basic control RF switch. Sogawa et al. [17] studied the dynamic optical characteristics of excitons in dynamic quantum dots formed in GaAs by the interference of orthogonally propagating SAW beams. It will be interesting to examine how the integration of SAW with the charge carriers in an organic semiconductor can acoustically control and manipulate the charge carrier transport.

In this chapter, an experimental demonstration of the unidirectional ACT in an organic semiconductor by two parallel and counter-opposite SAWs has been presented utilizing an easy and straightforward structure consisting of two identical IDTs and a corresponding collector diode facing each IDT. The effect of SAW drag force on the charge carriers by interacting two SAWs has been studied using an orthogonal layout of the two IDTs. The Keysight PNA-L Network Analyzer cascaded with MPS 150 RF probe station fed continuous RF signals matched to IDT1 and IDT2 resonance frequencies, resulting in SAW1 and SAW2 acoustic waves. The acoustical control of the charge movement is characterised and analysed using the Keithley 4200A-SCS Parameter Analyzer.

4.1 Device fabrication

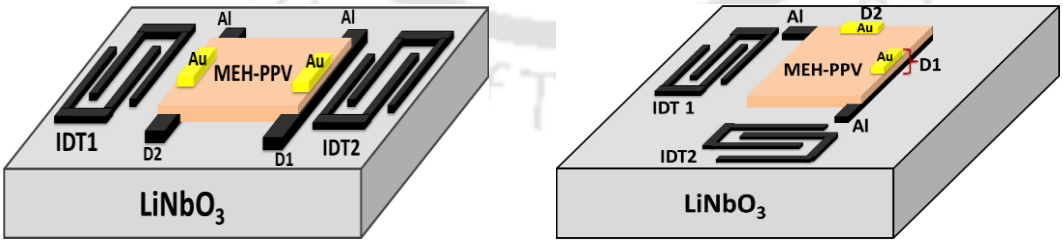

Figure 4.1: (a) Device structure with two IDTs which transmit SAWs in opposite directions and corresponding collector diodes D1 and D2 to collect the charges transported by each SAW. (b) Device structure with two IDTs to transmit SAWs in orthogonal directions and two corresponding collector diodes D1 and D2 opposite to the IDTs.

TH-3353_166102010

The work requires the fabrication of mainly two kinds of device structures on YZ lithium niobate substrates. Each device structure comprises two IDTs (IDT1 and IDT2), a polymer layer, and two collector diodes (D1 and D2). An MSM configuration with the semiconducting polymer layer forms the collector diodes. The first device structure has two IDTs that transmit SAWs in opposite directions and two collector diodes, one each at the edges of the polymer, to collect the charges transported by each SAW, as shown in Figure 4.1(a). The second device structure is similar except that the positioning of two IDTs is in perpendicular orientation to generate SAWs in orthogonal directions, as depicted in Figure 4.1(b). The layout of the device structure is graphically designed using CleWin software and used to make a hard photomask by direct laser writing (using Dilase 250-Kloe direct laser writing instrument) on the soda-lime glass coated with AZ 1518 photoresist. The IDTs, each of 20 finger pairs (N_P), are designed with three different finger widths and spacings ($\lambda/4$) of 10, 15, and 20 μm and corresponding aperture widths (W_a) of 1.9, 2.92, and 3.89 mm. Aperture width, *Wa*, calculated from aperture optimisation, offers 50 Ω impedance for RF port matching. The theoretically calculated values of the resonance frequencies corresponding to the IDT finger widths 10, 15, and 20 μm are 87.2, 58.1, and 43.6 MHz, respectively.

4.2 Unidirectional acoustic charge transport

An excitation to IDT1 and IDT2 will generate rayleigh waves (SAW1 and SAW2) that travel oppositely in the *x* direction. Figure 4.2(a) presents the input reflection coefficients, S_{11} and S_{22}, of Rayleigh SAW with the resonance peak obtained experimentally at 42.7 MHz. The white light was shone on the polymer film in the space between the two collector diodes to optically generate excitons in the path of SAW propagation. When SAW propagates through the polymer, the induced SAW fields ionize the excitons, segregate the electrons to the crests and holes to the troughs and transport the charges in the direction of SAW propagation [18]. SAW1 travelling from IDT1 would trap the charge carriers along its path and transport them to the diode D1. As anticipated, D1 showed a large current, and D2 showed negligible current when IDT 1 was on. Similarly, SAW2 travelling from IDT2 would move the generated charges to the diode D2 resulting in a high current from D2 and a negligible current from D1, as observed in Figure 4.2(d). SAW is unidirectional, therefore it drags the photogenerated charges that are formed in the polymer along its route in the direction of its propagation. Thus, this experiment offers a simple technique to verify the unidirectional charge transport of excitons photogenerated in a semiconducting polymer film with the help of SAW-induced fields.

TH-3353_166102010

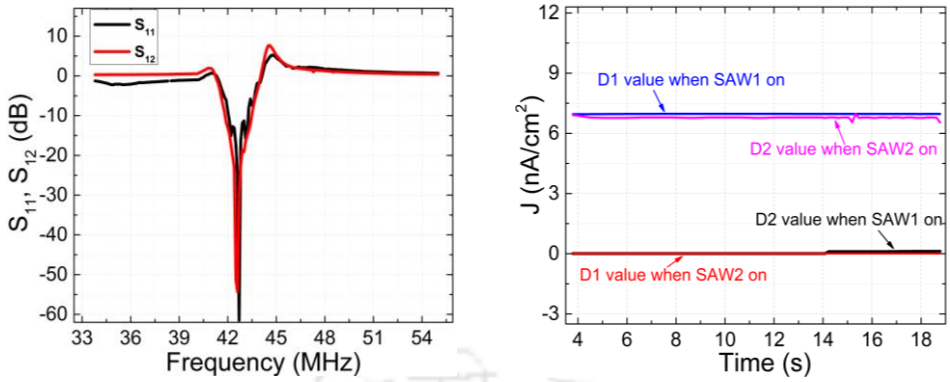

Figure 4.2: (a) S_{11}, S_{22} (dB) of the Rayleigh SAW obtained experimentally for 20 µm IDT finger width. (b) Time response of current density for the fabricated device with parallel IDTs and diodes arrangement.

4.3 Interaction of orthogonal SAWs

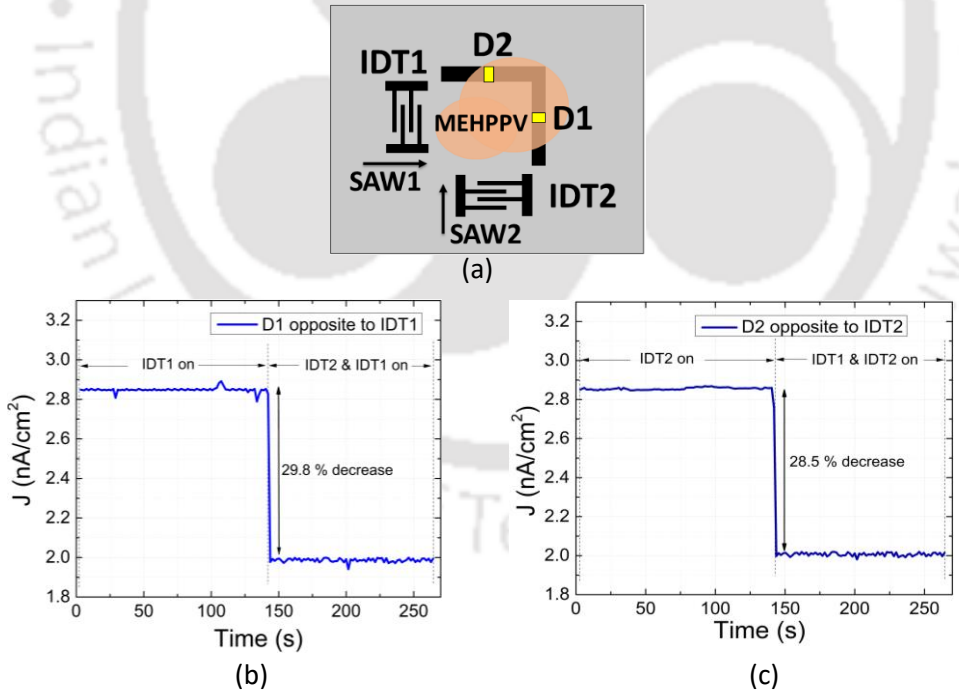

Figure 4.3: (a) 2D schematic of the fabricated orthogonal device. (b) Current density at diode D1 when first IDT1 is activated and then IDT2 activated. (c) Current density at diode D2 when first IDT2 is activated and then IDT1 activated.

The previous experiment reveals that the charge carriers experience an acoustic drag force by the acoustic wave in the direction of SAW propagation. Similarly, two SAWs propagating

TH-3353_166102010

in orthogonal directions provide an opportunity to explore and manipulate the transfer of charge carriers in the polymer plane. It can be realized with two IDTs constructed in perpendicular orientation and a collector diode facing each IDT, as shown in the 2D schematic of the device structure in Figure 4.3(a). We investigated the interaction of orthogonal SAWs (SAW1 and SAW2) on the charge carriers photogenerated in MEH-PPV under a light intensity of 15 mW/cm^2 by using identical IDTs (IDT1 and IDT2) of finger width 10 µm each excited with RF power of -8 dBm. Figure 4.3(b) shows that when just IDT1 is excited, the photogenerated excitons in the acoustic path of SAW1 are ionized and delivered to the corresponding collector diode, D1, producing a current density of 2.8 nA/cm^2. After an interval of around 140 s when IDT2 is stimulated, the current density at D1 decreases to 2.0 nA/cm^2, showing a percentage decrease by 29.8%. When IDT1 is excited, excitons generated in MEH-PPV by optical illumination are ionized and dragged by SAW1 to the collector diode D1. After IDT2 is triggered, charge carriers moving along with SAW1 are confronted by the acoustic drag force of SAW2, and some of the charge carriers are dragged away from the SAW1 path, as seen by the decrease in the current of D1. The charge carriers under the influence of SAW2 are conveyed to the respective collector diode, D2, giving a current density of 2.9 $nA/cm^{2,}$ as shown in Figure 4.3(c). However, when SAW1 is turned on after an interval of 140 s, there is a decrease in the current by 28.6%. Hence, charge carriers transported by SAW1 are hindered by SAW2, resulting in the acoustic manipulation of the charge carriers. The percentage decrease is 28–30% for the same dimension IDTs.

4.3.1 Interaction of orthogonal SAWs with different SAW frequencies

The implication of the different dimension IDTs in the orthogonal arrangement constructs a prospect to alter the percentage reduction of charges. The experiment is then repeated using IDTs with different finger widths of 15 µm in IDT1 generating SAW1 of 56 MHz, and 10 µm in IDT2 producing SAW2 of 85 MHz, and following the same sequence of operation, turning on SAW1 first, followed by turning on SAW2 and measuring the current at D1. Since the frequency of SAW2 is greater than the frequency of SAW1, the combination is referred to as a low-high (L-H) frequency case representing the influence of higher frequency (HF) SAW on the charge transport by lower frequency (LF) SAW. Similarly, turning on SAW2 while measuring the current at D2, followed by SAW1, can be referred to as a high-low (H-L) frequency case since it represents the influence of LF SAW on charge transport by HF SAW. The charge can be quantified as the average value of the current measured multiplied by the time of measurement ($Q = I_{avg} \times t$). Figure 4.4(a) represents the decrease (in the form of a bar graph) in the amount of charges transferred to diode D1 measured with IDT1 on and with both

TH-3353_166102010

IDT1 and IDT2 on. Similarly, Figure 4.4 (b) shows the amount of charge transferred to diode D2 measured with IDT2 on and with both IDT2 and IDT1 on. It can be observed that the decrease in charge for D1 is more as compared to D2 when both the IDTs are turned on and can be explained as follows.

The charge manoeuvring behaviour of the orthogonal SAWs of different frequencies can be explained by the acoustic radiation force or acoustic drag force, which is a function of SAW frequency. Wave motion in all of its forms, electromagnetic waves, transverse surface waves, or longitudinal sound waves, imposes a unidirectional radiation force [19], [20] on the obstacles in the path. In semiconductor physics, the acoustic drag force can be explained through the charge carrier motion by the wave [21]. The acoustic wave causes a spatially variable electrostatic potential proportional to the acoustic deformation. The charges tend to attain a lower energy state, creating an equilibrium distribution. As the SAW propagates, the charges must take some time to attain equilibrium and lag behind the wave experiencing a drag in the direction of SAW propagation.

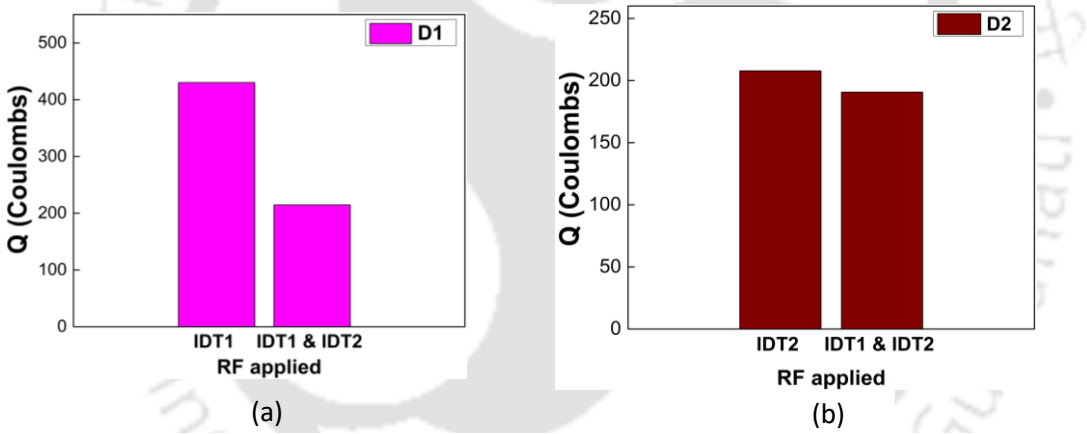

Figure 4.4: (a) Bar diagram showing the decrease in charge received at diode D1, and (b) diode D2 when both the SAW beams are interacted.

4.3.2 Acoustic drag force

The acoustic drag on the charge carriers consumes the energy of the surface waves, which is accompanied by the loss of wave momentum [22]–[24]. This loss of momentum is described by Weinreich [25] as an average force exerted on the charge carriers and is represented as

$$F = \frac{q^2 S}{c^2 KT} \frac{\omega^2 \tau_R}{[1+(\omega\tau_R)^2]} \tag{4.1}$$

TH-3353_166102010

where q, S , τ_R and ω are the acoustic charge, acoustic power, intervalley scattering time, and frequency, respectively.

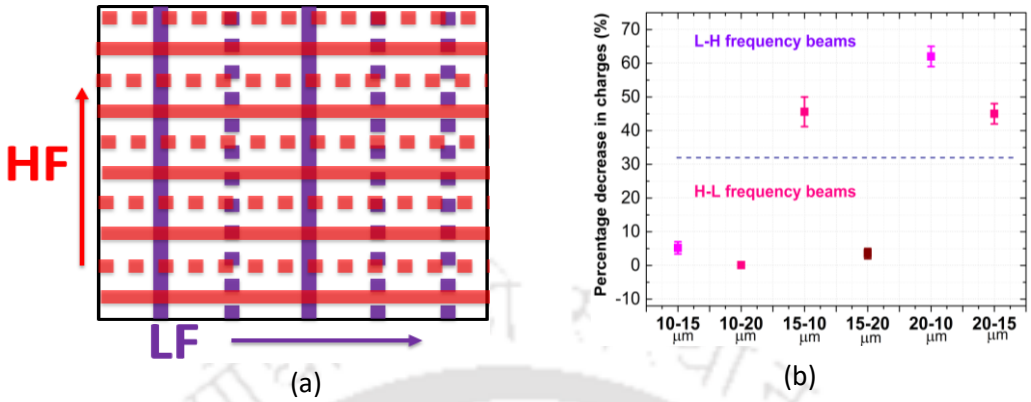

Figure 4.5: (a) Visual representation of the effect of the interaction of H-F SAW beam with L-F SAW beam and vice-versa. (b) Percentage decrease in charges for the six combinations of H-F and L-F SAW beams.

It can be observed from equation (4.1) that the acoustoelectric dragging force is an increasing function of frequency. As a result, the acoustic drag exerted on the charge carriers by HF outweighs the LF drag. In the L-H frequency case, the visual representation of the region of interaction is shown in Figure 4.5(a), depicting the LF wavefront with crests as blue lines and troughs as dashed blue lines and, similarly, the HF wavefront in red colour. As a result of the interaction of the two waves, the charges tend to accumulate at the intersections of the two wavefronts and are influenced by the drag forces of the two waves. Since the HF drag is greater than the LF drag, a greater number of charge carriers will be drifted away from the path of the LF SAW beam, and as a consequence, the number of charges transferred to diode D1 decreases. Comparatively, for the H-L frequency case, LF having a lower drag on the carriers pulls away a smaller number of charge carriers from the HF, causing a slight decrease in the diode D2 current. Consequently, the orthogonal IDTs system can be viewed as an RF button switch to control the number of charges transported to a desired location. The experiment was repeated for several combinations of HF and LF SAW beams, as mentioned in Table 1, and the percentage reduction in charges in each case was noted. Figure 4.5(b) represents the percentage reduction in charges for the six combinations of frequencies. It can be observed that for L-H frequency cases, the percentage reduction in charges is in the range of 40–65%, whereas for H-L frequency cases, the percentage reduction in charges is minimal in the range of 1–7%. The more the difference in the two frequencies interacting, the more significant is the percentage decrease in charge.

TH-3353_166102010

Table 4.1: Combinations of SAW frequencies and the percentage reduction in charges

Layout name	IDTs paired	SAW frequencies interacting	Percentage decreases in charges
L-H frequency	15–10 µm 20–15 µm 20–10 µm	56–85 MHz 43–56 MHz 43–85 MHz	50% 45% 65%
H-L frequency	10–15 µm 10–20 µm 15–20 µm	85–56 MHz 85–43 MHz 56–43 MHz	7% 0.8% 5%

4.4 Diagonal charge transport with orthogonal SAW beams

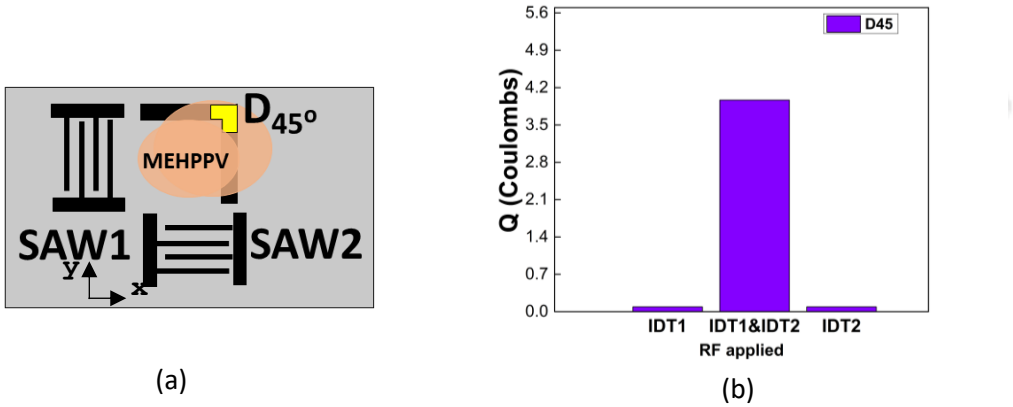

(a) (b)

Figure 4.6: (a) 2D Schematic of the fabricated SAW device to study the charge transport by two orthogonal SAWs of equal frequency, (b) Charge carriers collected at diode D_{45° under three cases: only IDT1 is activated, only IDT2 is activated, and both IDT1 and IDT2 are activated.

As observed in the previous experiment of the interaction of charges with orthogonal SAWs, each wave drags the charges in the direction of propagation independently. In order to verify the direction of the effective transport, we have fabricated a device consisting of two identical IDTs placed orthogonally and a collector diode (D_{45°) placed at an angle of 45° with the directions of wave propagation as shown in Figure 4.6(a). We fabricated several devices with identical IDTs of finger widths 10 µm, 15 µm, or 20 µm producing orthogonal SAWs of frequencies 85 MHz, 56 MHz, or 43 MHz, respectively. Figure 4.6(b) shows the charges collected at diode D_{45° under three cases: only IDT1 is activated, only IDT2 is activated, and both IDT1 and IDT2 are simultaneously activated. It has been observed that the diode D_{45° shows a nominal current for the cases when only IDT1 or IDT2 is turned on and a considerable current when both IDTs are activated at the same time. Suppose we consider the SAW dragging force in the x and y directions as two vectors (S_x and S_y) of equal magnitude (S) interfering at

TH-3353_166102010

right angles to each other. The resultant of the vector will be simply $\sqrt{2}\,S$ of magnitude and making an angle of $tan^{-1}\left(\frac{S_x}{S_y}\right) = 45^{O}$. When RF is applied simultaneously to both the orthogonal IDTs, the resultant SAW drag field leads diagonally. However, for the case RF is applied to either IDT1 or IDT2, only one SAW drag field is present, propagating in either *x* or *y* direction. Therefore, the charges collected at the D_{45^o} diode are negligible. Similar behaviour of diagonal directional charge transport in GaAs [10], (InGa)As [11], and semiconductor quantum wires [27] has been reported using orthogonal SAWs.

4.5 Summary

In this chapter, the unidirectional nature of the ACT in MEH-PPV film formed on a lithium niobate substrate is proved using a simple structure comprising two identical IDTs transmitting SAWs in opposite directions and a corresponding collector diode facing each IDT to collect the charges transported by the SAW. The SAW-induced field causes ACT, which pulls the charge carriers in the direction of propagation. The SAW drag force has also been analysed using a device consisting of two IDTs generating orthogonal SAW beams. It has been analysed that the acoustic drag force is a frequency-dependent term and thus can be used as a parameter in acoustic manipulation of charge carrier transport, observed with the combinations of three frequencies. The orthogonal IDTs arrangement can be used to study the influence of HF wave on the charge transport by LF wave and vice versa. The orthogonal interaction of same-frequency SAWs results in the formation of a resultant drag force that acts diagonally and thus offers charge transport in the organic semiconductor at an angle of 45^{O}. The techniques outlined in this chapter could provide the foundation for optical signal processing devices based on SAW control of excitons in organic semiconductors.

TH-3353_166102010

4.6 References

[1] P. V. Santos, T. Schumann, M. H. Oliveira, J. M. J. Lopes, and H. Riechert, "Acousto-electric transport in epitaxial monolayer graphene on SiC," *Appl. Phys. Lett.*, vol. 102, no. 22, p. 221907, 2013, doi: 10.1063/1.4809726.

[2] P. V. Santos, F. Alsina, J. A. H. Stotz, and R. Hey, "Band mixing and ambipolar transport by surface acoustic waves in GaAs quantum wells," *Phys. Rev. B*, vol. 69, p. 155318, 2004, doi: 10.1103/PhysRevB.69.155318.

[3] A. R. Rezk *et al.*, "Acoustically-driven trion and exciton modulation in piezoelectric two-dimensional MoS_2," *Nano Lett.*, vol. 16, no. 2, pp. 849–855, 2016, doi: 10.1021/acs.nanolett.5b02826.

[4] K. Tsubouchi, T. Higuchi, M. Nagao, and N. Mikoshiba, "Charge transfer by surface acoustic waves on a monolithic MIS structure," *Appl. Phys. Lett.*, vol. 762, 1978, doi: 10.1063/1.90496.

[5] W. D. Hunt, Y. Kim, and F. M. Fliegel, "A synopsis of surface acoustic wave propagation on {100}- cut 〈110〉 propagating gallium arsenide," *J. Appl. Phys.*, vol. 69, no. 4, pp. 1936–1941, 1991, doi: 10.1063/1.348765.

[6] L. Bandhu, L. M. Lawton, and G. R. Nash, "Macroscopic acoustoelectric charge transport in graphene," *Appl. Phys. Lett.*, vol. 103, no. 13, 2013, doi: 10.1063/1.4822121.

[7] B. C. Beggs, L. Young, and R. R. Johnson, "Response of an acoustic charge transport device to near-infrared radiation.," *Int. Electron Devices Meet.*, pp. 294–297, 1987, doi: 10.1109/iedm.1987.191413.

[8] C. Rocke, S. Zimmermann, A. Wixforth, and J. P. Kotthaus, "Acoustically driven storage of light in a quantum well," *Phys. Rev. B*, vol. 57, pp. 4099–4102, 1997.

[9] A. D. Barros, P. D. Batista, A. Tahraoui, J. A. Diniz, and P. V Santos, "Ambipolar acoustic transport in silicon," *J. Appl. Phys.*, vol. 112, no. 1, 2012, doi: 10.1063/1.4733966.

[10] B. C. Schmukler, "Dynamics of charge storage in acoustic charge transport devices on GaAs," *J. Appl. Phys.*, vol. 69, no. 5, pp. 3335–3344, 1991, doi: 10.1063/1.348562.

[11] F. L. Augustine, R. J. Schwartz, and R. L. Gunshor, "Experimental observation of charge transfer by surface acoustic waves in a monolithic Metal/ZnO/SiO_2/Si (MZOS) device," *Ultrason. Symp.*, pp. 769–773, 1981.

[12] M. Rotter, A. V Kalameitsev, A. O. Govorov, W. Ruile, and A. Wixforth, "Charge conveyance and nonlinear acoustoelectric phenomena for intense surface acoustic waves on a semiconductor quantum well," *Phys. Rev. Lett.*, vol. 82, pp. 2171–2174, 1999.

[13] J. Rudolph, R. Hey, and P. V. Santos, "Long-range exciton transport by dynamic strain fields in a GaAs quantum well," *Phys. Rev. Lett.*, vol. 99, no. 4, pp. 1–4, 2007, doi: 10.1103/PhysRevLett.99.047602.

TH-3353_166102010

[14] P. V. Santos, M. Ramsteiner, and F. Jungnickel, "Spatially resolved photoluminescence in GaAs surface acoustic wave structures," *Appl. Phys. Lett.*, vol. 72, no. 17, pp. 2099–2101, 1998, doi: 10.1063/1.121288.

[15] F. Alsina, J. A. H. Stotz, R. Hey, and P. V. Santos, "Acoustically induced potential dots in GaAs quantum wells," *Solid State Commun.*, vol. 129, no. 7, pp. 453–457, 2004, doi: 10.1016/j.ssc.2003.11.014.

[16] M. M. De Lima, R. Hey, J. A. H. Stotz, and P. V. Santos, "Acoustic manipulation of electron-hole pairs in GaAs at room temperature," *Appl. Phys. Lett.*, vol. 84, no. 14, pp. 2569–2571, 2004, doi: 10.1063/1.1695636.

[17] T. Sogawa, H. Sanada, H. Gotoh, H. Yamaguchi, S. Miyashita, and P. V. Santos, "Spatial and temporal modulation of exciton photoluminescence properties in GaAs/AlAs dynamic quantum dots formed by surface acoustic waves," *Phys. Rev. B - Condens. Matter Mater. Phys.*, vol. 80, no. 7, pp. 1–8, 2009, doi: 10.1103/PhysRevB.80.075304.

[18] H. Mishra, P. Bhattacharjee, and H. B. Nemade, "Acoustic charge transport in organic semiconductor films," *J. Phys. D. Appl. Phys.*, vol. 55, no. 1, p. 015102, 2022, doi: https://doi.org/10.1088/1361-6463/ac9f20.

[19] M. L. Palmeri, A. C. Sharma, R. R. Bouchard, R. W. Nightingale, and K. R. Nightingale, "A finite-element method model of soft tissue response to impulsive acoustic radiation force," *IEEE Trans. Ultrason. Ferroelectr. Freq. Control*, vol. 52, no. 10, pp. 1699–1712, 2005, doi: 10.1109/TUFFC.2005.1561624.

[20] G. R. Torr, "The acoustic radiation force," *Am. J. Phys.*, vol. 52, no. 5, pp. 402–408, 1984, doi: 10.1119/1.13625.

[21] R. H. Parmenter, "The acousto-electric effect," *Phys. Rev.*, vol. 89, no. 5, pp. 990–998, 1953.

[22] G. Weinreich, "Ultrasonic attenuation by free carriers in germanium," *Phys. Rev.*, vol. 107, pp. 1–2, 1957.

[23] L. Bandhu, L. M. Lawton, and G. R. Nash, "Macroscopic acoustoelectric charge transport in graphene," *Appl. Phys. Lett.*, vol. 103, no. 13, 2013, doi: 10.1063/1.4822121.

[24] C. C. Tang, Y. F. Chen, D. C. Ling, C. C. Chi, and J. C. Chen, "Ultra-low acoustoelectric attenuation in graphene," *J. Appl. Phys.*, vol. 121, no. 12, 2017, doi: 10.1063/1.4979207.

[25] G. Weinreich, T. M. Sanders, and H. G. White, "Acoustoelectric effect in n-type germanium," *Phys. Rev.*, vol. 114, no. 1, pp. 33–44, 1959, doi: 10.1103/PhysRev.114.33.

[26] M. M. De Lima and P. V. Santos, "Modulation of photonic structures by surface acoustic waves," *Reports Prog. Phys.*, vol. 68, no. 7, pp. 1639–1701, 2005, doi: 10.1088/0034-4885/68/7/R02.

[27] A. O. Govorov, A. V. Kalameitsev, V. M. Kovalev, H.-J. Kutschera, and A. Wixforth, "Self-induced acoustic transparency in semiconductor quantum films," *Phys. Rev. Lett.*, vol. 88, no. 22, p. 226803, 2001, doi: 10.1103/PhysRevLett.87.226803.

TH-3353_166102010

Chapter 5

Electric-Field Induced Chain Alignment in MEH-PPV

In the recent past conjugated polymers have attracted researchers owing to their versatile nature and broad potential applications. Conjugated polymers are organic materials with a backbone chain of alternating double and single bonds. Their overlapping p-orbitals provide a system of delocalized π-electrons, which can lead to fascinating and compelling optical and electrical features. The low-cost production, simple solution processing, light-weight and flexible properties of conjugate polymers make them attractive for organic electronic devices such as solar cells [1]–[3], field effect transistors (FETs) [4]–[6] and flexible electronic devices [7], [8]. Numerous studies have shown that the properties of the organic active layer, which serves as the fundamental building block for all organic optoelectronic devices, significantly influence the charge transport properties and overall device performance. It has been discovered that charge-carrier mobility and overall device characteristics are strongly influenced by the size, shape, crystallinity and chain orientation of the conjugated polymers [9], [10]. The performance of conjugated polymers in electronic devices still falls far behind that of their inorganic counterparts. Inorganic semiconductors have delocalized band structures and electronic states as a result of long-range crystallinity within the atomic lattice. However, the conformation of the polymer backbone governs the potential of conjugated electronic states to delocalize along the backbone at the single molecular level.

Consequently, the conformation of the polymer backbone substantially controls the charge transport and optoelectronic properties of conjugated polymers. Given the anisotropy of polymer chains, the orientation of macromolecular chains significantly affects the overall characteristics of the polymer film. Polymer chain alignment has gained importance as a new

TH-3353_166102010

and effective way to counter grain boundary limitations and increase crystallinity [11], [12] in conjugated polymers. The alignment of semiconducting polymer chains is crucial in achieving the necessary charge transport in organic devices. Controlling of chain orientation has been observed to increase the charge mobility by an order magnitude in organic field effect transistors [13], enhance the conductivity in photovoltaic cells [14] and improve the power conversion efficiency in polymer solar cells [15]. Techniques such as spin coating [16], choice of solvent [17], floating film transfer [18], and solvent drying process [19] have been found helpful to some extent in controlling polymer chain orientation and crystallinity, in addition to other processing methods such as electrospinning [20], nanorubbing [21], and nanoimprint lithography [22]. However, the use of external sources such as the application of magnetic field [23], shear-flow fields, laser beams [24], and electric fields [20], [25] are a more straightforward and effective way of modifying the chain orientation. Out of these options, applying an electric field may be thought of as the most effortless approach to change the chain orientation. The polarizability of the conductive polymers induces a dipole in the presence of an electric field (EF). The dipole will possess an electrostatic charge which further results in the production of electrostatic energy. Any particle that has electrostatic potential energy might be affected by the presence of the EF [26]. An EF can alter a polymer particle's electrostatic charge and hence alter its orientation in the direction of the applied EF. Tassinari et al. [27] applied a vertical EF during the deposition of the chiral conductive polymer and witnessed chain alignment. Xi et al. [28] investigated the effect of an alternating current (AC) EF on P3AT polymer and studied the structural, mechanical and electrical properties of the aligned polymer. Shi et al. [29] achieved chain alignment for a thickness of 2 μm in MEH-PPV and reported the enhancement in carrier mobility by three times by applying a vertical EF during the formation of MEH-PPV film. Hao et al. [30] employed a horizontal EF to a 100 μL of MEH-PPV drop-casted on a glass slide and examined the conformational changes and photophysical behavior in by the film. The electric field-induced alignments of the polymers discussed so far have mostly been for microscopic scales. For planar devices, a long-range chain alignment of polymer films is essential and there have been relatively less reports on the EF-induced long-range alignment of polymer films. Recently, McFarland et al. [31] showed the assembling of macroscopic P3HT fibres by employing an external EF to P3HT solutions after forming nanowhiskers as fundamental building units. Although the work produced aligned P3HT nanofibers 5 cm long, the synthesis procedure did not give thin film and required a significant amount of processing time. Another key challenge in EF-induced chain alignment is the use of high EF values (in the range of kV/cm) which requires proper care and handling.

The chapter reports the long-range chain alignment of a polymer film on a lithium niobate substrate using a horizontal DC electric field during film formation by the deposition process.

TH-3353_166102010

Lithium niobate is a piezoelectric material and has applications in ACT devices. The application of EF up to 750 V/cm has successfully achieved the chain alignment at the macroscopic scale necessary for fabricating planar ACT devices. The chain alignment has been verified and characterized using a Raman spectrometer. The chain alignment is further quantified by calculating the dichroic ratio (DR) of the Raman peaks in the presence and absence of EF. In addition, the conductivity of the film is measured at parallel to perpendicular angles with respect to the direction of EF to confirm the direction of chain alignment.

5.1 Experimental setup

The work investigates the effect of the application of a horizontal EF on the chain conformation of a conjugated polymer. The application of a horizontal EF during the deposition process of the conjugated polymer film is achieved by applying a DC voltage between two aluminum (Al) metal plates, as shown in the schematic diagram in Figure 5.1(a).

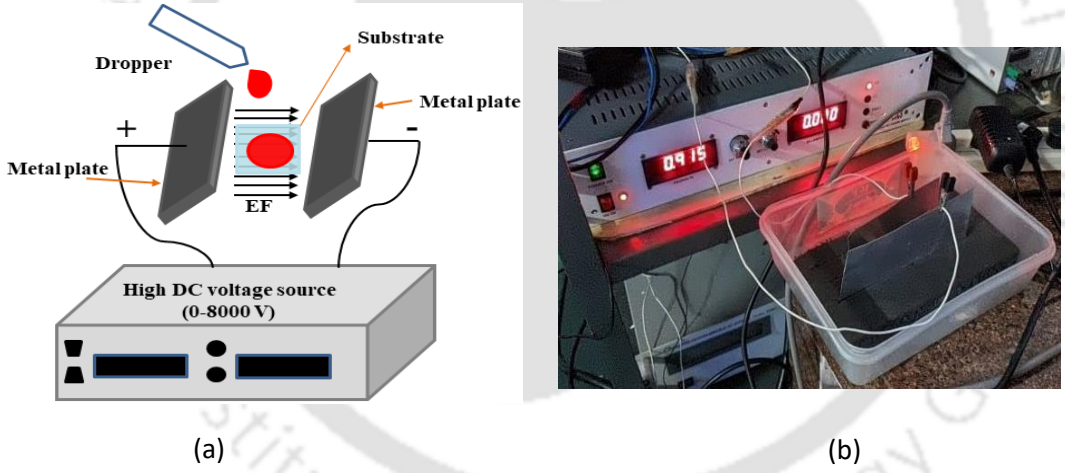

Figure 5.1: (a) Schematic of the experimental set up consisting of high DC voltage generator and parallel metal plates. (b) Image of the experimental setup.

We employed a high DC electrical voltage power source (HVPS, model EHT-11, SES Instruments Pvt. Ltd, India) to supply the DC voltage across the metal plates. An electric field will be created between the metal plates as a result of the supplied voltage, and its strength may be altered by adjusting the gap between the plates. The EF was increased from 0 to a maximum of 750 V/cm. The polymer film is deposited on a substrate between the metal plates in the presence of the EF. Figure 5.1(b) displays the setup used in this experiment. The thin film of MEH-PPV (commercially purchased from Sigma Aldrich) polymer was formed on the surface of a lithium niobate substrate by drop casting method. In previous studies [30], [31],

TH-3353_166102010

measurements of polymer chain alignment were made with polymer samples that were significantly dilute. In the present work, a 12 mg/ml solution of MEH-PPV in polar solvent of chlorobenzene was prepared by magnetically stirring the solution for 30 minutes at a temperature of 70–75 ^{O}C and then cooled down to room temperature. The solution was then drop-casted onto the substrate and then allowed to air dry entirely in the presence of the EF, as shown in Figure 5.1(a). The thickness of the MEH-PPV film was found to be nearly 1–2 μm as measured by the surface profiler. A drop-casted film without EF was also formed for comparison with the films cast under EF. For simplicity, we denote the drop casted film in the absence and presence of EF as D-cast and E-cast films, respectively.

5.2 Chain alignment analysis

5.2.1 Raman spectra analysis

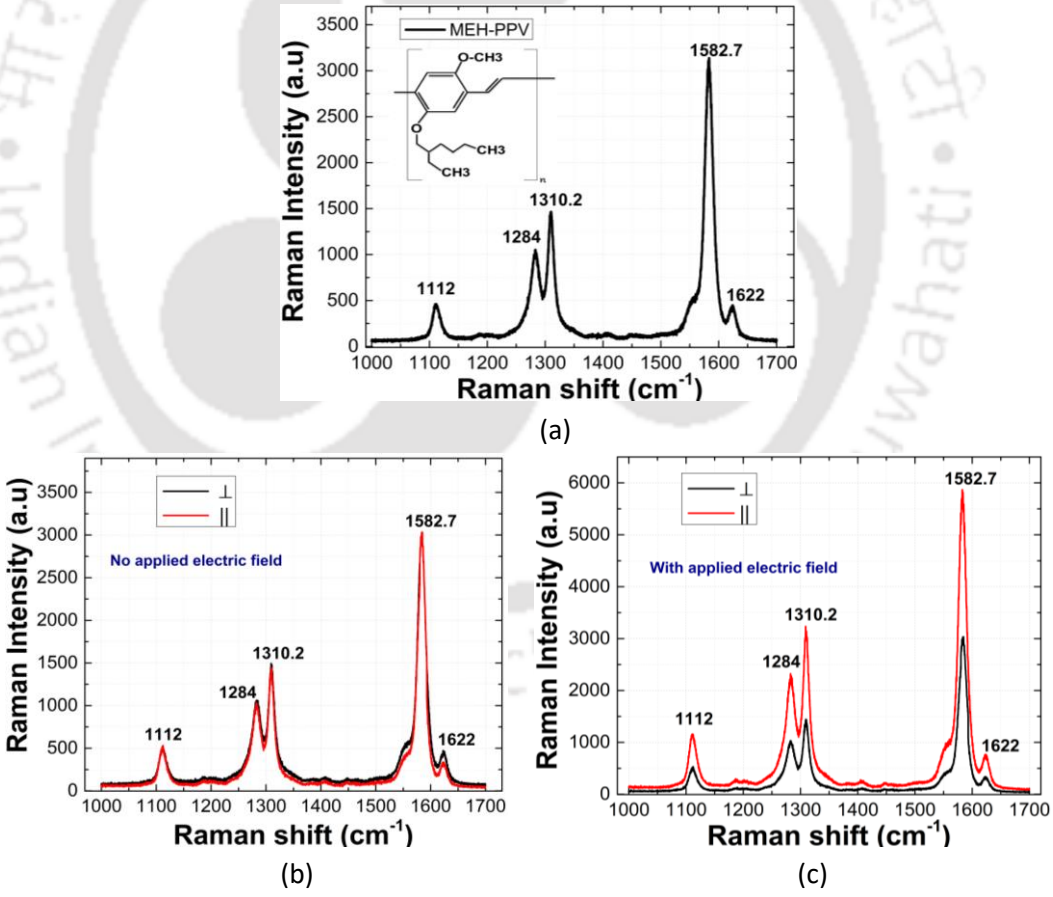

Figure 5.2: (a) Unpolarised Raman spectra of MEH-PPV film. (b) Polarised Raman spectra of D-cast MEH-PPV film under no EF. (c) Polarized Raman spectra of E- cast MEH-PPV film under the influence of EF.

TH-3353_166102010

The polymer chain orientation was investigated using Polarized Raman spectroscopy [32]. Polarized Raman spectra were obtained using a Raman Spectrometer, Horiba LabRAM HR800, equipped with a 785 nm laser and a light polarizer. The unpolarized Raman spectra, as shown in Figure 5.2(a), of drop casted MEH-PPV film were found to be consistent with that reported by many researchers [33], [34]. The inset of the figure shows the chemical structure of the MEH-PPV semiconducting polymer. Polarized Raman spectra of the MEH-PPV films formed in the presence or absence of EF were obtained to confirm the alignment of the polymer film. The polarized Raman spectra of the polymer films were measured using two mutually parallel and perpendicular polarizations. For both the D-cast and E-cast films, polarized Raman spectra were obtained with the mutually perpendicular ($\perp$) incident and scattered polarization vectors, and the spectra were compared to those obtained with mutually parallel (||) incident and scattered polarization vectors.

Figures 5.2(b) and 5.2(c) reveal the effect of EF on the polymer chain orientation. For the D-cast films, as observed in Figure 5.2(a), the Raman intensities are equal for both the perpendicular and parallel polarizations indicating the random orientation of the polymer chains. However, the parallel polarization has a very different peak intensity than the perpendicular polarization for the E-cast films indicating an alignment of chains in the polymer film. The laser beam encounters nearly the same number of bonds and their corresponding changes in dipole moments for random chain orientation at any polarization angle, leading to equal peak intensities. However, the parallel component has a higher peak intensity for aligned orientation than the perpendicular component. The high peak intensity for parallel polarized laser suggests that the polymer orientation is affected by the applied EF. It is anticipated that the MEH-PPV dipole moment [35] interaction with the EF causes the alignment of the polymer chains along the direction of the EF. The EF straightens the backbone of the macroscopic chain axis as the dipole moment forms an angle with respect to the macroscopic chain axis [35].

5.2.2 Dichroic ratio calculation

Figure 5.3(a) shows the effect of the magnitude of EF on the chain alignment in the polymer. As the field is increased from 0 to 300 V/cm, the Raman peak intensities for the parallel polarized component increase indicating a more significant number of polymer chains getting aligned. The Raman spectra show the characteristics bands [36] of MEH-PPV: 1112 cm^{-1} (mixtures of C-C stretching and C-H in-plane-bending vibration), 1284 cm^{-1} (C=C stretching band of benzene ring), 1310 cm^{-1} (C=C stretching coupled to C-H bending of vinyl group), 1582 cm^{-1} (C-C stretching band of benzene ring), and 1623 cm^{-1} (C=C stretching band of vinyl

TH-3353_166102010

group). A method of quantifying the degree of alignment in a polymer is calculating the dichroic ratio (DR) of the polarized spectra. DR is the ratio of parallel-polarized to perpendicularly polarized infrared peak intensities for a particular vibration [37]. Ideally, DR is 1 for a random chain orientation, and DR is infinite for fully aligned polymer chains [20].

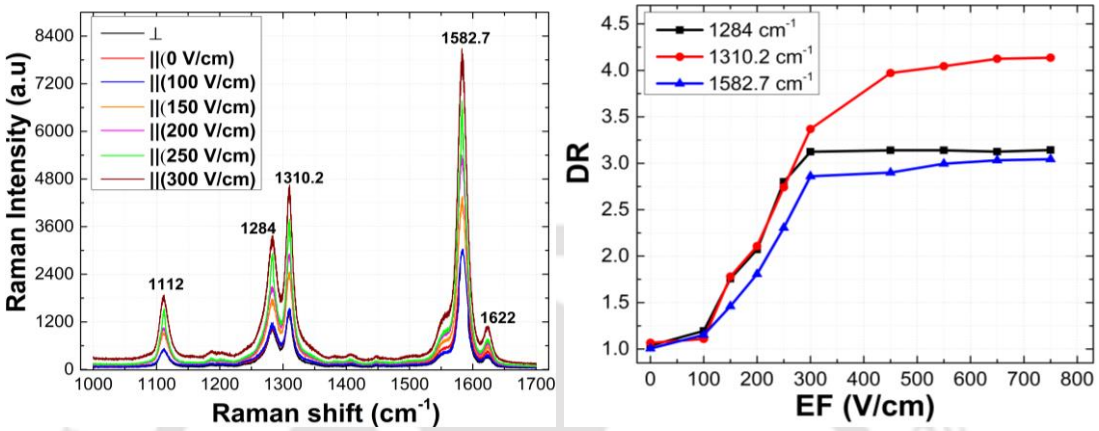

Figure 5.3: (a) Polarized Raman spectra for an EF ranging from 0 to 300 V/cm. (b) Dichroic ratio (DR) plotted as a function of EF (0 to 750 V/cm).

However, in practice, the DR will not be infinite, and a higher dichroic ratio suggests a higher degree of chain alignment. The DR for D-cast film is around 1 for all the peaks in the Raman spectra of MEH-PPV. However, DR is found to be larger than 1 in the case of E-cast films and indicates the change in the dipole moment of the particular vibration that coincides with the alignment direction [20]. The increase in DR with greater EF shows that a more significant number of polymer chains are aligned. Figure 5.3(b) illustrates the DR calculated for three major Raman peaks as a function of the EF. DR values are different for each peak because the DR depends on the individual band rotation of the bonds. To fully understand the impact of an increase in EF on the chain alignment, the EF magnitude is further raised to 750 V/cm. The DR is nearly constant beyond 300 V/cm for the Raman peaks at 1284 cm^{-1} and 1582.7 $cm^{-1,}$ representing the stretching of carbon bonds in the benzene ring and beyond 450 V/cm for the Raman peak at 1310.2 cm^{-1} representing the C=C stretching coupled to C-H bending of vinyl group. It can be attributed to the fact that after attainment of the fully aligned polymer chains there is no further change in the backbone structure of the polymer.

TH-3353_166102010

5.2.3 I-V analysis

The accomplishment of chain alignment was further confirmed by fabricating a device, as illustrated in Figure 5.4(a).

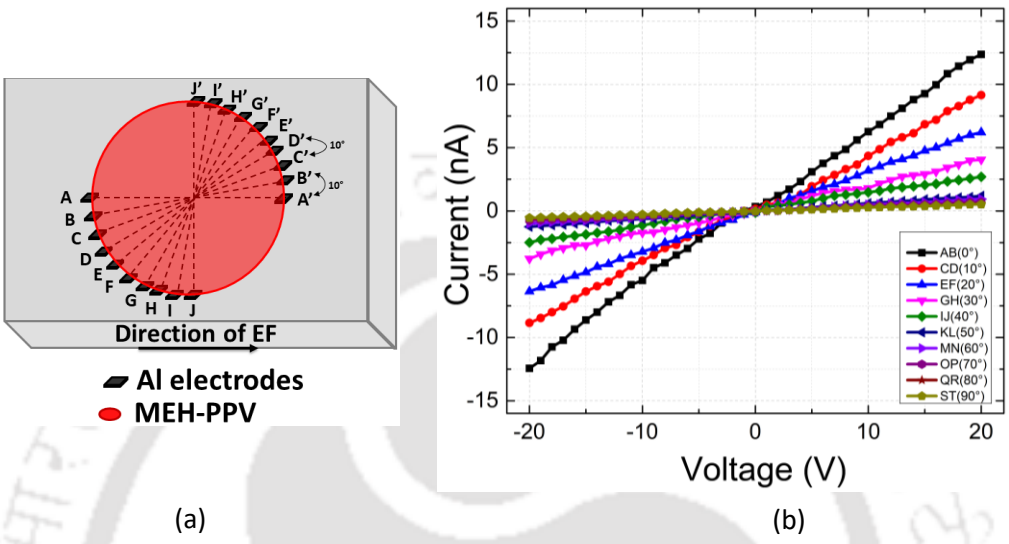

Figure 5.4: (a) Schematic of the device fabricated to verify the chain alignment under the influence of EF. (b) *I-V* characteristics measured between electrode pairs aligned in different angles with the applied EF direction during deposition process.

The device was fabricated to observe the charge transport in MEH-PPV chains at ten different angles from the direction of EF or the aligned chains axis. The fabrication of the device starts first with Al metal deposition on 20 positions on $LiNbO_3$ as electrodes, as depicted in Figure 5.4 (a)). MEH-PPV was drop cast on these electrodes to make ten pairs (each pair 5 cm apart) of two-terminal structures. A total of 10 electrode pairs in rotation of 10°, taking the direction of EF as the base axis, records the current in the chains oriented in an angle ranging from 0° to 90° to the base axis. AA', BB', CC', DD', EE', FF', HH', GG', II' and JJ' electrode terminals witness the current in a direction making an angle of 0°, 10°, 20°, 30°, 40°, 50°, 60°, 70°, 80° and 90°, respectively, to the direction of EF. The highest current value for the electrodes in 0° arrangement, as revealed in Figure 5.4(b), indicates that the polymer chains are entirely aligned in sequence (0°) with the direction of EF and not any other angle. The increased current for the two terminal AA' at 0° angle with the base axis indicates that the polymer chains are aligned parallel to the direction of EF. The calculated conductivity for the AA' terminal device is 3.43×10^{-10} S cm^{-1}, an order magnitude higher than reported in the literature [38].

TH-3353_166102010

5.3 Intrachain versus interchain transport

Due to the morphology of conjugate polymers, two kinds of exciton transport modes are proposed: Interchain and Intrachain hopping. Interchain hopping refers to transferring exciton from one chain to another, while exciton transport along one single chain has been signified as intrachain, as shown in Figure 5.5(b). Models explaining Intrachain transport have been proposed by R. Meng et al., which described the transport along the length of a single chain depending on the location of the generated exciton [39]. It should be noted from Figure 5.5(a) that the conductivity for the intrachain transport is 20 times greater than the interchain. The application of the EF during the formation of MEH-PPV films straightens the polymer backbone chains and aligns the chains throughout the film [40]. In addition, the long-range alignment of the semiconducting polymer chains tends to cause the grain boundaries in the film to disappear [41], [42]. The injected carriers experience lower barriers while travelling along the backbone of the chain resulting in dominant intrachain [43], [44] transport along the conjugated backbone with occasional π-π hopping to the onward chains.

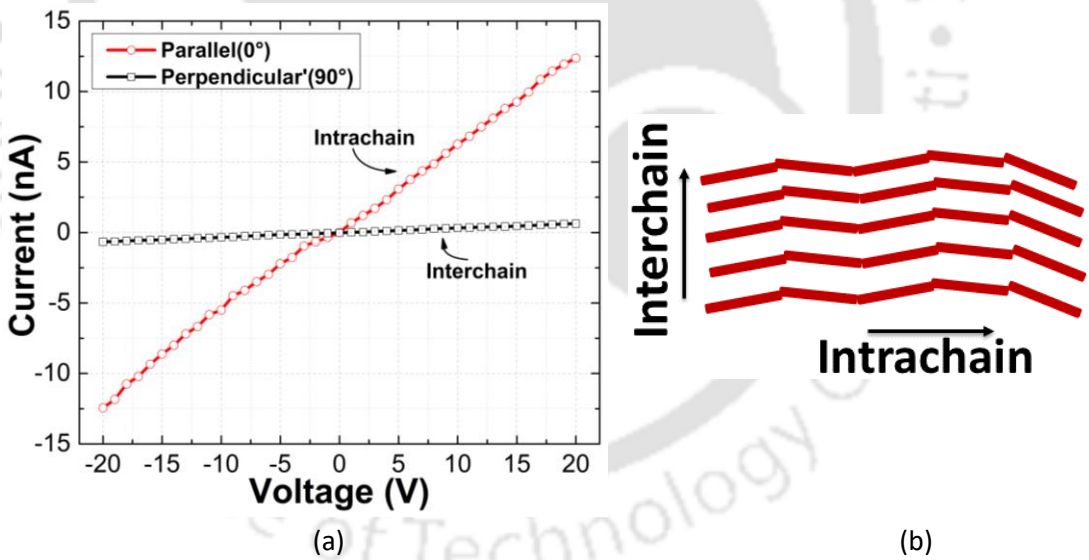

Figure 5.5: (a) I-V characteristics measured between electrode pairs aligned in parallel and perpendicular angles with the applied EF direction signifying (b) the depicted intrachain and interchain transport.

In contrast, the charge transport perpendicular to EF is interchain [44], [45] charge transport essentially through the π-π hopping from one chain to the neighbouring chain, hence requiring more energy than intrachain transport. Furthermore, the number of hops across the chain will be considerably large; therefore, the resultant current is significantly less.

TH-3353_166102010

5.4 Conductivity of aligned chains

Figure 5.6 shows the conductivity of the MEH-PPV film measured along the EF direction over a wide range of EF applied during the formation of MEH-PPV film and the error bars indicating standard deviation for a total of eight devices. It is evident that as the EF strength increases, the degree of alignment in the polymer chains increases, resulting in higher conductivity. There is no further improvement in conductivity beyond EF of 450 V/cm, indicating the highest degree of chain alignment. The results are consistent with the Raman spectra analysis shown in Figure 5.3(b).

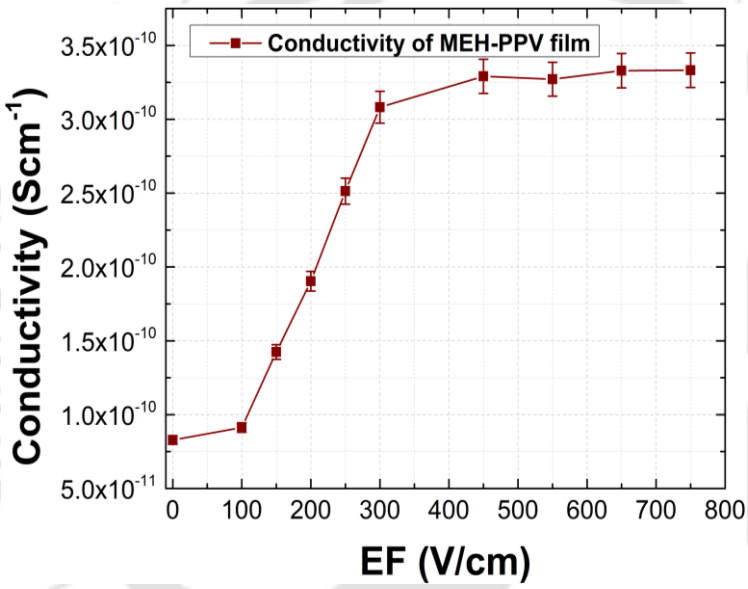

Figure 5.6: Plot of conductivity of the MEH-PPV film measured along the EF direction versus magnitude of EF.

5.5 DC electrical setup

Finally, a simple electrical setup has been developed for applying EF during film formation via the drop-casting method. It consists of a bridge rectifier, capacitor filter and two parallel Al metal plates, as shown in Figure 5.7(a) schematic diagram. The image of constructed setup is shown in Figure 5.7(b). The input to the setup is an AC mains supply of 220 V AC which results in a maximum DC output voltage, $V_{o,}$ of 300 V across the metal plates. This DC voltage formed across the Al metal plates results in generating a horizontal EF whose strength can be varied by adjusting the distance between the plates. The bridge rectifier works as follows: During the positive half cycle of the input AC waveform, diodes D2 and D4 conduct and during the negative half cycle, diodes D1 and D3 conduct resulting in full wave

TH-3353_166102010

rectification. The capacitor filter smoothens the waveform and produces constant DC voltage output, V_o. A power resistor R is used for short circuit protection. If V_o is applied across two parallel metal plates separated by distance d, the EF between the plates is calculated as V_o/d. Considering that the minimum space required to accommodate a device is about 0.5 cm, the maximum value of the EF would be 600 V/cm. Thus, this simple electrical setup can be used for obtaining drop-casted polymer films with aligned chains.

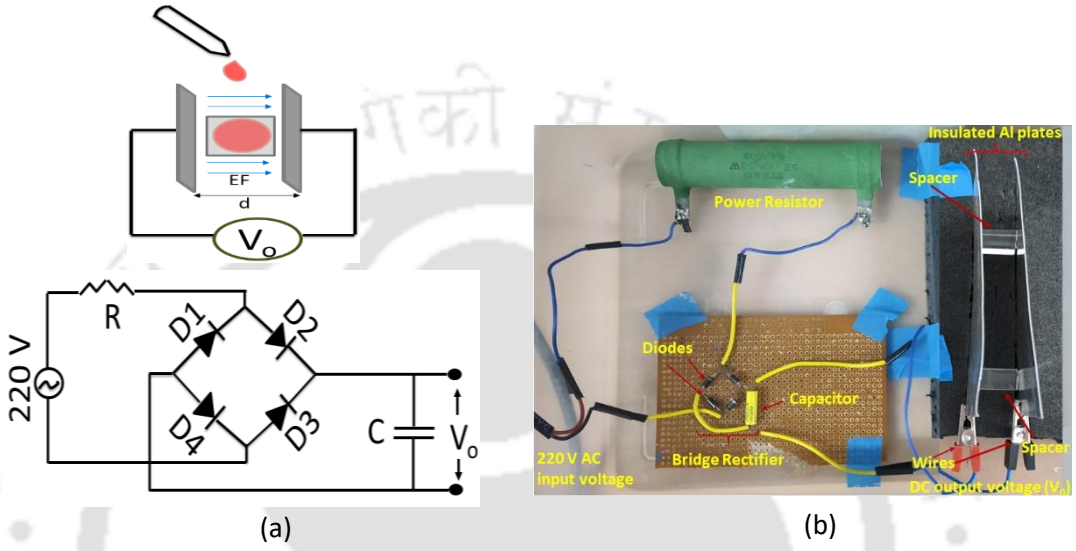

Figure 5.7: (a) Schematic of the experimental set up and electric circuit consisting bridge rectifier and metal plates. (b) Image of the experimental set up.

5.6 Summary

In summary, the work presents a method to obtain polymer films with highly aligned chains by applying EF during the formation of polymer film by drop casting. The polymer chains are aligned in macroscopic scales over a distance of 5 cm along the direction of the applied EF and it is verified by analyzing the polarized Raman spectra of the polymer film. The polar property of the polymer leads to the formation of an electric dipole in the presence of EF and results in the ordering of the polymer chains in the direction of the EF. The chain alignment of the MEH-PPV film has been quantified by calculating the DR of the Raman peaks in the presence and absence of EF. As the magnitude of EF is increased, DR initially increases indicating alignment of chains and saturates after achieving the highest degree of chain alignment. In addition, the chain alignment in MEH-PPV polymer has been verified by measuring the conductivity of the film along and across the direction of applied EF. The conductivity of the film measured parallel to the EF direction is significantly higher than that in perpendicular direction. When the chains are aligned, grain boundaries are reduced and charge carriers are able to move along the polymer backbone with less energy. However, the

TH-3353_166102010

conductivity measured across the chains is low indicating a restricted amount of transport since it requires high energy for the charge carriers to hop from one chain to the adjacent chain and travel across large number of chains. It has been found that as EF increases the conductivity of the MEH-PPV polymer film also increases and saturates after achieving maximum chain alignment. Finally, a simple and effective electrical set up has been constructed to apply DC EF during the polymer film formation attaining chain alignment.

भारतीय प्रौद्योगिकी संस्थान गुवाहाटी • Indian Institute of Technology Guwahati •

TH-3353_166102010

5.7 References

[1] Y. Li *et al.*, "Built-in voltage enhanced by: In situ electrochemical polymerized undoped conjugated hole-transporting modifiers in organic solar cells," *J. Mater. Chem. C*, vol. 8, no. 8, pp. 2676–2681, 2020, doi: 10.1039/c9tc06140a.

[2] L. Zhan *et al.*, "Over 17% efficiency ternary organic solar cells enabled by two non-fullerene acceptors working in an alloy-like model," *Energy Environ. Sci.*, vol. 13, no. 2, pp. 635–645, 2020, doi: 10.1039/c9ee03710a.

[3] R. Chen *et al.*, "Efficient synthesis and photovoltaic properties of highly rigid perylene-embedded benzothiazolyls," *Polym. Chem.*, vol. 7, no. 4, pp. 780–784, 2016, doi: 10.1039/c5py01791b.

[4] H. Sirringhaus, "Device physics of solution-processed organic field-effect transistors," *Adv. Mater.*, vol. 17, pp. 2411–2425, 2005, doi: 10.1002/adma.200501152.

[5] B. S. Ong, Y. Wu, P. Liu, and S. Gardner, "High-performance semiconducting polythiophenes for organic thin-film transistors," *J. Am. Chem. Soc.*, vol. 126, no. 11, pp. 3378–3379, 2004, doi: 10.1021/ja039772w.

[6] H. Friend, R *et al.*, "Electroluminescence in conjugated polymers," *Nat. Chem.*, vol. 397, pp. 121–128, 1995.

[7] H. H. Chou *et al.*, "A chameleon-inspired stretchable electronic skin with interactive colour changing controlled by tactile sensing," *Nat. Commun.*, vol. 6, 2015, doi: 10.1038/ncomms9011.

[8] M. C. Choi, Y. Kim, and C. S. Ha, "Polymers for flexible displays: From material selection to device applications," *Prog. Polym. Sci.*, vol. 33, no. 6, pp. 581–630, 2008, doi: 10.1016/j.progpolymsci.2007.11.004.

[9] T. L. Benanti and D. Venkataraman, "Organic solar cells : An overview focusing on active layer morphology," *Photosynth Res .*, vol. 87, pp. 73–81, 2006, doi: 10.1007/s11120-005-6397-9.

[10] A. L. Briseno *et al.*, "Self-assembly, molecular packing , and electron transport in n-type polymer semiconductor nanobelts," *Chem. Mater.*,vol. 20, pp. 4712–4719, 2008.

[11] A. R. Aiyar, J. Il Hong, and E. Reichmanis, "Regioregularity and intrachain ordering: Impact on the nanostructure and charge transport in two-dimensional assemblies of poly(3-hexylthiophene)," *Chem. Mater.*, vol. 24, no. 15, pp. 2845–2853, 2012, doi: 10.1021/cm202700k.

[12] Y. Yao, H. Dong, and W. Hu, "Ordering of conjugated polymer molecules: Recent advances and perspectives," *Polym. Chem.*, vol. 4, no. 20, pp. 5197–5205, 2013, doi: 10.1039/c3py00131h.

[13] C. Luo *et al.*, "General strategy for self-assembly of highly oriented nanocrystalline semiconducting polymers with high mobility," *Nano Lett.*, vol. 14, no. 5, pp. 2764–2771, 2014, doi: 10.1021/nl500758w.

[14] F. C. Tang *et al.*, "Alignment of poly(3,4-ethylenedioxythiophene) polymer chains in

TH-3353_166102010

photovoltaic cells by ultraviolet irradiation," *J. Mater. Chem.*, vol. 22, no. 42, pp. 22409–22417, 2012, doi: 10.1039/c2jm34556k.

[15] Y. Yang, K. Mielczarek, A. Zakhidov, and W. Hu, "Effects of nanostructure geometry on polymer chain alignment and device performance in nanoimprinted polymer solar cell," *Org. Photonic Mater. Devices XV*, vol. 8622, p. 862211, 2013, doi: 10.1117/12.2008394.

[16] D. M. Delongchamp *et al.*, "Variations in semiconducting polymer microstructure and hole mobility with spin-coating speed," *Chem. Mater*, vol. 17, no. 23, p. 5610, 2005.

[17] M. Liu *et al.*, "Controlling morphology and aggregation in semiconducting polymers: The role of solvents on lasing emission in poly[2-methoxy-5-(20-ethylhexyloxy)- 1,4-phenylene-vinylene]," *Materials (Basel).*, vol. 10, no. 7, pp. 1–14, 2017, doi: 10.3390/ma10070706.

[18] D. S. Yang, K. Chung, and J. Kim, "Controlled alignment of polymer chains near the semiconductor-dielectric interface," *Org. Electron.*, vol. 76, p. 105484, 2020, doi: 10.1016/j.orgel.2019.105484.

[19] D. H. Kim, Y. Jang, Y. D. Park, and K. Cho, "Controlled one-dimensional nanostructures in poly(3-hexylthiophene) thin film for high-performance organic field-effect transistors," *J. Phys. Chem. B*, vol. 110, no. 32, pp. 15763–15768, 2006, doi: 10.1021/jp062899y.

[20] M. V. Kakade, S. Givens, K. Gardner, K. H. Lee, D. B. Chase, and J. F. Rabolt, "Electric field induced orientation of polymer chains in macroscopically aligned electrospun polymer nanofibers," *J. Am. Chem. Soc.*, vol. 129, no. 10, pp. 2777–2782, 2007, doi: 10.1021/ja065043f.

[21] S. Nagamatsu *et al.*, "Backbone arrangement in 'friction-transferred' regioregular poly(3-alkylthiophene)s," *Macromolecules*, vol. 36, no. 14, pp. 5252–5257, 2003, doi: 10.1021/ma025887t.

[22] D. Cui, H. Li, H. Park, and X. Cheng, "Improving organic thin-film transistor performance by nanoimprint-induced chain ordering," *J. Vac. Sci. Technol. B Microelectron. Nanom. Struct.*, vol. 26, no. 6, pp. 2404–2409, 2008, doi: 10.1116/1.3013301.

[23] T. Kimura, H. Ago, M. Tobita, S. Ohshima, M. Kyotani, and M. Yumura, "Polymer composites of carbon nanotubes aligned by a magnetic field," *Adv. Mater.*, vol. 14, no. 19, pp. 1380–1383, 2002.

[24] W. M. Gibbons, P. J. Shannon, S.-T. Sun, and B. J. Swetlin, "Surface-mediated alignment of nematic liquid crystals with polarised laser light," *Nature*, vol. 351, pp. 49–50, 1991.

[25] Y. Xi and L. D. Pozzo, "Electric field directed formation of aligned conjugated polymer fibers," *Soft Matter*, vol. 13, no. 21, pp. 3894–3908, 2017, doi: 10.1039/c7sm00485k.

[26] J. M. J. LaFreniere, E. J. Roberge, and J. M. Halpern, "Review— Reorientation of polymers in an applied electric field for electrochemical sensors," *J. Electrochem. Soc.*, vol. 167, no. 3, p. 037556, 2020, doi: 10.1149/1945-7111/ab6cfe.

TH-3353_166102010

[27] F. Tassinari, S. P. Mathew, C. Fontanesi, L. Schenetti, and R. Naaman, "Electric-field-driven alignment of chiral conductive polymer thin films," *Langmuir*, vol. 30, no. 16, pp. 4838–4843, 2014, doi: 10.1021/la500657e.

[28] Y. Xi and L. D. Pozzo, "Electric field directed formation of aligned conjugated polymer fibers," *Soft Matter*, vol. 13, no. 21, pp. 3894–3908, 2017, doi: 10.1039/c7sm00485k.

[29] Q. Shi *et al.*, "Enhancement of carrier mobility in MEH-PPV film prepared under presence of electric field," *Chem. Phys. Lett.*, vol. 425, no. 4–6, pp. 353–355, 2006, doi: 10.1016/j.cplett.2006.05.046.

[30] X. T. Hao, N. Y. Chan, D. E. Dunstan, and T. A. Smith, "Conformational changes and photophysical behavior in Poly[2-methoxy-5-(2′-ethyl-hexyloxy)-1,4-phenylene vinylene] Thin films cast under an electric field," *J. Phys. Chem. C*, vol. 113, no. 27, pp. 11657–11661, 2009, doi: 10.1021/jp901498a.

[31] F. M. McFarland *et al.*, "Electric field induced assembly of macroscopic fibers of poly(3-hexylthiophene)," *Polymer (Guildf).*, vol. 151, pp. 56–64, 2018, doi: 10.1016/j.polymer.2018.07.062.

[32] S. Frisk, R. M. Ikeda, D. B. Chase, and J. F. Rabolt, "Determination of the molecular orientation of poly(propylene terephthalate) fibers using polarized Raman spectroscopy: A comparison of methods," *Appl. Spectrosc.*, vol. 58, no. 3, pp. 279–286, 2004, doi: 10.1366/000370204322886618.

[33] B. R. Moraes, N. S. Campos, A. C. C. Barra, and C. M. S. Izumi, "Surface-enhanced Raman scattering of MEH-PPV on gold and silver nanoparticles," *J. Spectrosc.*, vol. 2018, 2018, doi: 10.1155/2018/6924758.

[34] S. H. Yang, P. Le Rendu, T. P. Nguyen, and C. S. Hsu, "Fabrication of MEH-PPV/SiO_2 and MEH-PPV/TiO_2 nanocomposites with enhanced luminescent stabilities," *Rev. Adv. Mater. Sci.*, vol. 15, no. 2, pp. 144–149, 2007.

[35] T. W. Hagler, K. Pakbaz, and A. J. Heeger, "Polarized-electroabsorption spectroscopy of a soluble derivative of poly(p-phenylenevinylene) oriented by gel processing in polyethylene: Polarization anisotropy, the off-axis dipole moment, and excited-state delocalization," *Phys. Rev. B*, vol. 49, no. 16, pp. 968–975, 1994, doi: https://doi.org/10.1103/PhysRevB.49.10968.

[36] B. R. Moraes, N. S. Campos, A. C. C. Barra, and C. M. S. Izumi, "Surface-enhanced raman scattering of MEH-PPV on gold and silver nanoparticles," *J. Spectrosc.*, vol. 2018, 2018, doi: 10.1155/2018/6924758.

[37] A. Maleki, Z. Seidali, M. S. Zakerhamidi, and M. H. M. Ara, "Dichroic ratio and order parameters of some Sudan dyes doped in nematic liquid crystalline matrix," *Optik (Stuttg).*, vol. 126, no. 24, pp. 5473–5477, 2015, doi: 10.1016/j.ijleo.2015.09.100.

[38] M. M. Szindler, M. Szindler, and L. A. Dobrzański, "The structure and conductivity of polyelectrolyte based on MEH-PPV and potassium iodide (KI) for dye-sensitized solar cells," *Open Phys.*, vol. 15, no. 1, pp. 1022–1027, 2017, doi: 10.1515/phys-2017-0127.

[39] and A. Z. E. Najafi, B. Liao, T. Scarborough, "Imaging surface acoustic wave dynamics in semiconducting polymers by scanning ultrafast electron microscopy,"

TH-3353_166102010

Ultramicroscopy, vol. 184, pp. 46–50, 2018, doi: 10.1016/j.ultramic.2017.08.011.

[40] M. Xiao *et al.*, "Charge transport physics of a unique class of rigid-rod conjugated polymers with fused-ring conjugated units linked by double carbon-carbon bonds," *Sci. Adv.*, vol. 7, no. 18, pp. 1–14, 2021, doi: 10.1126/sciadv.abe5280.

[41] L. H. Jimison, M. F. Toney, I. McCulloch, M. Heeney, and A. Salleo, "Charge-transport anisotropy due to grain boundaries in directionally crystallized," *Adv. Mater.*, vol. 21, pp. 1568–1572, 2009.

[42] H.-R. Tseng *et al.*, "High-mobility field-effect transistors fabricated with macroscopic aligned semicondcuting polymers," *Adv. Mater.*, vol. 26, pp. 2993–2998, 2014.

[43] K. Johnson *et al.*, "Control of intrachain charge transfer in model systems for block copolymer photovoltaic materials," *J. Am. Chem. Soc.*, vol. 135, no. 13, pp. 5074–5083, 2013, doi: 10.1021/ja3121247.

[44] E. Collini and G. D. Scholes, "Coherent intrachain energy migration in a conjugated polymer at room temperature," *Science*, vol. 323, pp. 369–374, 2009.

[45] T. Nguyen, I. B. Martini, J. Liu, and B. J. Schwartz, "Controlling interchain interactions in conjugated polymers : The effects of chain morphology on exciton-exciton annihilation and aggregation in MEH-PPV films," *J. Phys. Chem. B*, vol. 104, pp. 237–255, 2000, doi: 10.1021/jp993190c.

TH-3353_166102010

Chapter 6

Development & Demonstration of Charge Transfer Devices with Aligned Polymer Chains

Ever since the invention of vacuum tube circuits, the idea of charge transfer has been drawn from static and dynamic registers that use discrete component devices. In semiconductor technology, a charge transfer device (CTD) is one that relies on the transmission of charges in discrete packets along or below the surface. For the past two decades, CTDs have found widespread use in shift registers, imaging systems, dynamic memories, and high-speed filtering [1]–[3]. Charge-coupled devices (CCDs) and bucket brigade devices (BBDs) are the two basic ways to build CTDs. Bucket-brigade electronics is a well-known charge transfer idea that has been implemented using standard technology in both a bipolar form and MOS version [4], [5]. However, the idea of a CCD is more recent.

Most of the current research and development in technology are focused on the twin goals of downsizing and simplifying already existing systems. The goals are evident in the electronics industry, where there is a continuous drive to decrease gadget size, weight, and power consumption. ACT is a relatively recent concept and technique that has charge transfer applications in both electrical and optoelectronic fields. As discussed in previous chapters, ACT is the fundamental concept of transporting charge carriers from one point to another with the assistance of SAW induced fields. In 1972, R. J. Strain [6] was the first to suggest obtaining charge transfer operation with acoustic waves by physically relating a CCD to a sinusoidal travelling wave model. He presented a numerical analysis of the CCD travelling wave model by equalizing the CCD operation using a clock cycle and the charge trapped in a travelling

TH-3353_166102010

potential wave. Gaalema et al. [7] physically integrated SAWs with CCDs in 1976. The electric field of an acoustic surface wave could drag minority carriers synchronously. The electric field associated with this piezoelectric surface wave can create travelling potential wells at the surface of an adjacent semiconductor that traps a considerable charge and sweeps it into the collector diode. Later, with development and refinement, physicists found prospects of employing SAW-assisted charge transport in buffer memory devices [8], shift registers [9], and other optoelectronic devices [10], [11]. As a result, the role of acoustic waves in charge transfer in inorganic materials has been thoroughly established. The charge transport in organic semiconductors using SAW has been successfully demonstrated and described in earlier chapters. Given the evolving use of organic materials in the electronics industry, organic semiconductors are a suitable material for further researching the design of a CTD prototype.

This chapter constructs and examines first-of-its-kind acoustic CTDs with aligned polymer chains. The device structures comprise of an aligned MEH-PPV film on a piezoelectric YZ lithium niobate substrate and orthogonal pair of IDTs. The orthogonal layout of IDTs emits SAW in different directions, one in the direction of chain alignment and the other in a direction orthogonal to the direction of chain alignment. It demonstrates experimentally the SAW-controlled intrachain and interchain transport of optically excited charge carriers. The voltage excitation is provided by applying a continuous RF signal using a Keysight PNA-L Network Analyzer (VNA) cascaded with MPS 150 RF probe station to the IDTs producing Rayleigh SAWs. The intrachain and interchain charge transport is recorded using Keithley 4200A-SCS Parameter Analyzer with the source-measurement units (SMUs). Further analysis of the performance of CTDs was carried out using a device structure consisting of two collector diodes constructed parallel within the aperture width of a single IDT. An experimental demonstration of the charge transfer process has been done with the description of charge leakage and device resolution. The work offers a foundational framework for the future design and development of a well-architecture device for imaging and other optoelectronic applications.

6.1 Device fabrication

The device fabrication process is the same as was mentioned in earlier chapters. The first device was fabricated to investigate the acoustical control of intrachain and interchain movements of charges in MEH-PPV. Two IDTs orthogonal to each other were formed on a lithium niobate substrate with two BEs. MEH-PPV polymer solution of 12 mg/ml in chlorobenzene was drop-casted in the area between the IDTs and on top of the BEs, forming the middle layer of the collector diodes in the presence of a DC EF. The solution was then

TH-3353_166102010

allowed to dry out entirely in the presence of the EF, and then the EF application was removed. The top electrodes are formed to complete the collector diode structures and to produce the device, as shown in Figure 6.1(a). The same fabrication processes were followed to construct the second device, which has one IDT of 20 μm finger width, an aligned MEH-PPV polymer layer and two collector diodes, as shown in Figure 6.1(b). The two collector diodes are each of 1 mm length kept at a distance of 0.75 mm apart from each other and within the IDT's aperture width (4 mm).

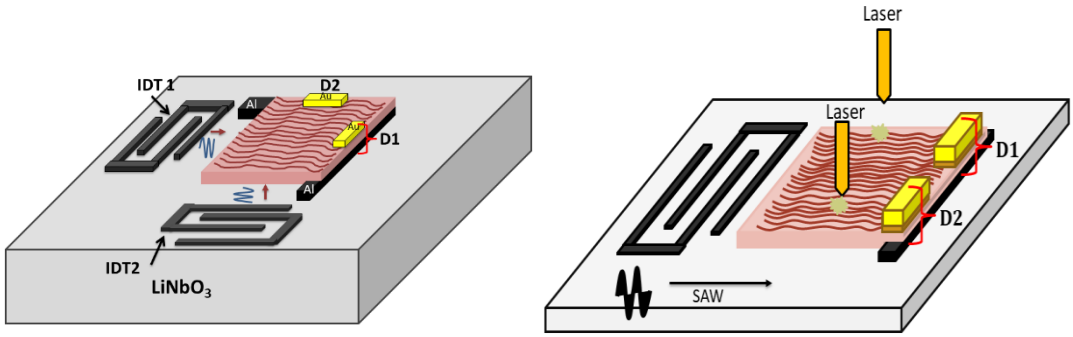

(a) (b)

Figure 6.1: (a) Orthogonal device structure to investigate the intrachain and interchain movements of charges assisted with SAW. (b) Single IDT CTD device with aligned polymer chains.

6.2 SAW-controlled intrachain and interchain transport

The ACT of optically generated charge carriers has been already described in the previous chapters. The excitons are separated, trapped and moved as spatially separated charge carriers along the SAW path and then collected at the collector diode. The energy of the SAW must be higher than the binding energy of the exciton in order for the ACT to be realized. Using the device shown in Figure 6.1(a) with two IDTs orthogonal to each other, aligned MEH-PPV chains, and two collector diodes facing each IDT, the intrachain and interchain movements of charges assisted with SAW were investigated. The polymer area between the orthogonal IDTs and collector diodes was illuminated to generate excitons optically.The current is measured separately from each collector diode with the corresponding IDTs excited. IDT1 transmitting SAW in the direction of aligned chains will record the intrachain charge transport. In contrast, IDT2 propagating perpendicular to the chain alignment direction will measure the interchain charge transport. Figure 6.2(a) shows the current density plot for the orthogonal device depicting SAW-controlled intrachain and interchain charge transport as a function of applied SAW RF power. As anticipated, the intrachain (along the chain) current is high compared to

TH-3353_166102010

the interchain (across the chain) current for the same RF power range. It can be explained by the fact that charge carriers dragged along the conjugated backbone of MEH-PPV by SAW with occasional hopping to the onward chains experience lower energy barriers as a result of chain alignment [12], [13]. However, interchain charge transport, which hops from one chain to the next, requires more energy compared to intrachain transport and hence has a higher threshold SAW power.

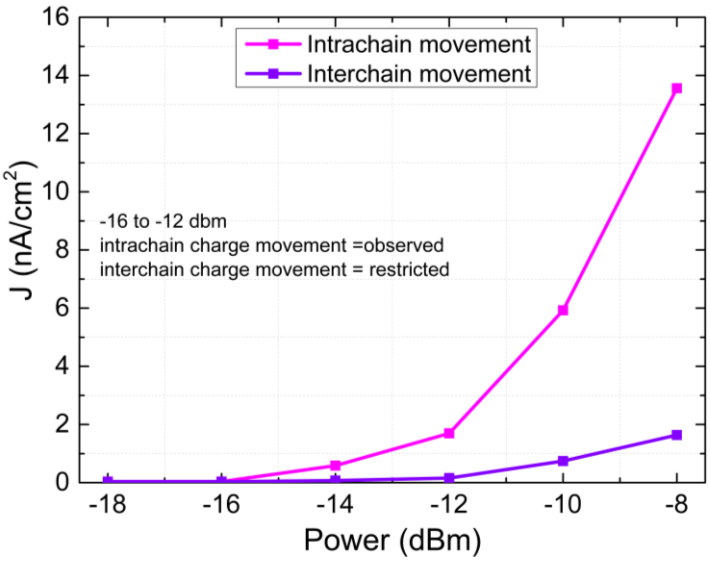

Figure 6.2: Current density (*J*) versus RF power plot depicting the SAW-controlled intrachain and interchain charge transport.

As was discussed in chapter 3, the ACT process involves the charge carriers being ionized, trapped, and dragged by the SAW along the path of propagation. The total energy offered by SAW for the exciton ionization, as mentioned in section 3.3.2 of chapter 3, is given as

$$E_{SAW} = \frac{1}{2} m^* (\mu\zeta)^2 + \frac{1}{2} \rho A^2 (\omega)^2 \qquad (6.1)$$

In addition, the acoustic drag force experienced by the charge carriers, as already described in section 4.3.2 of chapter 4, is

$$F = \frac{q^2 S}{c^2 KT} \frac{\omega^2 \tau_R}{[1+(\omega\tau_R)^2]} \qquad (6.2)$$

The minimum SAW power requisite for the ACT was found to be -16 dBm, as discussed in [14]. As seen in Figure 6.2, it can be inferred that for RF values below -16 dBm, no excitons

TH-3353_166102010

optically produced would be ionized. As a result, neither intrachain current nor interchain current was observed.

It is important to note that for the movement of the optically generated charge carriers across the chains, SAW has to provide energy not only for exciton ionization but also to overcome the hopping barrier across the chains. It can be assumed that between the RF power range of -14 to -12 dBm, SAW is able to provide energy to the optically generated charge carriers to hop across the chains and realize interchain transport. The energy needed to hop across interchain distance in a polymer is known as the interchain hopping barrier (E_h). The energy for the charge carriers to hop from one chain to the adjacent is typically in the range of 0.045–0.09 eV, as reported in the literature [15]–[17]. Using the general relation between energy and force, the corresponding force required for the interchain hopping, F_h, is then calculated to be around 0.0044–0.0067 fN. Using equation (6.2), the acoustic drag force offered by SAW is calculated. For RF powers of -14 dBm, -13 dBm, and -12 dBm, acoustic drag force, F was computed to be 0.0039 fN, 0.0051 fN, and 0.0069 fN, respectively. It implies that the RF power of around -13 dBm can be considered the threshold power required by SAW to transport the charge carriers across the chains.

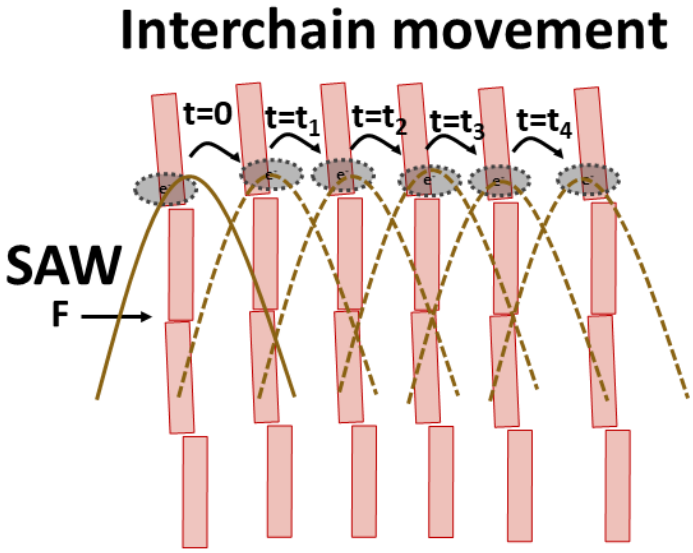

Figure 6.3: Schematic depicting process of SAW assisted interchain charge movement.

Figure 6.3 illustrates the schematic representation of the SAW-assisted interchain charge movement. When SAW travels along the interchain direction, it encounters a large number of chains and the charge carriers accumulate in the potential wells, as discussed in chapter 3. As SAW propagates through the polymer chains, potential wells will shift from one chain to the next and drag the accumulated charge carriers along with them. In addition, the propagation time of the SAW between chains is critical to the efficient transfer of charge carriers from one

TH-3353_166102010

chain to another via SAW. The time required for the charge carriers to move from one chain to another for the polymer known as the time constant for interchain hopping, τ_h, is generally a few tens of femtoseconds [19], [20]. For SAW velocity (c) of 3488 m/s and a polymer chain spacings of about 4 nanometres [16], [18], the SAW propagation time (τ_p) is approximately 1.25 picoseconds. The effective interchain hopping of the charge carriers is supported by the fact that the computed SAW propagation time across the chains is much greater than the time constant for interchain hopping. As a result, we may claim that it is possible to have a SAW-controlled intrachain and interchain transport of charge carriers in an organic semiconductor, and the power range between -16 dBm and -13 dBm is the power range where interchain movement is restricted, but intrachain movement is possible.

6.3 Performance of charge transfer device (CTD)

A CTD is characterized by its capacity to distinctively gather as many charge carriers as possible and suffer minimal charge crossover or leakage resulting into misleading data. Figure 6.1 (b) shows the structure of CTD on a piezoelectric substrate having a single IDT and two collector diodes, D1 and D2, at the opposite end and the polymer layer as a charge transport medium deposited between the IDT and diodes. The performance of the CTD has been evaluated by fabricating two devices: one with random MEH-PPV chains and the second with aligned MEH-PPV chains. A red laser is used to generate charge carriers in the polymer layer at different locations. The laser generates charge carriers in polymer at the point of incidence, A or B, as shown in Figure 6.4 (a). SAW will transport the charge carriers in the direction of propagation towards the collector diodes. Figure 6.4(a) shows the 2-D schematic of the fabricated CTD with random orientation of polymer chains. The collector diodes D1 and D2 are fabricated so that they fall within the aperture width of SAW and record the transport via SAW for each laser spot. When the laser is directed at spot A within the capture range of diode D1, the current detection at diode D2 should be minimal to ensure minimal charge crossover. Similarly, current detection at diode D1 should be at its lowest when the laser is focused at spot B inside the capture range of diode D2. For device 1, a charge leakage has been observed, as shown in Figure 6.4(b). For laser spot A beyond the capture range of diode D2, it has also been observed to detect some charges producing a current of 2.04 nA/cm^2. The charge detection at diode D2 can be explained by the fact that the random orientation of polymer chains might provide some path connecting the laser spot A and diode D2. It can be assumed that some of the optically generated charge carriers will select this easy path and navigate their way to diode D2 via SAW. In the instance that the entire surface of the active layer is illuminated, this charge leakage has the potential to add to the charges that were initially generated, which could result

TH-3353_166102010

in erroneous results. The charge leakage has been calculated to be around 23–24% for the SAW-assisted CTD with randomly oriented chains.

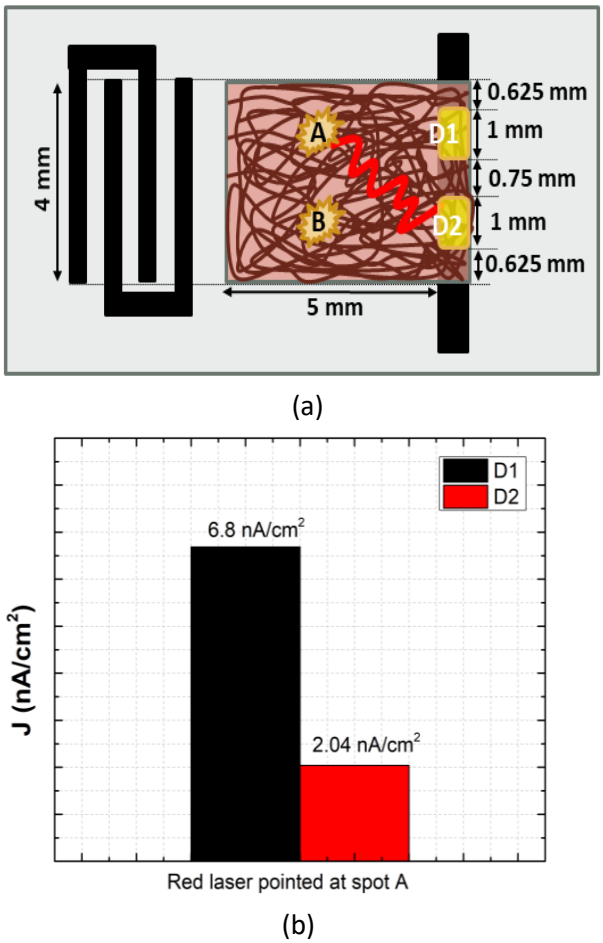

Figure 6.4: (a) 2D Schematic of device 1 CTD with random polymer orientation. (b) Current density observed at diode D1 and D2 for the laser spot at A.

The experiment was performed again using device 2 with aligned polymer chains, as shown in Figure 6.5(a). It can be seen from Figure 6.5(b) that diode D1 carries a high current of 12.2 nA/cm^{2,} and diode D2 shows a minimal current of 0.54 nA/cm^2 for the laser spot A. However, for the laser spot position B, diode D1 shows a minimal current of 0.56 nA/cm^2 and diode D2 shows a high current of 11.9 nA/cm^2. The observed current for this experiment is typically much greater than seen in the previous chapters for ACT. This increase in current is due to the reduced grain boundaries as a result of the formation of aligned chains, thus enhancing the conductivity of the polymer. For spots A and B, the charge crossover at the adjacent diodes has been computed and found to be 4–5%. The results indicate that for a well-aligned polymer layer, charges will face some barrier to spill from one chain to the next; hence, the charge leakage from the laser spot to the diodes adjacent to it is minimal. The result provides an effective way to realize that the intrachain transport has been successfully achieved and has

TH-3353_166102010

been able to deliver the optically excited charges to the designated collector diode. Another feature that defines a CTD is its resolution. The resolution of the constructed CTD with aligned chains will be defined by the minimum spacing between the SAW potentials as well as the separation between the collector diodes.

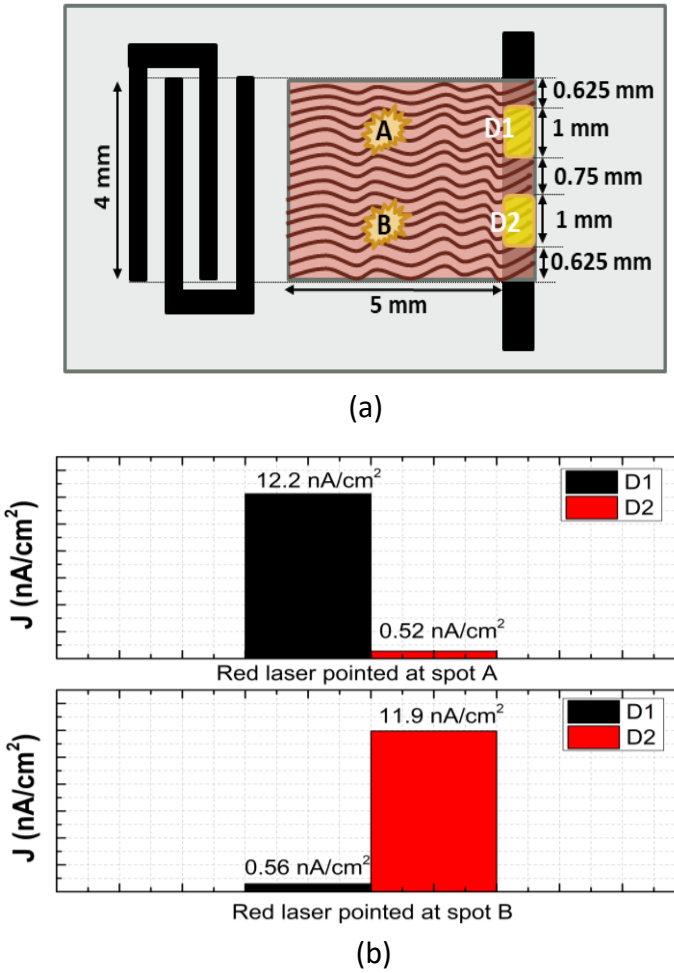

Figure 6.5: (a) 2D schematic of device 2 CTD with aligned polymer chains. (b) Current densities observed at diode D1 and D2 for the laser pointed at A and B.

A total of eight CTDs with aligned polymer chains were fabricated, and the charge leakage was calculated for each device. Figure 6.6 shows the bar diagram depicting the current leakage or spillage percentage calculated for eight devices with aligned polymer orientation. For our optical setup, the current spillage is 4–5% and has been found consistent for 6 out of 8 devices. This experiment demonstrates preliminary work that provides the base of a reliable SAW-assisted CTD for various optoelectronic applications.

TH-3353_166102010

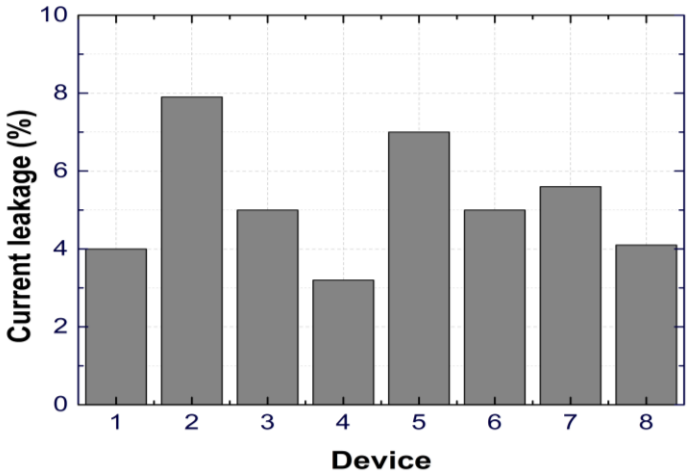

Figure 6.6: Bar diagram showing the current leakage for 8 CTDs.

6.4 Summary

In this chapter, a SAW controlled intrachain and interchain charge movement in MEH-PPV has been accomplished by fabricating a SAW device with an aligned MEH-PPV polymer layer and two IDTs, one transmitting SAW in the direction of chain alignment, and the other transmitting SAW orthogonal to the direction of chain alignment. As interchain movement requires more energy than intrachain transport, the threshold SAW power for interchain transport is higher than for intrachain transport. The performance of the CTDs has been evaluated using device structures consisting of a single IDT, polymer layer and two parallel collector diodes (D1 and D2) within the aperture width of the SAW. Devices having random and aligned MEH-PPV chain orientations have been tested. It is realized that the charge leakage for the device with random chain orientation is five times higher than that of the device with an aligned orientation. The minimal spacing between SAW potentials and collector diodes determines the resolution of the CTD. The results provide the groundwork for a SAW-assisted CTD that can be used in various optoelectronic and imaging applications.

TH-3353_166102010

6.5 References

[1] R. B. J. Warnar, *Impact of Charge-Transfer Device Technology on Computer Systems*. Washington, DC: NBS Special Publication, 1977.

[2] D. D. Buss and W. H. Bailey, "Applications of charge transfer devices to communication," *International Conference on Communications*, vol.1, pp 2-4, 1975.

[3] C. H. Sequin and M. F. Tompsett, "Charge transfer devices.," *Adv Electron Electron Phys Suppl*, vol. 1166, , 1977, doi: 10.1049/ep.1979.0133.

[4] F. L. J. Sangster and K. Teer, "Bucket-brigade electronics: New possibilities for delay, time-axis conversion, and scanning," *IEEE J. Solid-State Circuits*, vol. 4, no. 3, pp. 131–136, 1969.

[5] L. Boonstra and F. L. J. Sangster, "Charge-transfer devices," in *IEEE International Solid-State Circuits Conference*, 1972, pp. 5–7.

[6] R. J. Strain, "Properties of an idealized traveling-wave charge-coupled device," *IEEE Trans. Electron Devices*, vol. 19, no. 10, pp. 1119–1130, 1972, doi: 10.1109/T-ED.1972.17559.

[7] S. D. Gaalema, R. J. Schwartz, R. L. Gunshor, S. D. Gaalema, R. J. Schwartz, and R. L. Gunshor, "Acoustic surface wave interaction charge-coupled device," Appl. Phys. Lett., vol. 82, pp. 1–3, 1976.

[8] D. L. Smythe, R. W. Ralston, B. E. Burke, and E. Stern, "An acoustoelectric SAW/CCD device," *1978 Ultrason. Symp. Proceedings, IEEE*, pp. 16–19, 1978.

[9] D. L. Smythe and Ral, "Integrated surface acoustic wave/charge-coupled (SAW/CCD) signal processing devices," *SPIE Opt. Signal Process. C3I*, vol. 209, pp. 152–158, 1979.

[10] K. Tsubouchi, T. Higuchi, M. Nagao, and N. Mikoshiba, "Charge transfer by surface acoustic waves on a monolithic MIS structure," *Appl. Phys. Lett.*, vol. 33, no. 8, pp. 762–765, 1978, doi: 10.1063/1.90496.

[11] F. L. Augustine, R. J. Schwartz, and R. L. Gunshor, "Experimental observation of charge transfer by surface acoustic waves in a monolithic Metal/ZnO/SiO_2/Si (MZOS) device," *Ultrason. Symp.*, pp. 769–773, 1981.

[12] L. H. Jimison, M. F. Toney, I. McCulloch, M. Heeney, and A. Salleo, "Charge-transport anisotropy due to grain boundaries in directionally crystallized," *Adv. Mater.*, vol. 21, pp. 1568–1572, 2009.

[13] H.-R. Tseng *et al.*, "High-mobility field-effect transistors fabricated with macroscopic aligned semiconducting polymers," *Adv. Mater.*, vol. 26, pp. 2993–2998, 2014.

[14] H. Mishra, P. Bhattacharjee, and H. B. Nemade, "Acoustic charge transport in organic semiconductor films," *J. Phys. D. Appl. Phys.*, vol. 55, no. 1, p. 015102, 2022, doi: https://doi.org/10.1088/1361-6463/ac9f20.

[15] P. L. Santos *et al.*, "Measurement of interchain and intrachain exciton hopping barriers in luminescent polymer," *J. Phys. Condens. Matter*, vol. 24, no. 1, 2012, doi: 10.1088/0953-8984/24/1/015801.

[16] R. Noriega, A. Salleo, and A. J. Spakowitz, "Chain conformations dictate multiscale charge transport phenomena in disordered semiconducting polymers," *Proc. Natl. Acad. Sci. U. S. A.*, vol. 110, no. 41, pp. 16315–16320, 2013, doi: 10.1073/pnas.1307158110.

TH-3353_166102010

[17] J. H. Bombile, S. Shetty, M. J. Janik, and S. T. Milner, “Polaron hopping barriers and rates in semiconducting polymers,” *Phys. Chem. Chem. Phys.*, vol. 22, no. 7, pp. 4032–4042, 2020, doi: 10.1039/c9cp06039a.

[18] M. G. Harrison, J. Grüner, and G. C. W. Spencer, “Analysis of the photocurrent action spectra of MEH-PPV polymer photodiodes,” *Phys. Rev. B*, vol. 55, no. 12, pp. 1–19, 1997, [Online]. Available: papers://dc5b7a66-c191-4125-90d3-2536c98d4438/Paper/p951.

[19] M. L. Grage, Y. Zaushitsyn, A. Yartsev, M. Chachisvilis, V. Sundström, and T. Pullerits, “Ultrafast excitation transfer and trapping in a thin polymer film,” *Phys. Rev. B - Condens. Matter Mater. Phys.*, vol. 67, no. 20, pp. 1–5, 2003, doi: 10.1103/PhysRevB.67.205207.

[20] A. Ruseckas *et al.*, “Ultrafast depolarization of the fluorescence in a conjugated polymer,” *Phys. Rev. B - Condens. Matter Mater. Phys.*, vol. 72, no. 11, pp. 1–5, 2005, doi: 10.1103/PhysRevB.72.115214.

TH-3353_166102010

Chapter 7

Conclusion & Future Scope

7.1 Conclusion

This chapter summarises the results obtained and provides insight into the potential prospects of the work. The work focuses on the integration of SAW with organic semiconductors and achieves the acoustic transport of optically generated charge carriers with the aid of SAW.

An overview of the concept of SAW and its fundamental effect on semiconductors is discussed, followed by a thorough literature survey on ACT. The use of COMSOL Multiphysics 5.3 has been discussed for 3D-Finite element simulation of Rayleigh SAW devices with different IDT dimensions. All the required approximations for the simulation geometry, boundary conditions, and Euler angles have been considered. The optimization of the aperture width and its effects on port matching have been covered prior to the microfabrication of the device structure. It has been established that the results of theoretical analysis, modelling, and fabrication equipment all produce the same resonance frequencies. Subsequently, an ambipolar transport of electrons and holes in organic semiconductor films up to a distance of 3 mm with the aid of SAW was demonstrated using a novel piezo substrate-organic semiconductor device structure. The theoretical analysis of the ACT is explained using a semi-classical Hamiltonian of the system. The findings confirmed the validity of the SAW-aided charge transport, in which excitons are trapped, separated, and carried along the SAW channel as spatially separated charge carriers before being collected at the collector (polymer) diode. The energy of the SAW must be higher than the exciton binding energy in order to realise the ACT. The interaction between the SAW and the charge carriers results in transferring the wave's energy and momentum to the charge carriers. The maximum charge capacity is determined to be independent of light intensity and dependent on SAW power and wavelength. Another acousto-optic characteristic of the device, such as the transfer efficiency, is defined and affected by the screening effect. Next, we have

TH-3353_166102010

demonstrated the interaction of two SAWs and how they can influence charge transport in an organic semiconductor. Since the acoustic drag force is a frequency-dependent term, it can be employed as a parameter in the acoustic control of charge carrier transport, which has been demonstrated using combinations of three frequencies. Subsequently, the experimental results reported the influence of HF wave on the charge transport by LF wave and vice versa. Additionally, it was demonstrated experimentally that charge carriers could move diagonally via orthogonal SAW beams of the same frequency. The organic active layer is the basic building block of all organic optoelectronic devices. It has been established that controlling the chain orientation of the active organic film can increase the conductivity and charge mobility of optoelectronic devices. Consequently, the attainment of long-range chain alignment of the MEH-PPV film is achieved using a DC EF. The MEH-PPV polymer chains are aligned in the direction of the applied EF, as revealed by the polarised Raman spectroscopy and electrical conductivity results. The long-range alignment of the polymer chains, which tends to diminish the grain boundaries in the film, leads to improved charge transport. Further, a simple and easy-to-use electrical setup is presented and shown for applying EF throughout the polymer deposition process to avoid the requirement for expensive DC sources. In addition, novel and first-of-its-kind acoustic CTDs with aligned polymer chains are designed and developed.

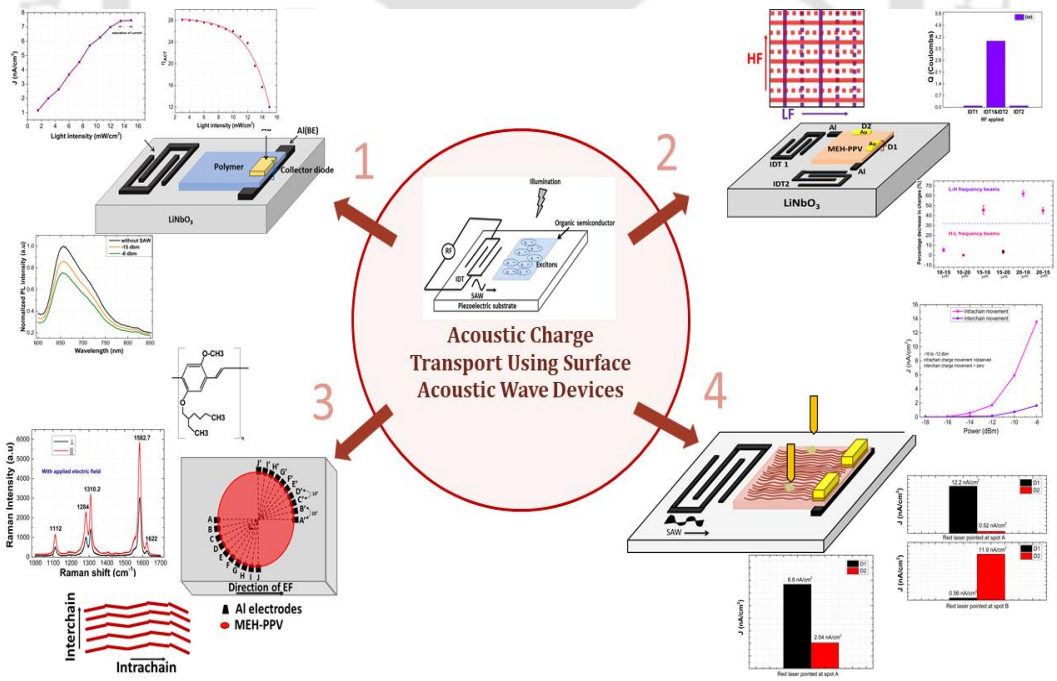

Figure 7.1: Schematic of the overview of the thesis.

A SAW-controlled intrachain and interchain transport of optically excited charge carriers in an organic semiconductor has been demonstrated and analysed based on the accomplishments of aligned polymer chains. The potential of CTDs with aligned and random polymer chain

TH-3353_166102010

orientations is investigated and compared in this research, establishing the foundation for the construction of devices for use in optoelectronic applications. Compared to the device with an aligned orientation, the charge leakage of random chain orientation is five times higher. A schematic of the thesis overview depicting all the major contributions of the research work is shown in Figure 7.1.

7.2 Future scope of the work

The present work investigates the prospects and potentials of charge carrier transfer in organic semiconductors using acoustic waves. Even though the results are promising, there is still potential for further growth and improvement. In the future, the current research project could be expanded in the following areas:

1. The ACT can be explored in materials like perovskites to study and understand the band edge modulation in these materials with SAW and obtain results to survey for potential applications in optoelectronics.
2. To further understand the effects of the acoustoelectric effect in the ultra-high frequency region, SAW devices that operate at frequencies higher than those employed in this thesis may be examined.
3. The impact of standing SAW on the ionization and transport of optically produced excitons on an organic semiconductor can be investigated and examined using a real-space micro-photoluminescence spectroscopy.
4. In order to further explore the acoustical influence on charge movement, a wide variety of angle combinations between two SAWs that interact with one another can be tested.
5. In order to employ the prototype for imaging applications, a proposed architecture for charge collection and signal processing of the charge transfer device can be conceptualized and constructed.

TH-3353_166102010

TH-3353_166102010

List of Abbreviations

ACT	Acoustic charge transport
AFM	Atomic force microscope
BE	Bottom electrode
CB	Conduction band
CCD	Charge-coupled device
CMOS	Complementary metal-oxide semiconductor
COM	Coupling of mode
CTD	Charge transfer device
EF	Electric field
FEM	Finite element method
FEA	Finite element analysis
GSG	Ground-source- ground
HF	High frequency
HMDS	Hexamethyldisilazane
HOMO	Highest occupied molecular orbital
IDT	Interdigital transducers
IL	Insertion loss
LF	Low frequency
LUMO	Lowest unoccupied molecular orbital
MEH-PPV	Poly[2-methoxy-5-(2'-ethylhexyloxy)-1,4-phenylene vinylene]
MSM	Metal-semiconductor-metal
NDS	Non-destructive sensing
P3HT	Poly(3-hexylthiophene)
PL	Photoluminescence
RF	Radio frequency
SAW	Surface acoustic wave
SMU	Source measuring unit
SWICC	Surface wave interaction CCD
SWNT	Single wall carbon nanotubes
TCD	Temperature coefficient of delay
TE	Top electrode

TH-3353_166102010

TTI	Triple transit interference
UV	Ultraviolet
VB	Valence band
VNA	Vector network analyzer

TH-3353_166102010

List of Symbols

a	IDT finger width
C_s	Capacitance per unit length of a single finger pair
E_{SAW}	Energy obtained from SAW
E_{BE} (0)	Binding energy of the polymer in absence of SAW
E_{BE}	Binding energy of the polymer in presence of SAW
F	Acoustic drag force
K^2	Electromechanical coupling coefficient
N	Maximum charge capacity
N_P	Number of finger pair
p	IDT pitch
R_{in}	Input resistance
S_{11}	Reflection coefficient
S_f	Mass sensitivity
t	Time
υ	SAW phase velocity
V_{in}	Voltage applied at the input port
V_{out}	Voltage applied at the output port
υ_f	Wave velocity of a free unconstrained surface
υ_m	Wave velocity of a metallized surface
W_a	Aperture width
Z_L	Load impedance
Z_0	Characteristic impedance

TH-3353_166102010

Φ	SAW field strength
Φ_0	Maximum amplitude of SAW
ω	SAW frequency
Γ	Total reflection coefficient
Λ	Acoustic wavelength
η_{ACT}	Acoustic charge transfer efficiency

भारतीय प्रौद्योगिकी संस्थान गुवाहाटी • Indian Institute of Technology Guwahati •

TH-3353_166102010

Appendix A

Acoustic Charge Transfer Efficiency

Acoustic charge transfer efficiency (η_{ACT})

The acoustic charge transfer efficiency (η_{ACT}) as mentioned in Chapter 3, can be calculated as

$$\eta_{ACT} = \frac{Q_{out}}{Q_{gen}} \times 100$$

From the experimentally measured current values, the number of charges delivered by SAW at the collector diode has been calculated for each light intensity.

For 4 mW light intensity, J = 2.32 nA/cm^2, number of charges collected the output, Q_{out} = 4.35 × 10^7

For 4 mW, the number of photogenerated charges per second for the slit width of 700 µm = 7.75 × 10^{14}

Number of photogenerated charges for the duration the film is exposed ($t = \frac{\text{slit width}}{\text{wave velocity}} = 200$ ns), Q_{gen} = 1.55 × 10^8

Therefore, acoustic charge transfer efficiency, $\eta_{ACT} = \frac{4.35\times10^7}{1.55\times10^8} \times 100 = 28\%$

Similarly, for 6 mW light intensity, J = 3.6 nA/cm^2, Q_{out} = 6.7 X 10^7, Q_{gen} = 2.4 X 10^8, η_{ACT} = 27.6%

TH-3353_166102010

TH-3353_166102010

Publications from the thesis

Journals:

- **H. Mishra,** P. Bhattacharjee, and H. B. Nemade, "Acoustic charge transport in organic semiconductor films," *J. Phys. D. Appl. Phys*., vol. 55, pp 015102, 2022.
- **H. Mishra,** P. Bhattacharjee, and H. B. Nemade, " Acoustical control of charge carrier movement in an organic semiconductor," *Sensors and Actuators A: Physical*, vol. 358, pp 114451, 2023.
- **H. Mishra,** P. Bhattacharjee, and H. B. Nemade, H. B. "Long-range chain alignment in MEH-PPV films cast under an electric field," *J Mater Sci: Mater Electron* vol. 35, pp 396, 2024.
- **H. Mishra,** P. Bhattacharjee, and H. B. Nemade, "Development and demonstration of charge transfer devices with aligned polymer films," *IEEE Transactions on Electron Devices*, vol. 70, no. 10, pp. 5313-5318, 2023.

TH-3353_166102010